Do mantle xenoliths preserve water signature from the lithospheric mantle and how ? : An analytical, experimental and numerical approach

Konstantinos Thomaidis

Université de Lille - Laboratoire Unité Matériaux Et Transformation - Matériaux Terrestres et Planétaires
École doctorale n°104: Sciences de la Matière, du rayonnement et de l'environnement
Thèse de doctorat - Spécialité: Milieux denses, matériaux et composants

Do mantle xenoliths preserve water signature from the lithospheric mantle and how? An analytical, experimental and numerical approach.

Les xénolites mantelliques préservent-ils la signature en eau du manteau lithosphérique et comment? Une approche analytique, expérimentale et numérique.

Présentée par Konstantinos Thomaidis
Dirigée par Jannick Ingrin et Pierre Hirel

Soutenue le 31 Mars 2022 devant le jury composé de:

Sautter Violaine, DR	Sorbonne Université	Rapporteur
Demouchy Sylvie, DR	Université Clermont Auvergne	Rapporteur
Deloule Etienne, DR	Université de Lorraine	Examinateur
Merkel Sébastien, PR	Université de Lille	Examinateur – Président du jury
Ingrin Jannick, DR	Université de Lille	Directeur de thèse
Hirel Pierre, MC	Université de Lille	Co-encadrant

Octobre 2018 – Mars 2022

Cover art: “Cinq Bleu” 2021
Illustration by Jules L'Hostis.
Conception and refinement by Konstantinos Thomaidis and Jules L'Hostis.

“The water as the most important element in our life is everywhere and “hugs” planet earth in ways we still don’t understand. In this illustration, we attempt to present the water cycle from an artistic, minimalistic point of view.” KT

«ὣς οὐδὲν γλύκιον ἧς πατρίδος οὐδὲ τοκήων γίγνεται...»
[...]
«Οὖτις ἐμοί γ᾽ ὄνομα: Οὖτιν δέ με κικλήσκουσι
μήτηρ ἠδὲ πατὴρ ἠδ᾽ ἄλλοι πάντες ἑταῖροι...»
[...]
«Κύκλωψ, αἴ κέν τίς σε καταθνητῶν ἀνθρώπων
ὀφθαλμοῦ εἴρηται ἀεικελίην ἀλαωτύν, φάσθαι Ὀδυσσῆα..»

(Όμηρος, Οδύσσεια Ι’, 34, 366-367, 502-504)

To my parents

Translation:
«The sweetest in the world I know is homeland and parents...»
[...]
«My name is Nobody, and all of them they call me Nobody,
my mother, my father and my comrades… »
[...]
«If any mortal human ask you Cyclops,
who got your eye out, say that Odysseus blinded you…»

(Homer, Odyssey I’, 34, 366-367, 502-504)

Résumé

L'eau sous forme de défauts ponctuels dans la structure des pyroxènes des xénolites du manteau est fréquemment utilisée pour tracer la teneur en eau du manteau lithosphérique. Cependant, on sait peu de choses sur le mécanisme qui permet aux xénolites de conserver les signatures hydrogène profondes et si l'on peut éviter une réinitialisation complète ou partielle par réaction avec le magma hôte pendant le transport. En particulier, on ne sait pas : 1) comment la teneur en eau des xénolites est modifiée par le mode d'éruption et pendant le refroidissement de la lave en surface 2) comment les joints de grains peuvent affecter l'échange d'hydrogène du xénolite avec le magma. L'objectif de cette thèse est de mieux comprendre ces deux aspects de la préservation de la signature de l'eau dans les xénolites mantelliques.

La première question est abordée à travers une étude des xénolites de péridotites de deux localités du Massif Central, Allègre et Ray Pic. Nous avons effectué environ 1000 analyses ponctuelles par FTIR et mesures de profil dans des cristaux d'olivine, clinopyroxènes et orthopyroxènes (opx) provenant de 16 xénolites collectés sur les deux localités. Les deux localités ont des structures de coulée de lave différentes, Allègre est un lac de lave figé et a une structure verticale tandis que Ray Pic est une coulée de lave typique allongée/horizontale. À Allègre, nous avons étudié des xénolites à différentes hauteurs au sein d'un massif de lave de 30 m. À Ray Pic, nous avons échantillonné des xénolites le long d'une coulée de lave de 20 km et dans un dépôt pyroclastique au niveau de l'édifice volcanique. Les deux études montrent qu'il n'y a aucune preuve que le refroidissement et la solidification des coulées basaltiques affectent la teneur totale en eau des pyroxènes dans les xénolites du manteau. Cependant, la comparaison des xénolites du dépôt pyroclastique avec ceux de la coulée de lave à Ray Pic montre clairement que la concentration en eau est fortement affectée par le degré de dégazage du magma avant l'éruption. Par contre, des xénolites avec des pyroxènes présentant différentes signatures spectrales, coexistent dans la même coulée de lave. La mise en place et le dégazage n'affectent donc pas les signatures spectrales, suggérant que des signatures antérieurement peuvent être conservées.

Pour la deuxième question, nous nous sommes concentrés sur l'étude de l'échange isotopique de l'hydrogène des xénolites avec leur environnement. Nous avons utilisé une approche combinant expérimentation et numérique. Nous présentons les résultats d'expériences d'échange hydrogène/deutérium réalisés dans des morceaux cubiques de taille centimétrique provenant d'un même xénolite. Les expériences ont été réalisées entre 600 et 900°C dans un gaz enrichi en

deutérium (D), à pression ambiante. Nous avons utilisé des monocristaux d'opx du même xénolite, comme témoins de la progression de l'échange avec le gaz. Nous avons comparé les profils de diffusion mesurés dans les monocristaux et les opx situés au bord des cubes avec les profils de diffusion dans les opx à l'intérieur des cubes. Les profils de diffusion ont été analysés grâce à un logiciel de modélisation numérique 2D (Idefick). Nos lois de diffusion H/D pour la diffusion intra-cristalline dans les opx mantelliques sont légèrement plus lentes mais comparables à celles proposées par Stalder et Behrens (2006) pour l'enstatite synthétique pure. Les profils OH-OD enregistrés dans les opx à l'intérieur des cubes ne sont que légèrement plus courts que ceux enregistrés dans les opx au bord des cubes (la diffusion apparente à l'intérieur des cubes est significativement, mais modérément affectée). Ces résultats montrent que la diffusion isotopique de l'hydrogène dans les joints de grains est suffisamment rapide pour équilibrer rapidement les cristaux d'opx à l'intérieur d'échantillons centimétriques. La diffusion aux joints de grains impliquant l'échange H/D dans les xénolites est au moins 2 ordres de grandeur plus rapide que la diffusion intra-cristalline dans l'opx. C'est une première preuve que dans la nature, la signature δD des xénolites est très probablement contrôlée par l'équilibre avec le magma hôte, même dans le cas de xénolites de taille conséquentes. Ceci explique pourquoi les pyroxènes de la plupart des xénolites du manteau ont des signatures δD appauvries. Celles-ci reflètent plutôt un équilibre avec un magma dégazé qu'une signature originale du manteau.

Abstract

Water in the form of hydrous point defects in the crystal structure of pyroxenes from mantle xenoliths is frequently used to trace the water content in the lithospheric mantle. However, little is known on the mechanism that allows xenoliths to preserve deep hydrogen signatures and if we can avoid complete or partial reset by reaction with the host magma during transport. Especially, it is unknown: 1) how much water content of xenoliths is modified by the eruption mode (effusive versus explosive) and during lava emplacement 2) how grain boundaries can affect hydrogen exchange in the xenolith with the surrounding melt. The aim of this thesis is to provide better understanding on these two aspects of the preservation of water signature in mantle xenoliths.

The first question is approached through an analytical study of peridotite xenoliths from two localities in the French Massif Central, Allègre and Ray Pic. We performed around 1000 FTIR point analysis and profile measurements in ol, cpx and opx crystals derived from 16 xenoliths collected on both localities. The two localities have different lava flow structures, Allègre is a frozen lava lake and has a vertical structure while Ray Pic basaltic lava flow is a typical elongated/horizontally one. In Allègre, we studied xenoliths from different heights in the 30 m lava body. In Ray Pic we sampled xenoliths along the 20 km lava flow and in a pyroclastic deposit at the volcanic edifice. Both studies show that there is no evidence that cooling and solidification of basaltic flows affect the total water content of pyroxenes in xenoliths. However, the comparison of the xenoliths from the pyroclastic deposit and the lava flow at Ray Pic shows that the water concentration is strongly affected by the degree of degassing of the magma prior the eruption. In addition, xenoliths with different spectral signatures of pyroxenes coexist within the same lava flow showing that the emplacement and degassing does not affect spectral signatures, suggesting that they may preserve signatures acquired earlier.

For the second question, we concentrated on the study of H isotopic exchange of the xenoliths with its surrounding. We used a combine experimental and numerical approach. In our experimental approach, we present results from hydrogen-deuterium exchange experiments performed in cm-size cubic pieces of a natural xenolith, a spinel lherzolite aggregate. Experiments were performed between 600-900^{o}C in a deuterium (D) enriched gas, at room pressure. We used single crystals of opx from the same xenolith, as sensors of the progress of the exchange with the gas. We compared diffusion profiles measured in single crystals and opx located at the edge of the cubes with diffusion profiles in opx inside the cubes, not directly in contact with the gas. Diffusion

profiles were analysed through a 2D numerical modelling software (Idefick). Our H/D diffusion laws for intra-crystalline diffusion in mantle opx are slightly slower but comparable to the ones in literature for synthetic pure enstatite. OH-OD profiles recorded by FTIR in opx inside the cubes are only moderately shorter than the ones recorded in opx at the edge of the cubes (i.e. apparent diffusion inside the cubes are only moderately slower). These results indicate that the isotopic diffusion of hydrogen in grain boundaries is fast enough to equilibrate rapidly the opx crystals inside the cube xenoliths. It shows that grain boundary diffusion involving H/D exchange in xenoliths is at least 2 orders of magnitude faster than intra-crystalline diffusion in opx. This can be a first-evidence that in nature the δD signature of xenoliths is very likely controlled by the equilibrium with the host magma even in the case of xenoliths with large grain size. It provides explanation why pyroxenes from most mantle xenoliths have depleted δD signatures. These rather reflect equilibrium with a degassed magma than an original mantle signature.

Résumé grand public

Nos connaissances sur la structure du manteau terrestre proviennent principalement des données sismologiques et des xénolites, des roches qui se sont formées dans le manteau et sont transportées à la surface par les volcans lors de l'ascension du magma. Les principaux minéraux qui constituent ces xénolites contiennent de l'eau piégée sous forme d'atomes d'hydrogène dans leur structure cristalline. Les xénolites ont été largement étudiés pour tenter de quantifier l'eau cachée dans le manteau. Dans cette étude, nous avons étudié des xénolites du Massif Central français pour tenter de trouver des réponses à deux questions. 1) De l'eau s'échappe-t-elle des minéraux des xénolites pendant l'éruption puis lors du refroidissement de la lave en surface ? 2) Le rapport isotopique entre hydrogène et deutérium original (un des isotopes de l'hydrogène) est-il conservé par les xénolites lors de leurs transports jusqu'à la surface ? Afin de répondre à la première question, nous avons réalisé une étude analytique sur 16 xénolites. L'étude a révélé que l'eau contenue dans les xénolites n'est pas affectée par le refroidissement de la lave en surface, mais plutôt par la quantité de gaz qui s'est échappée du magma avant et pendant l'éruption. Pour la seconde question, nous avons réalisé des expériences de diffusion, entre 600 et 900°C, dans des cubes centimétriques de xénolites. Les résultats des expériences ont révélé que la diffusion à travers le xénolite est suffisamment rapide pour rééquilibrer rapidement l'ensemble de celui-ci avec le magma. De cette découverte, nous concluons que la mémoire du rapport original hydrogène - deutérium dans les xénolites est très difficile à conserver pendant leurs voyages vers la surface. Ces résultats ont conduit à une réinterprétation des données existantes sur les xénolites.

Popular Science Abstract

Our knowledge for Earth's mantle layer comes mainly through seismological data and xenoliths, rocks that formed at mantle depths and are transported by volcanoes to the surface during magma ascent. The main minerals that constitute these xenoliths have some water trapped as hydrogen atoms in their crystal structure. Xenoliths have been studied extensively in an attempt to find the actual water content hidden in the mantle. In this work, we studied xenoliths from the French Massif Central and tried to find answers to two questions. 1) Does the water content escape from xenolith minerals while the lava erupts and then is cooling at the surface? 2) Can the ratio between hydrogen and deuterium (one isotope of hydrogen) in xenoliths preserves its original values while travelling from the mantle to the surface? In order to answer the first question we performed an analytical study of 16 xenoliths. The study revealed that water in xenolith minerals is not affected by the cooling of the lava but rather by how much gas has escaped from the magma prior and during eruption. For the second question, we performed diffusion experiments, between 600-900^{o}C, in one cm^{3} cubes of xenoliths. Results of experiments revealed that diffusion through the xenolith is fast enough to re-equilibrate rapidly the xenolith with the magma. From this finding, we conclude that memory of the original hydrogen deuterium ratio in xenoliths is very difficult to preserve during the journey to the Earth's surface. These results lead to a reinterpretation of existing data from xenoliths.

Table of contents

Abbreviations

A_{OD}: Deuterium integral absorption
A_{OH}: Hydrogen integral absorption
Cpx: Clinopyroxene
D: Intra-crystalline diffusion coefficient
D_a: Apparent intra-crystalline diffusion coefficient (within the cubes of xenolith)
D_{gb}: Diffusion coefficient in grain boundary
FMC: French Massif Central
FTIR: Fourier-Transform Infrared spectroscopy
IR: Infrared
gb: Grain boundary
H/D experiments: Hydrogen/Deuterium experiments
NAMs: Nominally Anhydrous Minerals
Ol: Olivine
Opx: Orthopyroxene
ppm: parts per million
SCLM: Sub-Continental Lithospheric Mantle

1. Introduction

In the introduction of this PhD thesis, we will describe briefly few basic terms, the state-of-the-art, the novelty and the aim of this work.

1.1 Lithospheric mantle and water

Earth's structure is separated into three main layers (Fig. 1.1), crust (upper layer, 5-70 km thick), mantle (down to 2900 km depth) and core (outer + inner ≈ 3500 km thick). Lithosphere is composed of the crust and an upper part of the upper mantle. This uppermost part of Earth's mantle is called lithospheric mantle. The mantle itself is 82% of the Earth's volume and 65% of its mass and is separated into two distinct units, the upper mantle above 670 km depth and the lower mantle between 670 and 2900 km depth. The lithospheric and asthenospheric part of the upper mantle above the transition zone (above 410 km depth) predominantly consists of peridotite rock composed in majority by olivine, enstatite (opx) and diopside (cpx) minerals with minor amount of spinel or garnet. The chemical composition of the transition zone between 410 and 670 km depths is similar to the rest of the upper mantle but with olivine being replaced by wadsleyite and ringwoodite, two polymorphs of olivine and a progressive decrease of the proportion of pyroxenes (enstatite and diopside) in favour of garnet.

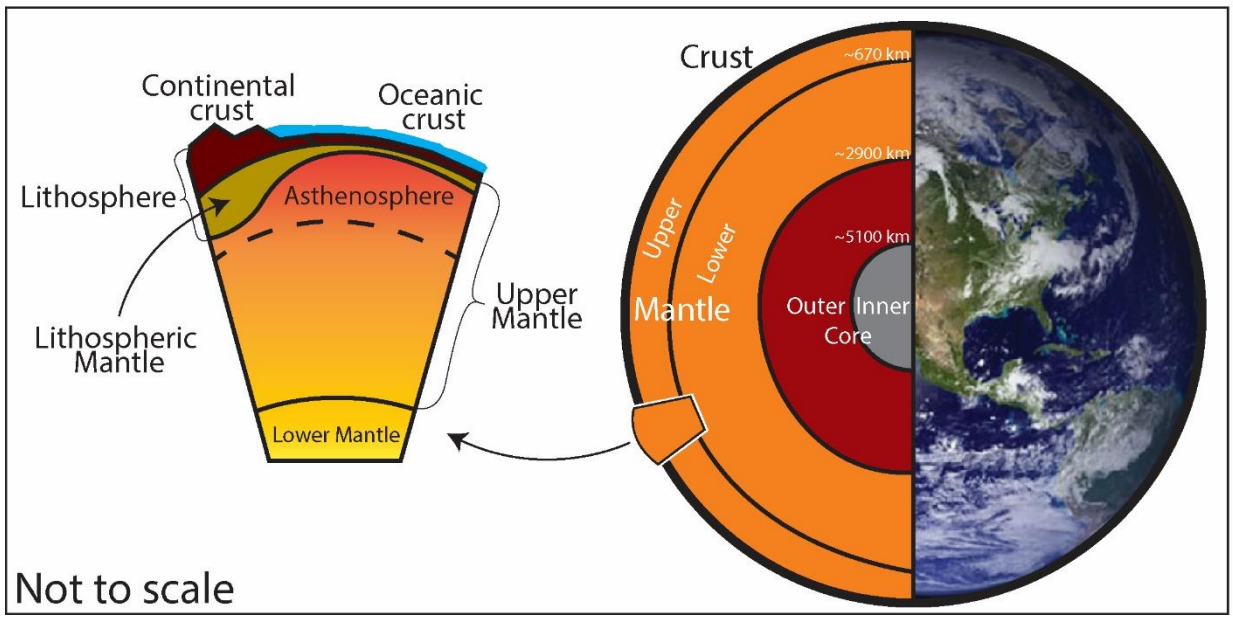

Figure 1.1: Simplified drawing of Earth's interior with its different layers. Modified after Karla Panchuk (2018) CC BY 4.0. Earth photo by NASA (n.d.) public domain.

The best evidence of upper mantle's composition comes from the mantle xenoliths, often called peridotite xenoliths. Xenoliths (Greek: ξενόλιθος, foreign rock) from the mantle are transported in surface through volcanic processes and they provide a direct insight into mineralogical and geochemistry processes in the mantle. They also provide information on the concentration and nature of water in the deep lithosphere (e.g. Ingrin and Skogby 2000; Grant et al. 2007; Demouchy and Bolfan-Casanova 2016; Peslier et al. 2017). As mentioned before the three main minerals that constitute peridotite mantle xenoliths and therefore mantle, are olivine (ol), enstatite with the orthopyroxene structure (opx) and diopside with clinopyroxene structure (cpx). In the ancient time, pyroxenes (ancient Greek: πυρόξενος, fire foreigner) crystals, were considered as impurities in the volcanic glass and not early forming minerals (Bowen's discontinuous reaction series). One of the important information carried from these three minerals is that they include hydrogen in their crystal structure in ppm quantities that may provide insights on the volatile contents in the lithospheric mantle.

Hydrogen is the most abundant element in the universe, as it accounts for almost the 3/4 of all matter and the most vital element of our lives making up around 60% of all the atoms in the human body. Despite this rich profusion above, hydrogen constitutes only 0.14% of the Earth's crust and 0.012% of the primitive mantle (Palme and O'Neil, 2005). However, Earth's mantle is gargantuan and even this small amount is disproportionately important. Several studies suggested that there is 1-7 times the amount of water in Earth's solid mantle as in all of Earth's oceans (Peslier et al. 2017). Majority of this water being under the form of hydrogen incorporation as point defects into nominally anhydrous minerals (NAMs) (Fig. 2.1a). Hydrogen in NAMs is associated with point defects in the crystal structure and can be present in the form of hydroxyl (OH^-) (Bell and Rossman, 1992), water (H_2O), molecular hydrogen (H_2) (Yang et al., 2016) or ammonium molecules (NH_4^+).

1.2 Importance of hydrogen in NAMs

The way hydrogen is distributed in minerals and how it is bonded in their crystal structure are fundamental questions as these control some of their properties such as, pressure and temperature phase stability, rheology and electrical conductivity (Karato, 1990; Gatta et. al., 2021). Even traces of hydrogen can affect the propagation of seismic wave velocities in mantle minerals like NAMs (Karato, 2006). Experiments have been made in olivine and pyroxenes, at high pressures, showing

that these minerals can incorporate significant amount of hydrogen, over 700 ppm, in the condition of the upper mantle (Van der Meijde et al. 2003: Frost and Dolejs, 2007 and references therein). Some studies have found that the high-pressure olivine polymorphs (wadsleyite, ringwoodite) can even store larger quantities of water, something that gave ground to the hypothesis that the transition zones may host a large amount of water (Litasov and Ohtani, 2007). Therefore, olivines and pyroxenes (NAMs) from the upper mantle are key witnesses and may play a key role in the transport of hydrogen between the two hydrogen rich reservoirs, the crust and the transition zone, participating to the water cycle between deep Earth and surface.

From the mantle minerals, pyroxenes are the most hydrous, containing from few tens up to 500 ppm %wt. H_2O, dominating the water budget in the mantle (Bell and Rossman, 1992). More specifically, hydrogen concentration in NAMs from mantle peridotite xenoliths range from 0-200 ppm %wt. H_2O for olivine, 0-650 ppm %wt. H_2O for opx and 0-1000 ppm %wt. H_2O for cpx (Ingrin and Skogby, 2000; Peslier, 2010; Demouchy and Bolfan-Casanova, 2016).

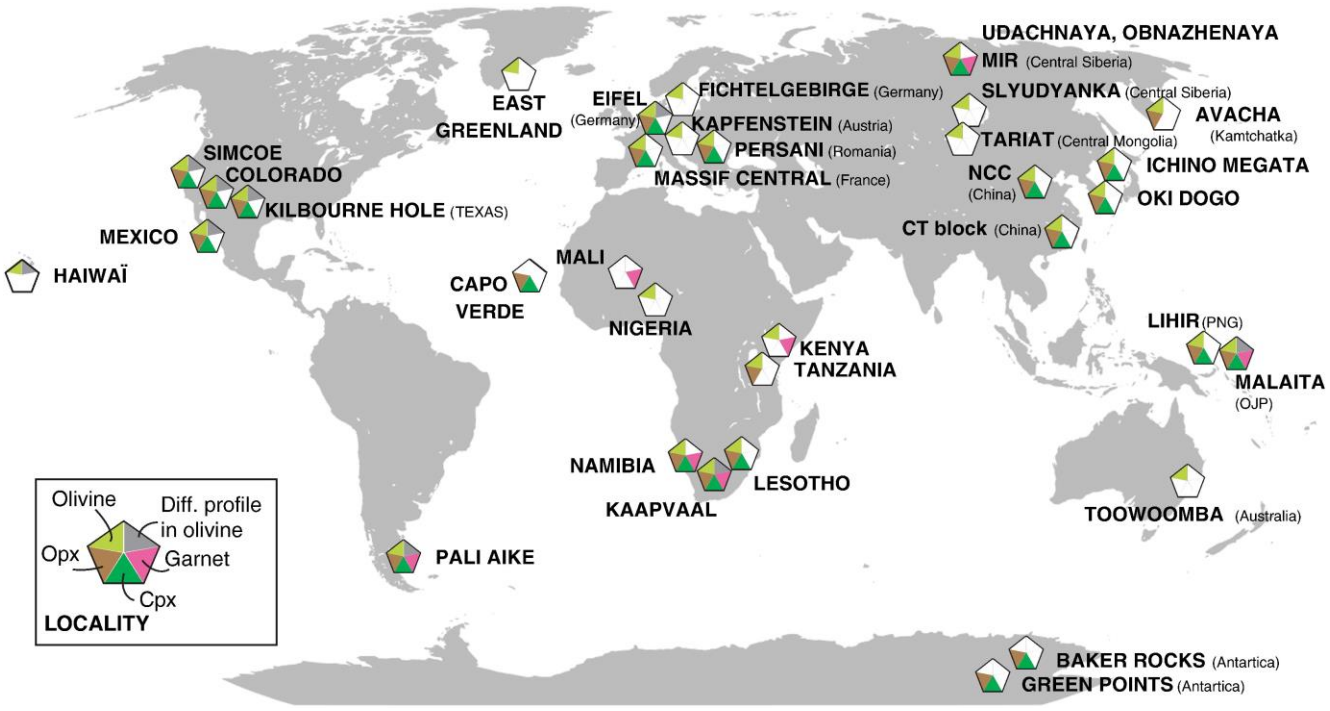

Fig. 1.2: Geological localities from studies which are reporting water concentrations from mantle derived NAMs. Figure taken from Demouchy and Bolfan-Casanova, 2016.

1.3 Water concentration and preservation in xenoliths from the lithospheric mantle

When it concerns natural samples (i.e. mantle xenoliths) and quantification of the water from the lithospheric mantle several questions arise. Water can be lost and/or added during the whole process of magma sampling of xenoliths, ascent and eruption. Mantle xenoliths usually are derived from the lithospheric mantle beneath continents, but not only. Because of the complex processes that occur prior and during transport to the surface, it is still debated if they can be representative of upper mantle conditions. There are studies suggesting that the most reliable minerals for preserving information about the true water content from the mantle are the pyroxenes (Denis et al. 2013; Tian et al. 2017).

Studies of water in magmas at different geological settings have been made, trying to decipher the hydrogen content from the mantle (Zimmer et al. 2010; Plank et al. 2013). Almost all the arc volcanoes with mafic magmas contain 2–6 %wt. water (Plank et al. 2013) and clinopyroxene crystals have been studied as potential recorders of magmatic water but the results revealed that cpx from slowly cooled basaltic lavas are not always credible for reconstruction of original magmatic water contents (Lloyd et al., 2016). Similarly, Towbin and Plank (2021) pointed out that a 0.5 mm diameter cpx single crystal needs ~1.5 days to complete overprint water signature with magmatic concentrations, while ascent time of some xenoliths was calculated to be as long as 13 -27 days. However, most of these interpretations are based solely on single crystals diffusion data and nobody really know if fully apply to xenoliths.

So far there is no direct correlation between hydrogen content and other physical or chemical properties of mantle xenoliths but there are evidences showing that water signature (content and spectral characteristics) of pyroxenes in xenoliths preserve an equilibrium memory from mantle depths (Grant et al. 2007; Warren & Hauri 2014; Patko et al., 2019). Likewise, it is suggested that some of these equilibria could have been achieved during magma transport of xenoliths in the surface (Ferriss et al. 2016; Tian et al. 2017), calling into doubt the fidelity of pyroxenes in xenoliths as indicators of the water signature in the mantle. In addition, little is known on the mechanism that allows xenoliths to preserve these deep-water signatures and avoid complete exchange with the host magma during transport. It is unclear how to explain the preservation of the water signature considering the fast diffusion observed in single crystals from previous experiments (in olivine Mackwell and Kohlstedt, 1990; Kohlstedt and Mackwell, 1998; Demouchy and Mackwell, 2006; in forsterite Demouchy and Mackwell, 2003; Padrón-Navarta et

al., 2014; in enstatite Stalder and Skogby, 2003; in diopside Carpenter Wood, 2001; Ingrin et al., 1995; Hercule and Ingrin, 1999; reviews Ingrin and Blanchard 2006; Farver 2010) and how these data can be applied to multiphases polycrystalline aggregates such as peridotite xenoliths. One possible explanation and key element for our understanding may be the control of diffusion by grain boundary diffusion in the polycrystalline xenoliths.

1.4 Water enrichment and diffusion in the grain boundary

In order to evaluate the influence of grain boundary on the water mobility there are two important parameters that need to be addressed, the relative enrichment of water in the grain boundary versus the crystal lattice (speciation), and the specific mobility of hydrogen in the grain boundary (D_{gb}, diffusion in gb).

There are studies indicating that grain boundaries may store water up to several times of magnitude higher than in grain interiors (Hiraga et. al. 2007; Sommer et. al. 2008; Fei et. al. 2016). In recent experiments, attempts made to trace the distribution of heavy water (D_2O) in synthetic peridotite within olivine-olivine boundaries (Gardner et.al. 2020) suggested that boundaries were enriched in ^2H by 2-3 orders of magnitude compared to grain interiors. Another partition coefficient of water between grain boundary and lattice in synthetic forsterite (Mg_2SiO_4), was proposed by Fei et. al. 2016. They proposed a value of C^{gb}/C^{lat} ≈520, derived from the average value of a total 25 measurements with min = 70 and max = 1780.

However, it is still unclear how grain boundaries can affect hydrogen exchange between the different constitutive minerals and with the surrounding melt. One attempt to estimate this impact was performed by Demouchy (2010) in sintered polycrystalline San Carlos olivine with small grain size (≤ 10 μm). In this study, grain boundary diffusion of hydrogen was three orders of magnitude faster than intra-crystalline diffusion in olivine. However, when extrapolated to grains size relevant to mantle conditions and mantle xenoliths, under the same assumptions of H concentration in grain boundary than in the experiments, the impact of grain boundary diffusion became negligible compared to intracrystalline diffusion (Demouchy 2010). Effective hydrogen diffusion in a peridotite xenolith made of olivine, orthopyroxene and clinopyroxene with different concentrations of hydrogen point defects, grain sizes and multiple grain boundaries can be quite different to the one observed in an experimentally sintered single-phase olivine aggregate.

Therefore, it is currently difficult to evaluate what mechanism control the exchange of hydrogen within real mantle xenoliths even for the simple case of hydrogen isotopic exchange.

1.5 Novelty and aim of this work

During this thesis we addressed two main questions:

1. What is the effect of the type of eruption on the preservation of water in xenoliths? More specifically, how the emplacement of basalt, the cooling and the solidification affect the water content of the embedded xenoliths. In order to answer it, we identified two specific cases, Allègre and Ray-Pic, where we can explore the volcanology effect in the water preservation in the mantle xenoliths. These two localities provide us with two different lava structures, a vertical lava lake and an elongated horizontal lava flow.
2. Do pyroxenes in xenoliths preserve their original mantle isotopic signature, and especially, what is the role of the grain boundaries in the control on hydrogen diffusion and exchange between the xenolith and the magma? In order, to reply to this question we performed H/D exchange experiments in deuterium (D) enriched gas at various temperatures (600-900^{o}C) in xenolithic cubes of 1 cm^3. We compare isotopic diffusion rates from opx single crystals and in the edge of the cubes, with profiles measured inside the cubes. To better understand and evaluate our data we use 'Idefick', a numerical modelling software specifically created for this work.

It is the first time that real upper mantle whole-rock, under the form of cubes of 1 cm^3 is used to investigate the effect of the grain boundary diffusion of hydrogen in mantle rocks. Many studies have been made before in single grains of ol, cpx and opx but never in whole rock xenolith. The use of the nature whole-rock samples was a challenging aspect of this work, because in some ways we have to perform blind experiments until we cut the cubes for analysis and it is not always easy to find suitable crystals within the sample for profile measurements.

After this introduction, we present briefly in chapter 2 some basic concepts in crystalline defects and diffusion. Chapter 3 is following with information for the sample localities and the samples, while in chapter 4 we present the experimental and analytical methods of this work. In chapter 5 we are addressing the first question and in chapter 6 the second. In the chapter 7 we present our conclusions and expose shortly some possible perspectives.

2. Diffusion and defects

Diffusion in a crystalline solid, such as a mineral, requires net movement of atoms from one crystallographic site to a neighboring one. Defects in the crystal structure (e.g. point defects, grain boundaries) are an essential prerequisite to enable mobility of the diffusion species. In this chapter, we will present the notion of crystalline defects and the basic concept of diffusion.

2.1 Crystalline defects (point defects and grain boundaries)

A crystalline material, such as a mineral, consists of an almost perfect periodic array of atoms. Crystalline defects are the interruptions of these perfect periodic arrangements of atoms. There are four types of defects based on their geometry: a) point defects, b) line defects, c) planar defects, and d) bulk (3D) defects.

Point defects are called the defects at a scale of individual atoms, usually where an atom is missing or is in an irregular place in the crystal structure. Point defects include: a) vacancies; vacant atomic sites, b) interstitial atoms; atoms in sites that normally are empty, c) aliovalent ions; ions with different charges from normal (e.g. Fe^{3+} at Fe^{2+} site) and d) impurity atoms (Fig. 2.1a). As an example, in FeO crystals, if only divalent iron (Fe^{2+}) was present then the crystals would be perfect, but FeO is rarely stoichiometric, its composition is Fe_xO with $x < 1$. In this case, it is because some Fe^{3+} ions are present in the structure, then for every two Fe^{3+} ions we must have an empty iron site (defect structure) in order to preserve the electrical neutrality. The concentration of point defects in the crystal structure is controlled by the thermochemical equilibrium, meaning that there is a relation between the concentration of point defects and temperature, pressure and chemical environment. Under otherwise chemical equilibrium, the concentration of point defects increases exponentially with temperature and can change notably with pressure.

There are two special point defects that does not affect the stoichiometry of the crystal: a) Schottky defects and b) Frenkel pairs (Fig. 2.1b). Schottky defects refers to the formation of vacancies in proportion of the stoichiometry of the crystal ($V_{Na} + V_{Cl}$ in the case of halite for instance, Fig. 2.1b). Frenkel pairs refers to the removing of an atom from its site putting it as an interstitial (Fig. 2.1b).

A crystalline solid is commonly found in the form of an aggregate of more or less randomly oriented single crystals (grains). Grain boundaries are considered as two-dimensional imperfections (planar defects) and are the interfacial transition regions between two same phase

crystals with different crystallographic orientation. Grain boundaries usually are distinct from the interphase boundaries between different phase crystals, but in this work for simplicity, we will refer to grain boundaries for both cases. Although, grain boundaries have only few atomic layers thickness, approximately ~1 nm (Kaur et. al. 1995; Dohmen and Milke 2010), their effective thickness usually is larger than the structure thickness, especially in ionic solids. The best direct method to determine the width of grain boundaries is by TEM (Transmission Electron Microscopy). Grain boundaries are classified into low-angle (<15^o) and high-angle (>15^o) boundaries. Low-angle are further separated into tilt boundaries (array of edge dislocations) and twist boundaries (screw dislocations) (Karato, 2008). However, this type of classification is valid only for grain boundaries between identical phases; it is less useful for ol-px, opx-cpx and silicate-spinel interfaces present in xenoliths.

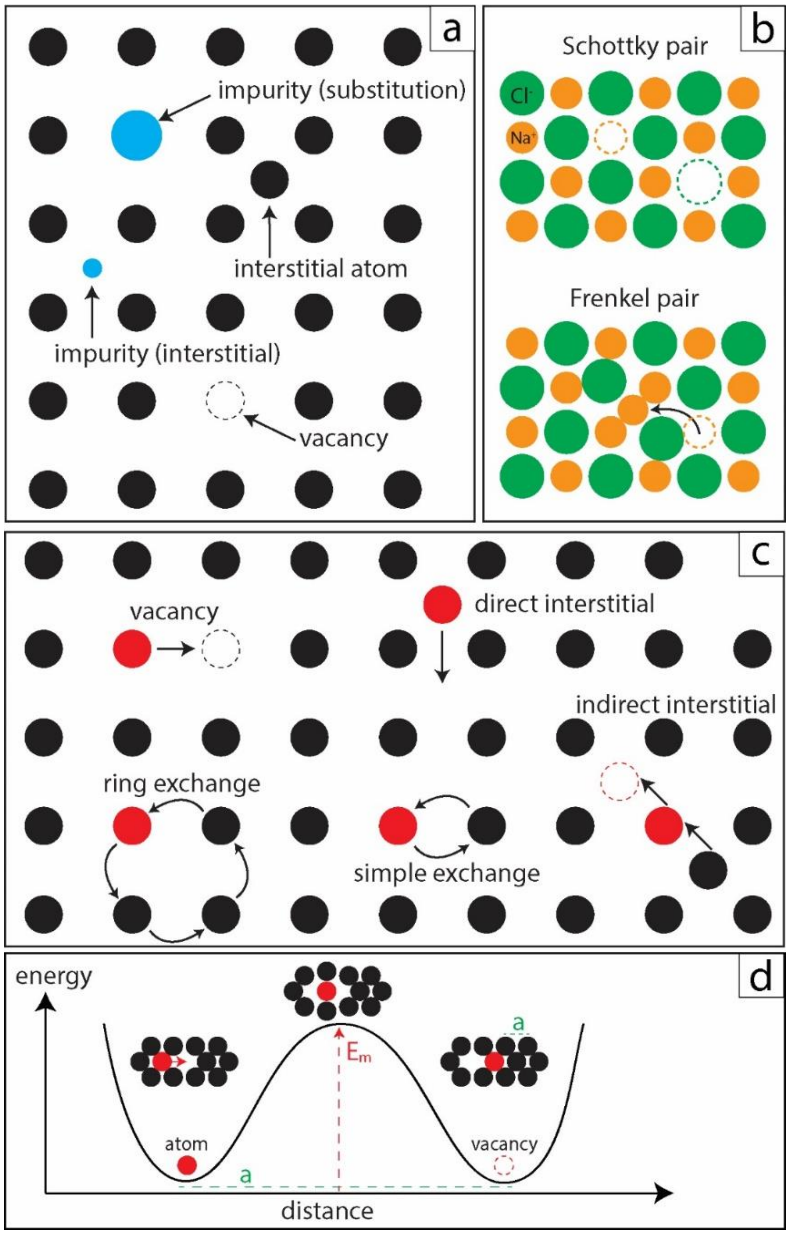

Fig. 2.1: a) Point defects in a crystal lattice. Modified after Karato (2008). **b)** Stoichiometric point defects. **c)** Basic diffusion mechanisms. **d)** Schematic illustration of the energy barrier that an atom, from its original position, needs to overcome to move into a vacancy.

The importance of grain boundaries in our work is because they can host large amount of impurities and are considered as high diffusivity paths. The segregation of impurities in the grain boundaries is frequent (Hiraga et al. 2004) and plays a great role in the distribution of trace elements, such as hydrogen. They are likely to be present preferentially in the grain boundaries.

2.2 Diffusion mechanisms

Diffusion rate depends of the dominant microscopic mechanism involved and the concentration of the point defects associated. The diffusion mechanisms can be divided into two types a) substitutional mechanism and b) interstitial mechanism (Putnis and McConnell, 1980; Pelleg, 2016).

Substitutional diffusion mechanism is when atoms move from an atomic site to another. In a perfect crystal structure, this action would involve the exchange between atoms. Such a simple exchange (Fig. 2.1c) should require a huge amount of energy as the atoms would need to deform instantaneously a perfect crystal lattice and push the neighbor atoms in order to move. Another substitution mechanism is the ring exchange (Fig. 2.1c), which involves several atoms changing places simultaneously and therefore require even greater amount of energy. These two substitutional exchange mechanisms, in practice, are too improbable. Substitutional diffusion is mostly occurring under vacancy presence (Fig. 2.1c). Vacancy is an empty atomic site in the crystal lattice, where a neighbor atom can move, creating a new vacancy. For simplicity, we can consider this as diffusion of vacancies. Therefore, the diffusion is dependent of the density of vacancies and this make this mechanism in principle slower than the interstitial (see below). The rate of diffusion is determined by the facility of forming vacancies and by the ability of the atoms to perform the jump to the vacancy. As the atoms are vibrating around their position and at higher temperatures even more, they gain enough energy to overcome the energy barrier and they can pass into the neighbor vacancies.

Interstitial diffusion mechanism is when the diffusing atom is moving through an interstitial position to another interstitial position. This direct interstitial mechanism differs from the indirect interstitial (interstitialcy) where an interstitial atom pushes an atom residing in a normal lattice site into an interstitial position (Fig. 2.1c). The latter requires more energy and is less probable. The rate of this type of diffusion is controlled by the facility of the atomic interstice jumps plus the energy to form an interstitial.

The most dominant of all the above diffusion mechanisms is the vacancy mechanism and we will describe it in more details. In thermal equilibrium, a definite concentration of vacant sites exists in materials. Any atoms adjacent to a vacancy has an equal chance to diffuse by jumping into the vacancy. For the frequency of a vacancy exchange, there are two conditions required a) enough jumping energy and b) enough time that the vacancy resides in the vicinity of the energetic atom (Pelleg, 2016). For diffusion to occur it is not enough to create a vacancy but the vacancy must migrate from a one position to another. This vacancy migration occurs by successive jumps from one lattice site to a neighboring site. These jumps require enough energy to break the bonds of the adjacent atoms and to induce lattice distortion, allowing the free pass of the atom between its neighbors. The bond breaking energy required derives from the thermal energy of atomic vibrations and we schematically illustrate the energy barrier required for a vacancy exchange (Fig. 2.1d). E_m is the energy (usually thermal through high temperature) required to supply to the atom for the jump to happen and is known as the activation energy of migration.

The above mechanisms are referred to the bulk diffusion that is different to the grain boundary diffusion. Of course, the same basic concept of diffusion is valid in this case as well. Grain boundary diffusion is the process of atomic transport due to random jumping motion of atoms along the grain boundary. Because of the grain boundary structural ‘disordering’ or ‘lower density’ compared to the bulk crystals, the activation energy for the diffusion is generally smaller and the atomic flux is generally orders of magnitude faster, than the one in the bulk crystal. The significance of grain boundary diffusion derives from the fact it is affecting many rearrangement processes such as diffusion creep mechanisms, sintering, grain growth, recrystallization etc.

2.3 Diffusion and Fick’s laws

More than 2000 years ago, Democritus stated that *“Αρχάς είναι των όλων ατόμους και κενόν…”*, the atoms and the void are the beginning of everything, and atoms are always moving from the beginning of time. This perpetual movement of the atoms is the basic characteristic of the diffusion. The word diffusion derives from “diffundere”, the latin word for “to spread out”. Diffusion (or atomic diffusion) is the net movement of atoms (or molecules, ions etc.) from a high concentration region to a low concertation region. The driving force of diffusion can be a chemical/concentration gradient or a temperature gradient, with the first one being the most

frequent in minerals. Except concentration difference and temperature, diffusion depends also of other parameters such as orientation and surface area.

Back in the 1855, A. E. Fick observed a similarity between diffusion and heat transfer by conduction, and start working in applying the theory of the latter to the former one. He proposed that in an isotropic material the diffusing flux (J) is linearly proportional to the concentration gradient in the direction of the diffusion x_i. This is the "Fick's first law" and is expressed mathematically by:

$$J_{X_i} = -D\frac{\partial c}{\partial x_i} \quad (2.1)$$

where c is the concentration and D the diffusion coefficient, a proportionality constant describing how fast one element can diffuse through a material in the given direction. The negative signs denotes that the flux is occurring in the direction of decreasing concentration. The "Fick's second law of diffusion" is the combination of the first law with the equation of mass conservation and is expressed mathematically by:

$$\frac{\partial c}{\partial t} = \sum_{ij} \frac{\partial}{\partial x_i} D_{ij} \frac{\partial c}{\partial x_j} \quad (2.2)$$

The diffusion coefficient is expressed as D_{ij} because it is actually a second rank tensor. If the diffusion coefficient is isotropic and independent of the concentration, equation (2.2) can be simply written as:

$$\frac{\partial c}{\partial t} = D\sum_i \frac{\partial^2 c}{\partial x_i^2} \quad (2.3)$$

The temperature dependence of the diffusion coefficient follows an Arrhenius relationship:

$$D = D_0 exp\left(-\frac{Ea}{RT}\right) \quad (2.4)$$

where D is diffusion coefficient (m^2/s), D_o is the temperature independent constant, E_a the activation energy of the diffusion (J/mol), R the universal gas constant (8.31446 J/(mol*K)) and T the absolute temperature (K).

Diffusion can occur either through the bulk of the crystal (bulk/volume diffusion) or through defect regions, such as the grain boundary, that have different diffusion coefficient (Fig. 2.2). Because diffusion from these regions are commonly faster from the bulk diffusion, they are

referred in literature as high diffusivity paths. When it comes to the grain boundary as high diffusivity path, you can use the following relationship:

$$D^{eff} = D^{v} + \frac{\pi\delta}{L} D^{B} \quad (2.5)$$

where δ is the thickness of the grain boundary and L is the grain size. This equation is assuming that near grain boundary the area of high diffusion coefficient is limited to δ. Because of the lower activation energy for diffusion in grain boundary than the bulk diffusion, these areas are more important at relatively low temperatures (Karato, 2008).

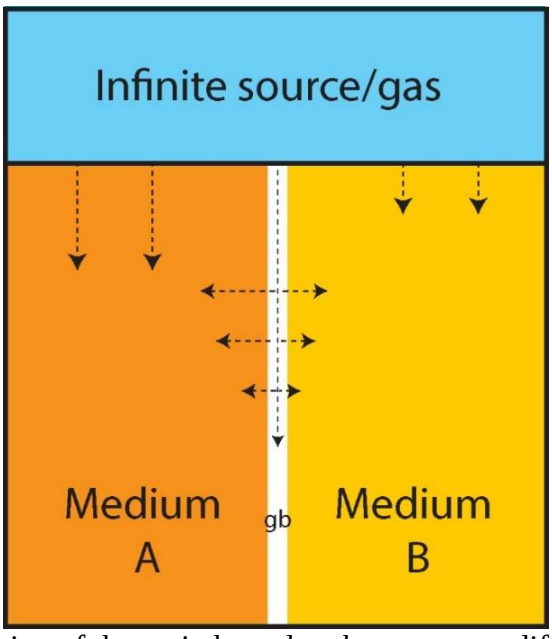

Fig. 2.2: Schematic illustration of the grain boundary between two different mediums.

2.4 Solutions of Fick's law and experiments

In our diffusion experiments, we will be doing two types of measurements a) diffusion in a single direction across a single crystal considered as a semi-infinite slice and, b) diffusion profiles from an edge of a crystal. For the first we are measuring the hydrogen (or/and deuterium) concentration after each heating step and we use the following solution of the Fick's second law:

$$\frac{C(t)-C_0}{C_1-C_0} = 1 - \frac{8}{\pi^2} \sum_{n=0}^{\infty} \frac{1}{(2n+1)^2} \, exp\left(\frac{-D(2n+1)^2\pi^2 t}{4L^2}\right) \quad (2.6)$$

We imported this equation in our code (see below) for calculating the diffusion coefficient for our single crystals. For the diffusion profiles we used:

$$\frac{C(x,t)-C_0}{C_1-C_0} = 1 - \frac{4}{\pi}\sum_{n=0}^{\infty}\frac{(-1)^n}{(2n+1)}\ exp\left(\frac{-D(2n+1)^2\pi^2 t}{4L^2}\right) cos\left(\frac{(2n+1)\pi\chi}{2L}\right) \quad (2.7)$$

For more details in the solutions of Fick's law used in experiments to measure hydrogen diffusion in minerals, see the review paper of Ingrin and Blanchard (2006).

2.5 OH defects in NAMs

To describe the nature of OH defects in olivine, we need to separate the infrared domain of stretching frequencies into three regions:

a) between 3670 - 3400 cm^{-1}, OH bands in this range are generally linked to the replacement of Si atoms in tetrahedral site by H atoms of various numbers, associated or not with other substitutions. They are mostly composed of $(4H^+)^x_{Si}$ defect (Blanchard et al. 2017) and the $([(2H^+)^{''}_{Si}(Ti^{4+})^{\cdot\cdot}_{M1}]^x$ defect (Walker et al. 2007).

b) between 3400 - 3300 cm^{-1}, OH bands are associated with defects linked to trivalent substitutions in octahedral sites compensated by a single H in a nearby octahedral site.

c) below 3300 cm^{-1}, bands are, linked to $(2H)_{M1}$ defects (Blanchard et al. 2017).

In the case of cpx (diopside), many infrared absorption bands related to the OH-stretching modes have been observed. A detailed study by Balan et. al. (2020) has provided a large picture of the possible defect geometry for the absorption bands. Peaks observed and proposed assignments to defects are:

a) at 3651-3620 cm^{-1} are associated to M^{3+} ions substituted for Si in tetrahedral sites

b) at 3460–3432 cm^{-1} are linked with octahedral M^{3+} ions and single protonated Ca vacancies

c) at 3420 cm^{-1} is associated with the Na^+ for Ca^{2+} substitution with an H+ compensating the charge deficiency

d) at 3350 cm^{-1} is linked with double protonated Ca vacancies

e) at 3300 cm^{-1} is likely associated with singly protonated Ca vacancies

Opx (enstatite) has been also studied in order to identify the OH-defects in its crystal structure. A theoretical study of pure enstatite by Balan et. al. (2012) links absorption bands at 3360 and 3070 cm^{-1} with M^{2+} vacancies while the 3690 and 3590 cm^{-1} bands would be associated with Si vacancies partially compensated by interstitial Mg^{2+}. Studies in synthetic enstatite doped with impurity cations such as Al^{3+}

and Cr^{3+} revealed the creation of two additional groups of OH absorption bands, between 3500-3730 cm^{-1} and 2800-3500 cm^{-1} (Prechtel and Stalder, 2012; Stalder et. al., 2015), while absorption bands between 3460-3330 cm^{-1} are linked to OH defects in synthetic enstatite doped with Fe^{3+} (Stalder, 2004).

3. Geological background and sampling locations

3.1 Geological background

All samples in this work are from the French Massif Central (FMC) (Fig. 3.1a), which is part of the Variscan Belt (Matte, 1986). The FMC belongs to the northern Gondwanian margin and is considered one of the best area to study the Variscan metamorphic and plutonic rocks. The FMC is a mass of nappes (large rock bodies that have been transported for long distances due to faulting or folding), an effect of six main tectonic-metamorphic events (see review paper Faure et al., 2009). In the basement of the FMC, we can find all the rock types: igneous rocks, products of the Tertiary-Quaternary volcanism; metamorphic rocks, formed during the Variscan (or Hercynian) orogeny; and sedimentary rocks, created from the deposition of the above.

The spatial-temporal distribution of the Cenozoic volcanism in the FMC has been separated into three main magmatic phases, with the last (third) event taking place from the upper Miocene (~15 Ma) (see Michon and Merle, 2001, for a comprehensive presentation). The third event, which started from the south of FMC, is described as the major magmatic event and it has been the source of the transportation of many mantle xenoliths to the surface.

The xenoliths studied in this work are hosted by Cenozoic alkali basalts and are products of lithospheric thinning (older Variscan units) due to a possible mantle plume. Based on textural variations and geochemical data from the xenoliths, the FMC is separated into two different lithospheric domains, north and south of the 45º30'N boundary (Lenoir et al. 2000). The south mantle xenoliths are significantly less depleted compared with the north xenoliths and have a coarse-granular textures while the north xenoliths show more often protogranular textures (Lenoir et al. 2000; Downes and Dupuy, 1987).

Several geophysical studies connect the volcanic activity with an asthenospheric upwelling beneath the south region of FMC (Lucazeau et al. 1984; Granet et al. 1995; Sobolev et al. 1997; Chevrot et al. 2014). The subcontinental lithospheric mantle (SCLM) underneath FMC has been a subject of various investigations of its evolution and the metasomatism processes that created its compositional variations (Lenoir et al. 2000; Wittig et al. 2007; Harvey et al. 2010; Bräuer et al. 2017; Uenver-Thiele et al. 2017). The differences between the north and the south xenoliths have supported the hypothesis that different agents have metasomatized the two FMC regions,

schematically more carbonatite melt in the north and a more silicate melt in the south (Wittig et al. 2007).

The samples studied in the thesis are all from the southern region. More specifically Allègre samples came from the Deves volcanic district, with the major magmatic events taking place between 3.5-0.5 Ma (Michon and Merle, 2001, Fig.3.1b) and Ray Pic samples from the Velay Oriental, with major magmatic events occurred between 9 Ma – 6 Ma (Michon and Merle, 2001, Fig.3.1b,c). Latest studies dated lavas from Ray Pic volcano 31 ka ago (Sasco et al., 2017).

The xenoliths from Allègre and a nearby volcano (Mt. Coupet) have been studied by Gu et al. (2016, 2018). The authors have found that the xenoliths have experienced multi-stage metasomatism and possible interaction with the host magma. They also concluded that partial melting was the main control mechanism over water content variations in their samples.

The geochemical and mineralogical composition of xenoliths from Ray Pic have been investigated in several previous studies (e.g. Downes and Dupuy 1987; Zangana et al. 1997, 1999; Lenoir et al. 2000). The most recent extensive study is by Denis et al. (2015) where they examined ten xenoliths from the Ray Pic locality. Results reveal no strong correlation between modal metasomatism and enrichment in incompatible element in Cpx. In addition, the observed trace element fractionations attributed to carbonatitic metasomatism and NAMs water content was not affected by hydrous metasomatism.

3.2 Sampling locations

Xenoliths from Allègre used in this work originated from a single location. The samples were collected in the Ringue quarry in Allègre in 2016 (Fig. 3.1d). The quarry is cutting a thick basaltic body from the Allégre volcano over a depth of 30 meters and samples were taken from the three different excavation levels. Basaltic lava from this strombolian volcano was rich in large peridotite xenoliths (Fig. 3.1e).

The second group of samples was collected in a lava flow of the Ray Pic volcano at various distances from the summit and from maar deposits nearby the volcanic edifice (pyroclastic flow), in October 2020 (Fig.3.1c). The lava flow is following “La Bourges” river (Fig.3.1f,g). During the 2016 expedition, samples from Ray Pic were also collected and some were used in this work.

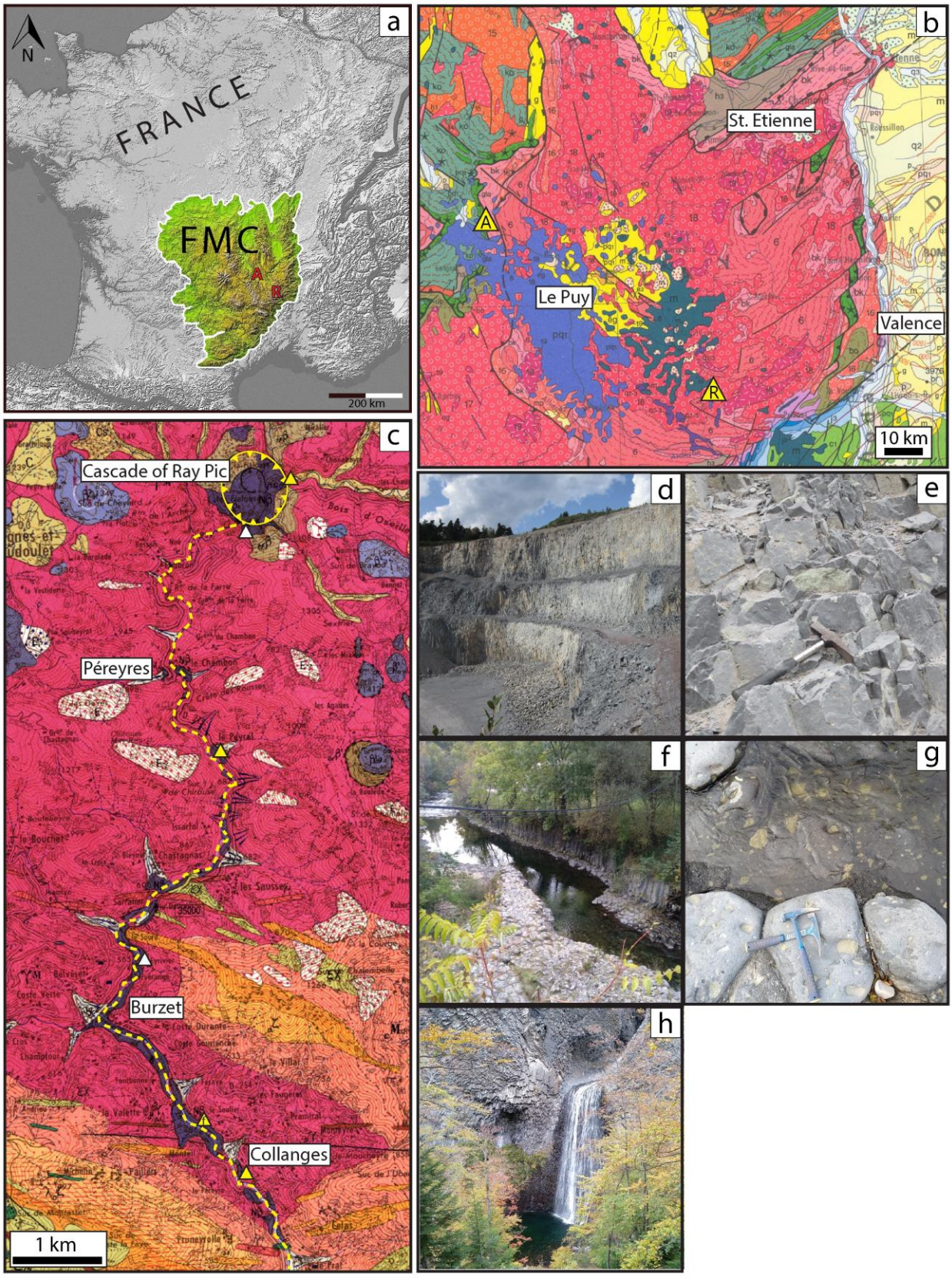
a
N
FRANCE
FMC
A
R
200 km
b
St. Etienne
A
Le Puy
Valence
R
10 km
c
Cascade of Ray Pic
Péreyres
Burzet
Collanges
1 km
d
e
f
g
h

Figure 3.1: a) Map of France showing in colour the location of the French Massif Central (FMC). The red letters mark the location of the two sampling localities, A for Allègre and R for Ray Pic. Map modified from Wikimedia commons (Technob105). **b)** Geological map of the southeast part of the FMC. The light blue area where Allègre is located (yellow triangle) is showing the Devès volcanic region, while the dark green-blue area where Ray Pic is located (yellow triangle) is marking the Velay Oriental volcanic region. **c)** Detailed geological map of the sampling area at Ray Pic. With yellow circle, we underlined the maar crater of Ray Pic. The yellow dashed line is showing the direction of the river and the lava flow. This was also the route we follow to acquire samples in the lava flow. The sample locations are marked with yellow triangles for the 2020 fieldwork and white for the 2016 fieldwork. Dark purple represents the basaltic flow and the dominant red colour the Velay granite. **d)** Panoramic view of the quarry in Allègre, where samples taken from each excavation level (fieldwork 2016). **e)** The basaltic lava in this locality is notably rich in large peridotite xenoliths (up to 20cm long) like the one present in the photo. **f)** Characteristic view of the river that cut the Ray Pic lava flow at Monteil bridge (yellow triangle with f in 2.1c). Columnar jointing created during cooling of the lava flow is present along the whole river. **g)** Inside or outside the water the basalt is very rich in peridotite xenoliths (Monteil bridge). **h)** The Ray Pic cascade (waterfall) indenting the lava flow at the edge of the edifice.

4. Experimental and analytical methods

4.1 Sample preparation

The sample preparation can be separated into three main parts: thin sections, cubes and single crystals.

The Allègre and Ray Pic xenoliths that were selected (e.g. Fig. 4.1a,b,d,h) for thin sections production were sent either to the preparation workshop of the Geology department, University of Lille or to a private Thin Section Laboratory in Toul. The selected xenoliths had average dimension ~250 cm^3 (min 20 cm^3, max 1500 cm^3) and had fresh surfaces, after breaking, with no evidence of weathering. Smaller xenoliths attached with the host basalt were also picked. Thin sections prepared for infrared measurements have thickness between 220-320 μm and were polished both sides (Fig. 4.1c). More than 40 thin sections were prepared from around 20 different xenoliths and we finally analysed 27 thin sections from 16 xenoliths. Some thin sections or samples were disregarded for various reasons:

a) due to their thin but wide shape (~9 cm^2), the thin sections were extremely fragile and destroyed during the epoxy removal (acetone bath) or transportation. The small pieces left were difficult to analyze,

b) technical problems during manufacture lead to either broken pieces or unpolished sides,

c) after cutting, few of them revealed weathered texture or oxidation reactions in the part that was hidden inside the basalt and the sample was immediately excluded from analyses.

The xenolith Alle16_lvl2_07 was selected for the production of the cubes and the single crystals used for the diffusion experiments. The sample was first cut into slices of approximately 1 cm thick and the two central slices were further cut into 9 columns with base area ~1cm^2 (Fig. 4.1e). The central columns (3 to 7) were cut with a low-speed diamond saw into cubes (~1cm^3) (Fig. 4.1f), avoiding those closer to contact with the basalt (columns 1,2,8,9). Cubes where polished with silica carbide grinding paper (#4000 grit size) on all sides and the cubes dimensions were measured with digital micrometer before the experiments. After the experiments, the cubes were cut in the middle with the low-speed diamond saw to produce thin slices, with thickness 300-350 μm (Fig. 4.1g). These thin slices from the cubes were polished both side (final stage 1 μm) and placed in acetone bath for more than 24 hours.

Finally, some columns were crushed for handpicking opx crystals under binocular microscope. Single opx crystals with final thickness between 150 to 370 μm were polished both sides (final stage 1 μm). After polishing, any remaining resin was removed in successive acetone baths for more than 24 hours.

The final thickness of all the prepared samples were measured up to few μm accuracy with a digital micrometer and these values were used to normalize the spectrum data.

Figure 4.1(next page): a) Representative sample from Ray Pic (Burz16 01). **b)** Representative sample from Allègre. **c)** Representative thin slice from Allègre (size 2.5 x 3.5 cm). **d)** Representative thin slice from Ray Pic with the host basalt. **e)** A cut slice of the Alle16_lvl2_07 xenolith with the columns. **f)** Examples of cubes cut in a central column. **g)** The preparation steps for the cube slice. **h)** A table full of samples collected from a single locality in Ray Pic revealing the amount of rocks gathered during the 2020 expedition.

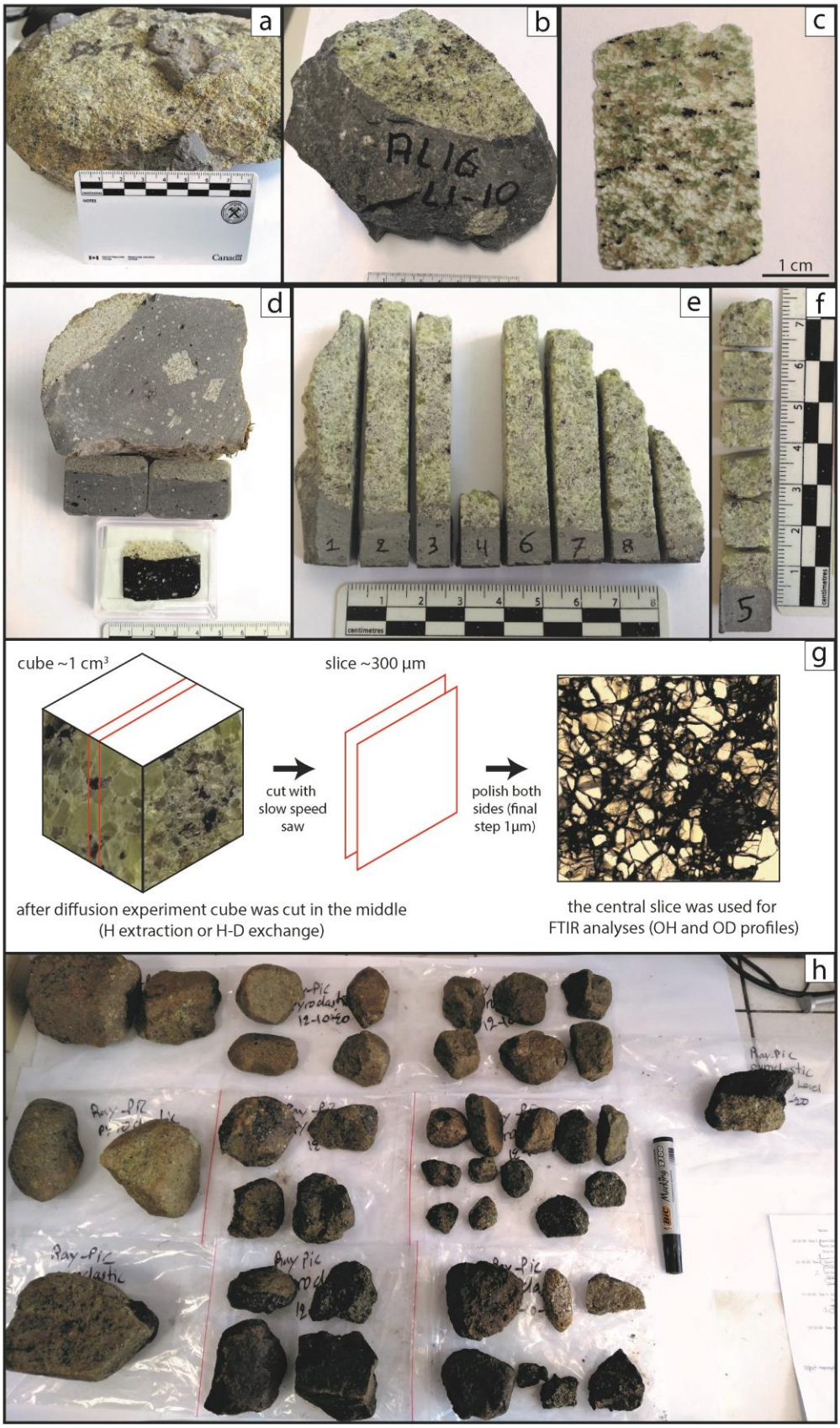
a
b
AL16
LI-10
c
1 cm
d
e
1
2
3
4
6
7
8
f
5
g
cube ~1 cm³
slice ~300 µm
cut with
slow speed
saw
polish both
sides (final
step 1µm)
after diffusion experiment cube was cut in the middle
(H extraction or H-D exchange)
the central slice was used for
FTIR analyses (OH and OD profiles)
h

4.2 Experimental set-up

The experiments performed during this work were hydrogen isotopic diffusion (H/D) exchange experiments with no change in total point defects concentration.

Experiments were performed by stepwise thermal treatment in a cylindrical horizontal furnace supplied with constant gas flow from a mixture of composition 10% D (^{2}H) + 90% Ar. Before entering the furnace, the gas passes through heavy water (D_2O). Bubbling into water allows the control of the pO_2. Continuous flux of gas ensure that gas can be considered as an infinite reservoir thus D content and pO_2 is constant during all the experiments despite the exchange/extraction. Accurate temperatures inside the furnace were measured with a Pt_{100}/Pt_{90}-Rh_{10} thermocouple located at the center of the furnace at less than 2 cm from the samples. The specific thermocouple is considered the most stable in most atmospheres and has an error of ±0.0025 per 1^{o}C, meaning that at 1000 ^{o}C error is ±2.5 ^{o}C. The furnace used has a constant temperature in a range of ± 5 cm of its central part. The total uncertainty on the temperature of experiments is estimated < 5°C. In all experiments, samples (cubes and single crystals) were placed first in a platinum foil container and then in a ceramic holder, which was settled in the centre part of the furnace (Fig. 4.2). . We used opx crystals, as sensors of the progress of the exchange within the xenolith, comparing diffusion profiles measured in single crystals or at the edge of the cubes with diffusion profiles within opx inside the cube not directly in contact with the gas. The gas flux was initiated prior of any temperature rise for 15 minutes period, to ensure saturated environment inside the furnace. Afterwards, temperature was increased at a rate of ~17^{o}C/min, until the final temperature of the experiment. For cooling, the furnace temperature was set to 0^{o}C resulting a cooling rate of 15^{o}C/min in the high-temperature region (the first 200-300^{o}C of decrease) and then continued with a rate around 10^{o}C/min. During temperature steps additional exchange/extraction may occur but it is considered negligible if we compare it with the exchange at the nominal temperature of the experiment (Ingrin et. al. 1995). Cube dimensions were measured up to few μm accuracy with a digital micrometer before and after the experiments in order to check for possible change in the sample geometry of the cubes after annealing experiments (i.e possible expansion due to cracks). In all experiments, no such change was observed. Experimental run conditions for all the samples are presented in the Table 4.1. At the end of each time step experiment, OH/OD content was measured at the centre of the opx single crystal and at the end of each temperature

series, one or more slices of few hundred microns thick were cut from the centre of the cubes for FTIR measurements. The cubes remain unaltered and cohesive after heat treatment and sawing of slices.

The gas in the experiments controls the partial pressures of oxygen (pO_2) and hydrogen (pH_2) or deuterium (pD_2). During the isotopic experiments, hydrogen is moving out of the crystal exchanging with the deuterium of the gas. Deuterium and hydrogen exchange at the surface of the grain to allow equilibration between the rich deuterium gas and the poor deuterium crystal. When exchange is completed, the deuterium content of the crystal is in equilibrium with the deuterium content of the gas. The results would be the same if we were doing the reverse experiment. Oxygen fugacity is constant during the experiment (during the set-point temperature plateau) and controlled by the reaction $D_2O = D_2 + ½\ O_2$ (D_2O in the gas is the result of the saturation of the gas at room temperature though the bubbling into D_2O prior to enter in the furnace).

Experiment type/ gas	Temperature (°C)	Total time after each time steps (' and h)	Cubes #	Single crystal #
-	untreated	-	7d	-
H/D / 10% D	600	10', 90', 15, 45, 135	5b	-
H/D / 10% D	700	1, 4, 12, 36, 108	5a	opx 1
H/D / 10% D	800	8, 16	7a, 7b	opx 5
H/D / 10% D	800	5	3d	opx 2
H/D / 10% D	900	1, 4	6a, 6b	opx 3
H/D / 10% D	900	2	6c, 6d	-

Table 4.1: Summary of the experimental run conditions for the H/D exchange experiments and samples.

During H/D experiments, the temperature and duration of experiments are too low and short respectively to allow other reactions to have a significative impact, like for instance redox reaction to modify notably the concentration of the total H/D-defects in the pyroxenes (this is not necessary true for olivine).

Prior to our experiments, in order to plan the time steps we used the empirical equation:

$$\lambda = 2\sqrt{Dt} \quad (4.1)$$

where λ is thickness (m), D is diffusion coefficient (m^2s^{-1}) and t is time (s). So based on the thickness/length of the diffusion we wanted to achieve and the given diffusion coefficient from previous studies we roughly estimated the time of our experiments.

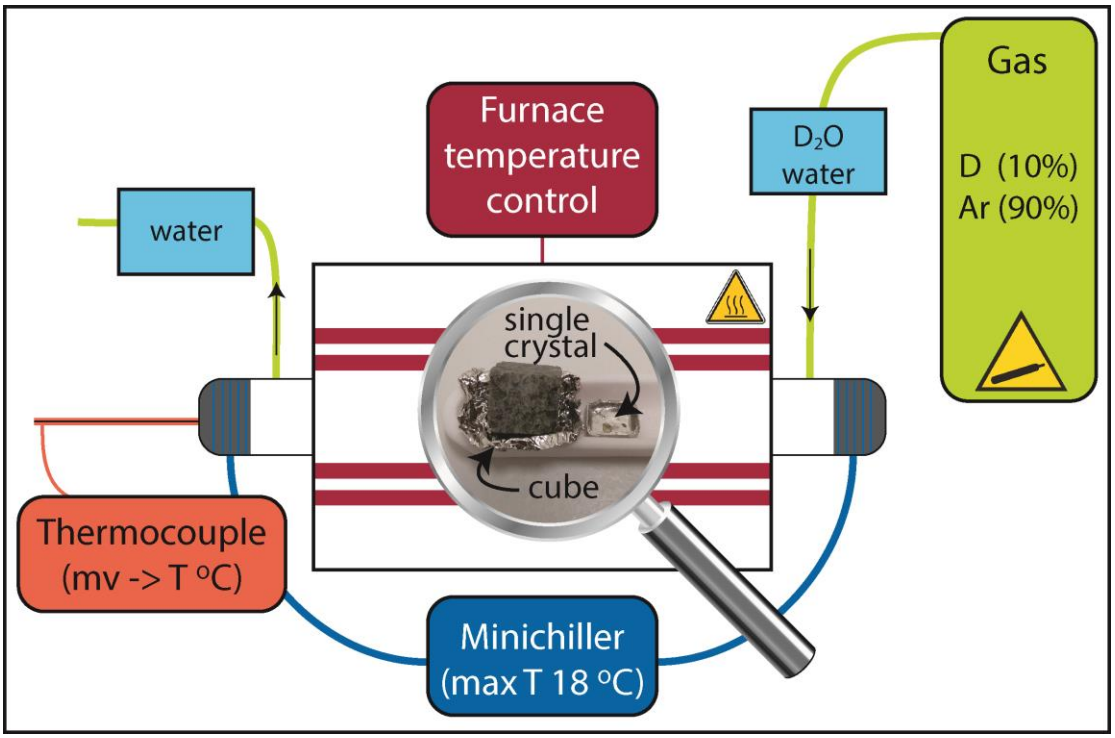

Figure 4.2: Schematic set-up of the experiments and apparatus. See text for more details. The minichiller cool down the metallic parts and o-rings at the edges of the ceramic tube.

4.3 Fourier transform infrared spectroscopy

One of the most popular method amongst scientists for measuring hydrogen diffusion is the infrared spectroscopy. The IR beam interact with the vibrational modes of OH dipole in the sample and produce absorption bands, captured in the IR spectrum. The intensity of these absorption bands are related to the concentration of hydrogen (and orientation of crystal with the IR beam) and several different calibrations have been proposed and used for conversion of the bands into quantitative concentrations. The relative position of the absorption bands in wavenumber is primarily depending on the strength of the O-H bond, which is influenced, by a) the strength of the hydrogen bond and, b) the bond geometry. The benefits of using infrared spectroscopy in hydrogen diffusion studies are a) very high sensitivity (ppm values) and b) the opportunity to detect the different hydrogen (OH^-, H_2O, hydrous phases in inclusions).

Fourier-transform infrared spectroscopy (FTIR) was used to measure the absorption of OH/OD bands in the single crystals, after each time step experiment, and at the end of the experiment in the cube slices. Unpolarized and polarized IR-spectra were collected in transmitted

light using a Bruker's Hyperion 3000 FTIR microscope coupled with the Vertex 70 spectrometer equipped with a single MCT detector and a Focal Plan Array (FPA) detector at LASIR laboratory, CNRS-University of Lille (Fig.4.3a). The FPA is composed of 128 x 128 MCT elements. Measurements were performed using a globar thermal light source, a KBr beam splitter and a 360-degree rotation IR wire grid polarizer on a KRS-5 substrate in the microscope. For each spectrum, 128 scans for background and 256 scans for sample were acquired in the wavenumber range of 600-4000 cm^{-1} with a resolution of 4 cm^{-1} (few analyses were collected in the range 600-7000 cm^{-1}). For the FPA mode, spectrum characteristics were 256 scans for background and 512 scans for sample with 8 cm^{-1} resolution and in the wavenumber range of 800-4000 cm^{-1}. A 15x objective (100x100 μm analysis window) for single MCT analyses, 36x objective (30x30 μm analysis window) for profile analyses and 15x objective (160x160 μm analysis window) for the FPA, were used. Baseline subtraction was performed using a polynomial function between 3800 and 3100 cm^{-1} for OH bands and 2800 and 2400 cm^{-1} for OD bands. These wavenumber ranges may fluctuate by few cm^{-1} in order to better fit with the baseline. Total absorbance (A_{OH}, A_{OD}) was calculated by integration over the wavenumber range of 3100 to 3800 cm^{-1} for OH and 2400 to 2800 cm^{-1} for OD. All spectra were normalized by sample thickness in cm. The lattice overtones (1250–2350 cm^{-1}) were used to identify the orientation of the crystals by comparison with previously published spectra (Prechtel and Stalder 2012) (Fig.4.3b). Small but distinctive differences have been reported in diffusivities along the three different crystallographic axes in natural opx (Fig.4.3c) with γ [001] > β [100] > α [010] (Stalder and Skogby, 2003). Very rare spectra show small bands in the range 2800-3000 cm^{-1} that is characteristic for glue/epoxy substance, remaining in the sample.

In order to determine the OH ppm concentration from the integral absorbance (A_{OH}) there are various Beer-Lambert law calibrations for water in minerals. The Beer-Lambert law states that there is a relation connecting the absorption of radiant energy (attenuation of light) by an absorbing medium. The equation is expressed as:

$$A = \varepsilon l c \quad (4.2)$$

where A is the absorbance (unitless), ε is the molar absorption coefficient ($Lmol^{-1}cm^{-1}$), l is the length of the light path (cm) and c is the concentration of the solution ($molL^{-1}$). In our work we used the calibration of Bell et al. (1995). This mineral-specific calibration has been used widely in natural samples and is based on absorption coefficients from an augite megacryst (Premier Mine

kimberlite, South Africa) for cpx and an aluminous enstatite from a spinel lherzolite xenolith (Kilbourne Hole, New Mexico) for opx. The other candidate for calibration was the wavenumber-dependent calibration of Libowitzky and Rossman (1997) that has been applied for synthetic crystals and was not selected for this work. Error from the measurement of the integral absorbance, which is mainly due to uncertainty on the baseline modelling and subtraction, is between 10-20% of the average A_{OH}. This range of error was calculated by underestimated and overestimated the integral absorbance through two extreme possible baselines and then performing a statistical quantification of the ± values.

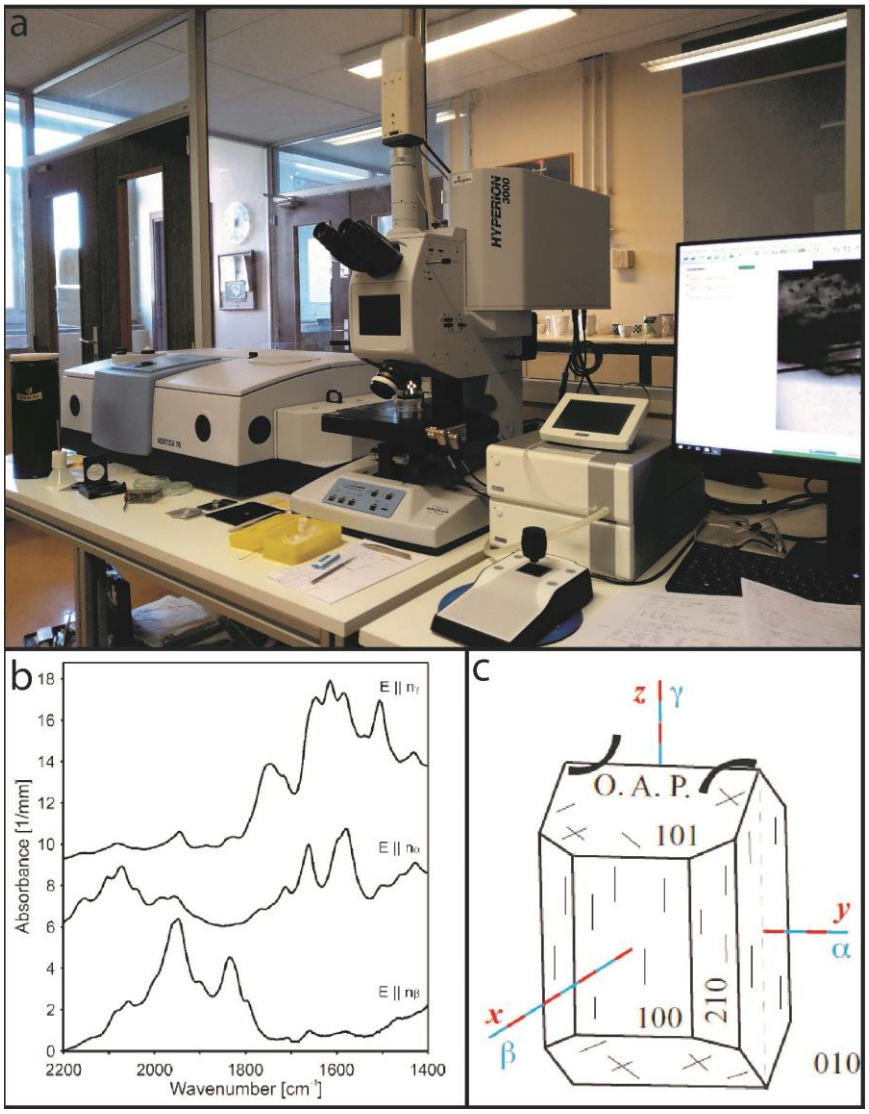

Figure 4.3: a) The Bruker's Hyperion 3000 FTIR microscope with the Vertex 70 spectrometer at LASIR laboratory, CNRS-University of Lille. **b)** Polarized IR-spectra of the lattice overtones of synthetic enstatite. Image from Prechtel and Stalder, 2012. **c)** Enstatite (opx) optical and crystallographic axes. Image from Deer et al., 2013.

Even if it was not the primary objective of the study in the natural samples, the water concentration of olivine was also estimated in some samples. Water in olivine from mantle xenoliths have bands in the infrared absorption spectrum in two regions, 3000-3450 cm^{-1} and 3450-3700 cm^{-1} wavenumber. In most of our samples, we observed no intensity peaks in the first region and calculated total water derived from the integration area of 3450-3600 cm^{-1} based on the Withers et al. (2012) calibration.

4.4 Idefick and numerical modelling with a finite elements approach

To understand and find solutions of the complex geometries and conditions of diffusion in our experiments, we turned to numerical simulations. For this purpose, we used the software "Idefick" developed by Pierre Hirel specifically for this work. Starting from a set of initial conditions, this program performs numerical integration of Fick's second law of diffusion over a finite-element grid, thus simulating the evolution of the concentration in the sample. Fig.4.4 summarizes the workflow of Idefick. Initial parameters are defined in a text document (.txt). These parameters include the properties of the different phases (diffusion coefficients), the size and resolution of the finite-element grid, the boundary conditions, and the desired duration of the simulation. From this initial setup, the program performs the numerical integration, and can write the concentration profile C(x,y) into data files at regular intervals. The program stops when one of the following conditions is satisfied: the specified duration is reached, or the concentration profile does not change anymore. More details about the program are provided in the Appendix B.

Idefick is essential in the process of understanding and obtaining the diffusion coefficients from the concentration profiles we acquired after experiments. We compared experimental diffusion profiles with the ones we modeled with Idefick in an attempt to estimate: 1) the contribution of the lateral diffusion (diffusion not in the direction of the profile) and 2) the contribution of grain boundary diffusion in our experiments.

4.5 GNU Octave programming

In order to evaluate and process our infrared data faster, we developed a source code exclusively for the analysis of FTIR data. We used the free software GNU Octave that is highly compatible with MATLAB. Octave is a software featuring a high-level programming language that is ideal

for this type of task. We used the software to: a) plot and normalize the FTIR spectra, b) subtract the baseline and calculate OH and OD absorbance, c) define diffusion coefficients for profiles and single crystals. Because this code can be useful for future use, we present it with details in the Appendix C. One of the strong advantages of the program is that it can use a whole segment of the spectra, before and after the intensity peaks, to produce an accurate baseline. Nevertheless, extra care was taken and a visual quality check of the polynomial baselines was systematically performed.

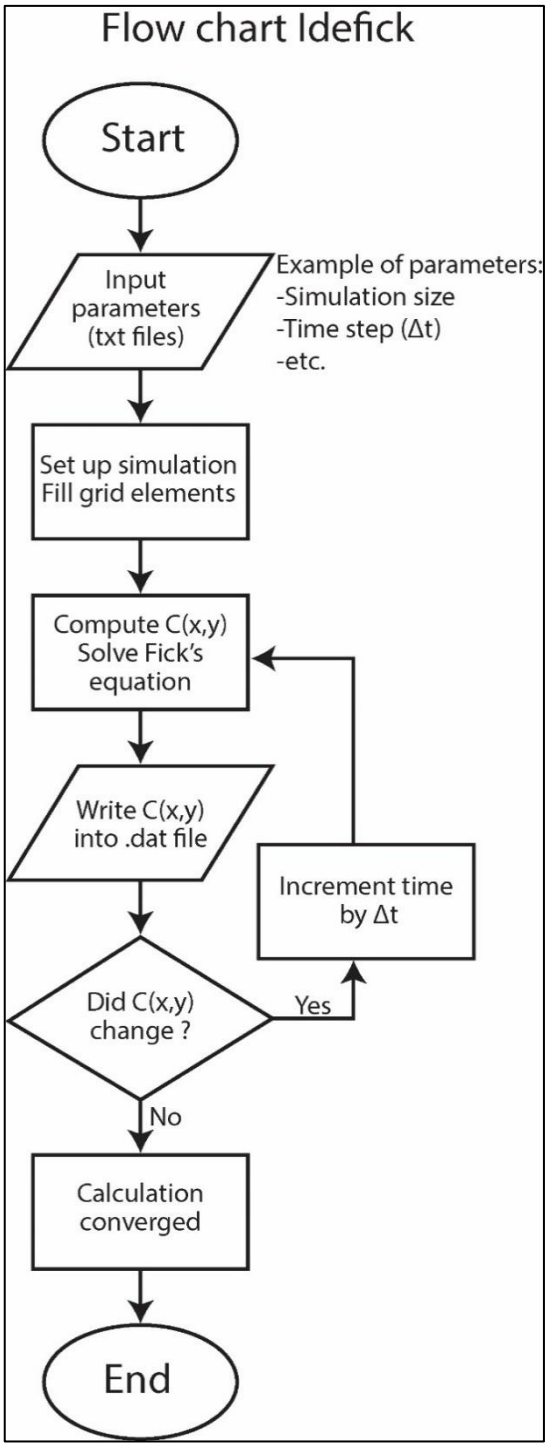

Figure 4.4: Flowchart of the program Idefick.

5. Water content in xenoliths: the effect of magmatic emplacement in hydrogen preservation

In this chapter, we are presenting the results and the interpretations of our work related to the study of natural samples. Basic petrographic characteristics of the samples collected on the two localities (Allègre and Ray Pic) are reported together with the FTIR analyses. In addition, we compared our data with data obtained from previous studies, from xenoliths at the same localities, for consistency evaluation.

We investigate two different natural cases of lava flow structures in an attempt to understand if the emplacement of the lava flows affects the water content in xenoliths and especially in pyroxenes. Allègre quarry provide us with a vertical structure while Ray Pic lava flow is a typical elongated/horizontally one.

5.1 Petrological description

In the duration of 35 FTIR session days dedicated to the natural samples, we obtain more than 1000 points of analysis and checked profiles in ol, cpx and opx crystals from 27 thin sections, derived from 16 xenoliths (Table 5.1). According to basic petrological and microscopic observations, the xenoliths used in this work are classified mainly as lherzolite (13), harzburgite (3) and dunite (1) (Fig. 5.1). The dominant texture present in the samples is protogranular, a granoblastic texture characterized by polygon shape grains and curvilinear mineral boundaries (Mercier and Nicolas, 1975). Some characteristics of the coarse granular and equigranular texture may be present in our samples and exist as an intermediate or mixed texture. Based on the observations a) ol and opx are usually coarse grained and with similar size, b) cpx is frequently of smaller size and often clustered with spl and c) in most of our pyroxene crystals, we observe exsolution textures, we conclude that our texture is more of a protogranular origin (Lenoir et al. 2000). Only one sample (Pyro2) has a porphyroclastic texture. Another characteristic of our samples is that spinel is present in all of them as accessory mineral and usually is found with pyroxene clusters. The igneous host rock of the xenoliths is identified as basalt with typical aphanitic-fine grained texture and only sporadically, we observe few ol or opx phenocrysts in the groundmass.

A petrological study of the xenoliths was not the objective of the study. Detailed petrological analysis of xenoliths from these two localities have already been reported in previous

studies: in Gu (2016) for Allègre samples from the same quarry and Denis et al. (2015) for the xenoliths of Ray Pic. The Allègre xenoliths from Gu (2016) that originated from the same quarry as our Allègre xenoliths have been used to calculate the equilibrium temperatures and pressure. The reported values are ranging between 840-1077°C and 9.3-14.8 kbar based on the two-pyroxene thermometer and the Ca-in-olivine geobarometer from Brey and Köhler (1990). In the same work, results from major elements composition are presented, with Mg# content in ol varying between 89.2-92.4, and $Fe^{T}O$ between 4.6-6.9 for opx and 2.4-3.6 for cpx.

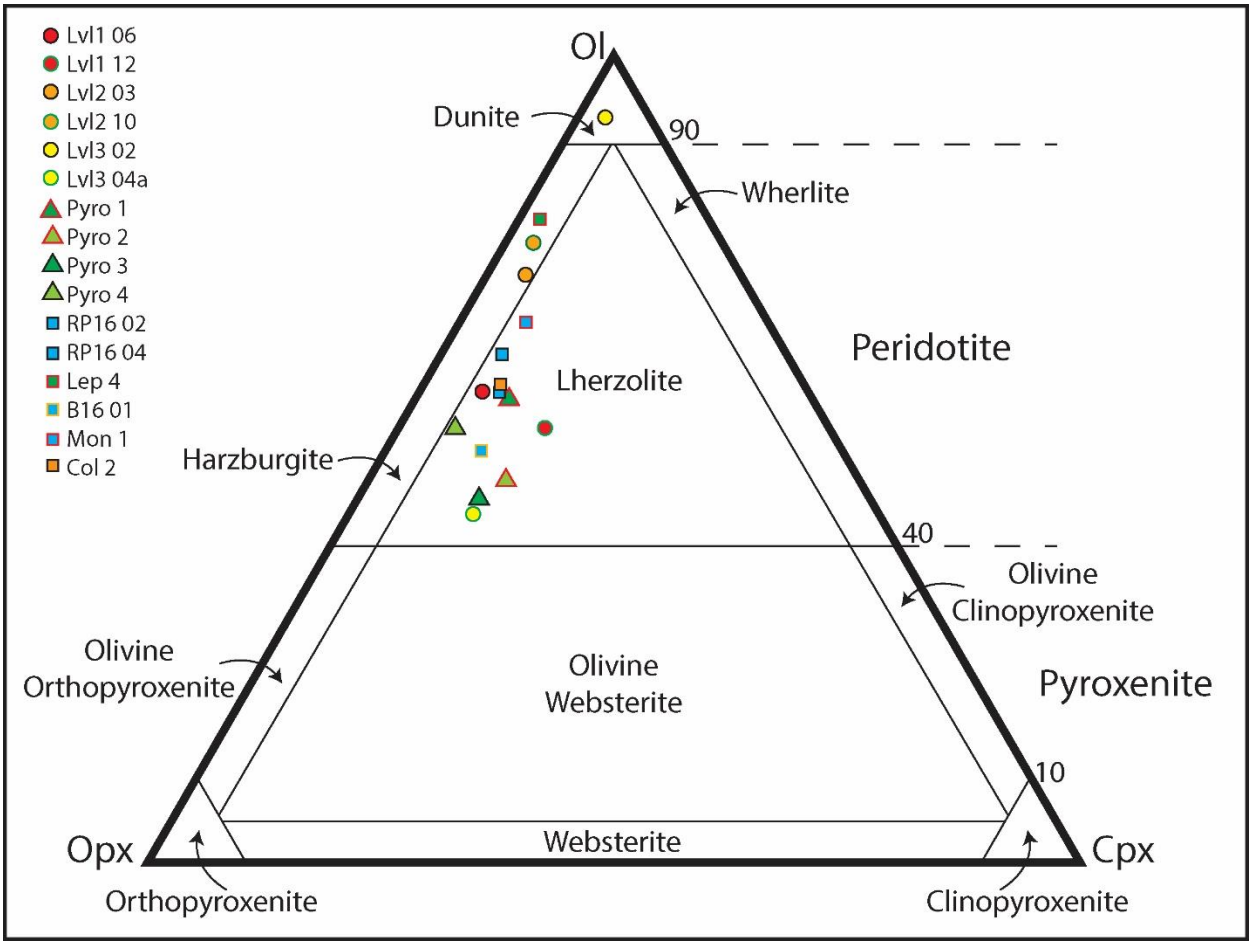

Figure 5.1: Triangular classification diagram. Data in Appendix D. For few samples, like Level 3 02, we do not have many analyses to strongly employ statistic tools. Nevertheless, we are going to use them into our discussion and interpretations.

Location	Sample	Approx. size (cm^3)	Lithology	Texture	Thin sections for FTIR	Thickness (µm)	n	Ol	Cpx	Opx	Profile measurement
Allègre	Level 1 06		Lherzolite	protogranular	2	249, 316	44	3-3	21-21	18-18	Cpx, Opx
	Level 1 12		Lherzolite	protogranular	2	238, 266	94	16-12	32-30	30-26	Ol, Cpx, Opx
	Level 2 03	210	Harzburgite	protogranular	2	215, 235	47	12-11	6-4	25-25	Ol, Opx
	Level 2 10		Harzburgite	protogranular	2	255, 265	57	12-11	14-14	19-17	Ol, Cpx, Opx
	Level 2 07		Lherzolite	protogranular	sample used for experiments (single crystals and cubes)						
	Level 3 02		Dunite	protogranular	1	273	23	10-9	3-3	7-6	Cpx, Opx
	Level 3 04a	160	Lherzolite	protogranular	2	246, 254	93	15-10	27-27	49-44	Ol, Cpx, Opx
Ray Pic	Pyro1	500	Lherzolite	protogranular	1	288	23	3-3	5-5	13-13	Ol, Opx
	Pyro2	220	Lherzolite	porphyroclastic	2	300, 300	29	3-3	12-12	9-8	Opx
	Pyro3	120	Lherzolite	protogranular	2	300, 300	35	8-8	9-9	13-10	Ol, Opx
	Pyro4	120	Lherzolite	protogranular	2	300, 300	35	5-5	12-12	16-12	Ol, Opx
	RayPic16 2	130	Lherzolite	protogranular	2	239, 244	83	15-12	15-15	43-41	Opx
	RayPic16 4	280	Lherzolite	protogranular	1	242	24	6-5	6-5	5-5	Opx
	Lep4	120	Harzburgite	protogranular	2	294, 296	43	12-12	-	28-27	-
	Burz16 01	1500	Lherzolite	protogranular	2	226, 242	150	8-6	38-35	72-67	Ol, Opx
	Mon1	30	Lherzolite	protogranular	1	297	29	6-6	9-9	14-14	Opx
	Col2	20	Lherzolite	protogranular	1	324	44	6-6	4-4	28-17	Opx

Table 5.1: Detailed presentation of the natural samples used in this work. Column n is the total point analyses in each xenolith. First numbers in Ol, Cpx and Opx indicate the selected total analyses to calculate the average values of OH concentration in the corresponding xenolith and second numbers the total number of different grains that were analysed.

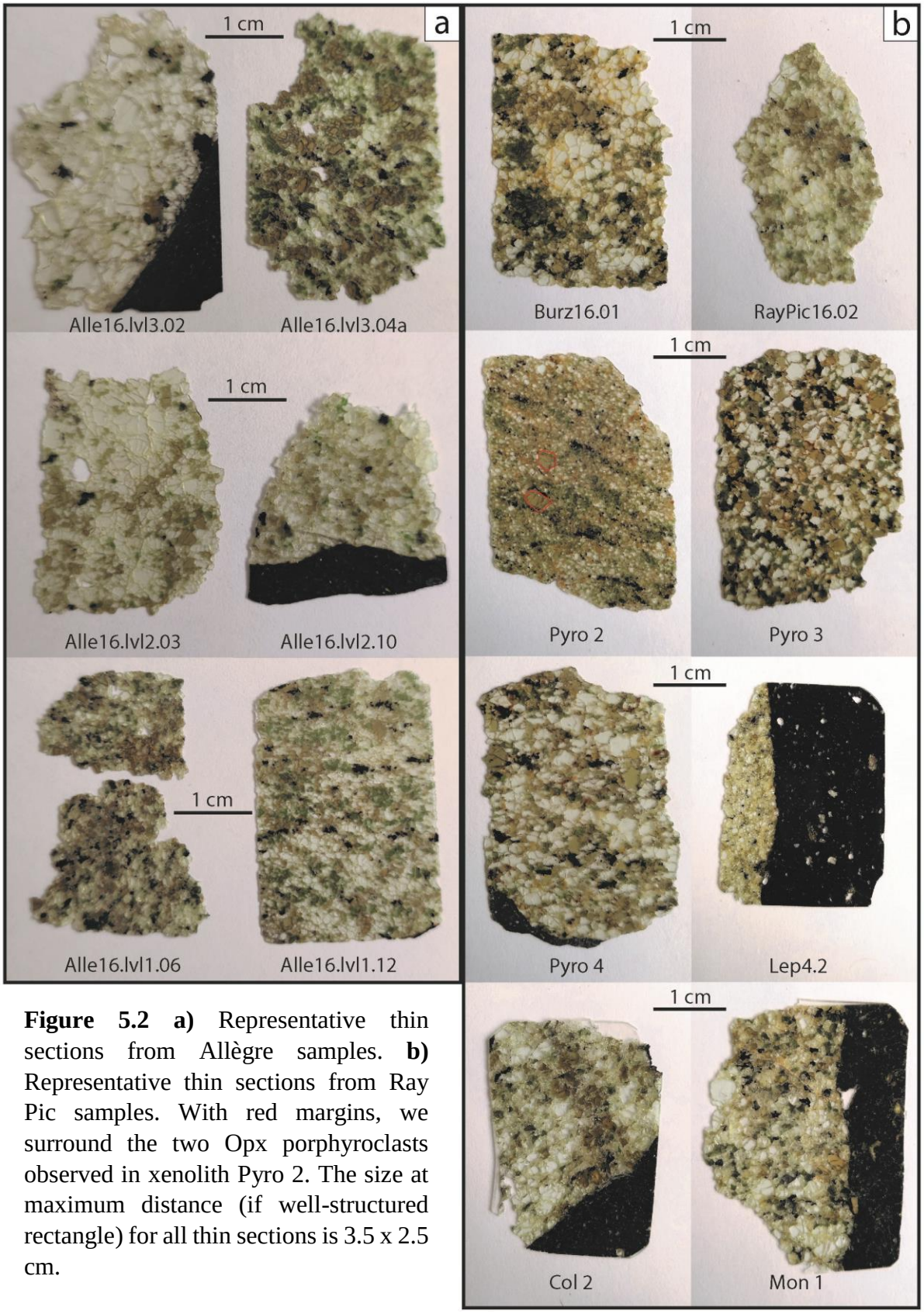

Figure 5.2 a) Representative thin sections from Allègre samples. **b)** Representative thin sections from Ray Pic samples. With red margins, we surround the two Opx porphyroclasts observed in xenolith Pyro 2. The size at maximum distance (if well-structured rectangle) for all thin sections is 3.5 x 2.5 cm.

5.2 Case study Allègre - vertical emplacement in a basalt body - Results

For Allègre we examined six xenoliths, two from each excavation level of the quarry. Results are presented in Table 5.2.

Sample	Ol	Cpx		Opx		H_2O	profiles
	ppm	A_{OH} (cm^{-2})-n	ppm	A_{OH} (cm^{-2})-n	ppm	cpx/opx	
Level 1 06	2.1	323.4-21	$136.8 \pm^{17}_{21}$	236.6-18	$47.8 \pm^{5}_{7}$	2.9	flat
Level 1 12	5.2	320.0-30	$135.4 \pm^{12}_{16}$	182.3-26	$36.8 \pm^{5}_{8}$	3.7	flat
Level 2 03	2.6	257.3-4	$108.9 \pm^{21}_{14}$	185.6-25	$37.5 \pm^{5}_{5}$	2.9	flat
Level 2 10	2.7	399.5-14	$169.0 \pm^{29}_{19}$	258.8-17	$52.3 \pm^{11}_{6}$	3.2	flat
Level 3 02	1.2	289.3-3	$122.4 \pm^{20}_{16}$	173.8-6	$35.1 \pm^{12}_{5}$	3.5	flat
Level 3 04a	1.8	239.6-27	$101.4 \pm^{21}_{16}$	127.1-44	$25.7 \pm^{5}_{5}$	3.9	flat

Table 5.2: Allègre data. Total absorption and ppm values are rounded to the first decimal and n denotes the number of different crystals used to calculate the average A_{OH}. All concentrations are in wt. ppm H_2O.

We first notice that the water concentration of pyroxenes does not seem to be affected by the lithology. The pyroxenes of the dunite and lherzolite samples of level 3 have comparable concentrations and the two harzburgite from level 2 have different water content (Table 5.2, Fig. 5.5). The average spectra of cpx and opx for all samples are plotted in Fig. 5.3. All the spectra of opx have the same signature except one sample, Level 2 03, which has a slightly different cpx spectra, with the 3520 cm^{-1} peak higher than the 3620 cm^{-1} one. We attribute this difference to the small number of Cpx analyzed in this sample and a bias of orientation.

The three lherzolites from Allègre analyzed in Gu (2016) have cpx and opx containing 112-161 wt. ppm and 23-41 wt. ppm water, respectively (Fig. 5.5). Our values are similar. The same calibration method was used in the two studies (Bell et al. 1995). In addition, the spectral signatures of the cpx and opx are also identical to the ones reported in Gu (2016). The spectral signatures appear to be independent of the lithology (lherzolite, harzburgite or dunite; Fig. 5.3).

The water content of olivine is low, between 1 and 5 wt. ppm, frequently just above detection limit for the thickness of the thin sections used (215-316 μm). No peaks were found in the range 3000-3450 cm^{-1} wavenumber and calculated total water content derived from the integration area of 3450-3600 cm^{-1}. We estimate the concentration based on the calibration of Withers et al. (2012).

All the profiles measurements made in cpx and opx grains in the Allègre samples revealed no heterogeneity in the water content distribution in crystals (Fig. 5.4). Therefore, we conclude that water content is homogenous in all crystals.

Although the absolute values of water content are a function of the calibration method applied, our dataset is internally consistent and it can therefore be used to evaluate the possible effect of magma emplacement on the water content of the xenoliths.

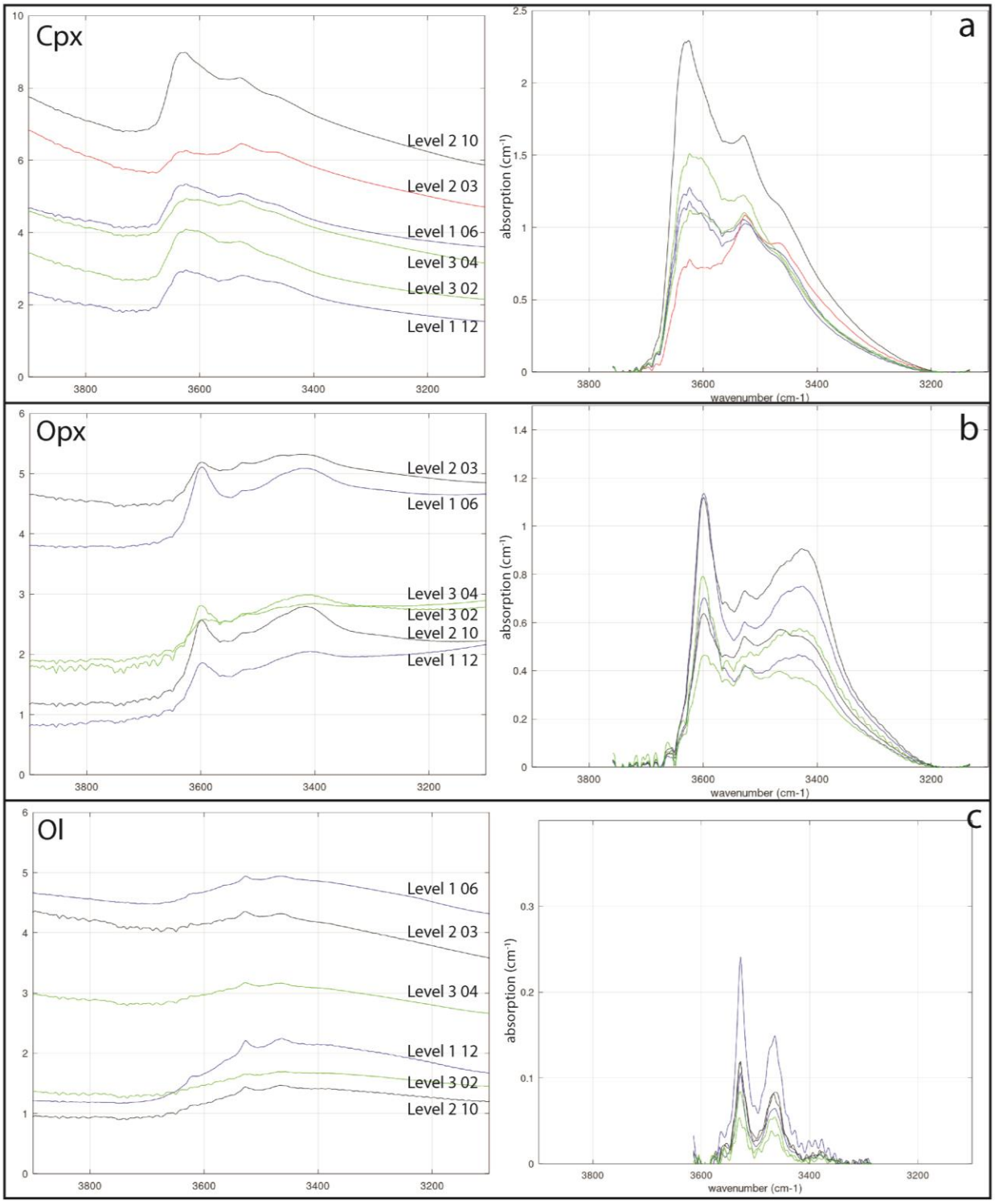

Figure 5.3: Average cpx (a), opx (b) and ol spectra for all the Allègre samples. On the right, we plot the integrated area, that was used to calculate the A_{OH} for each sample.

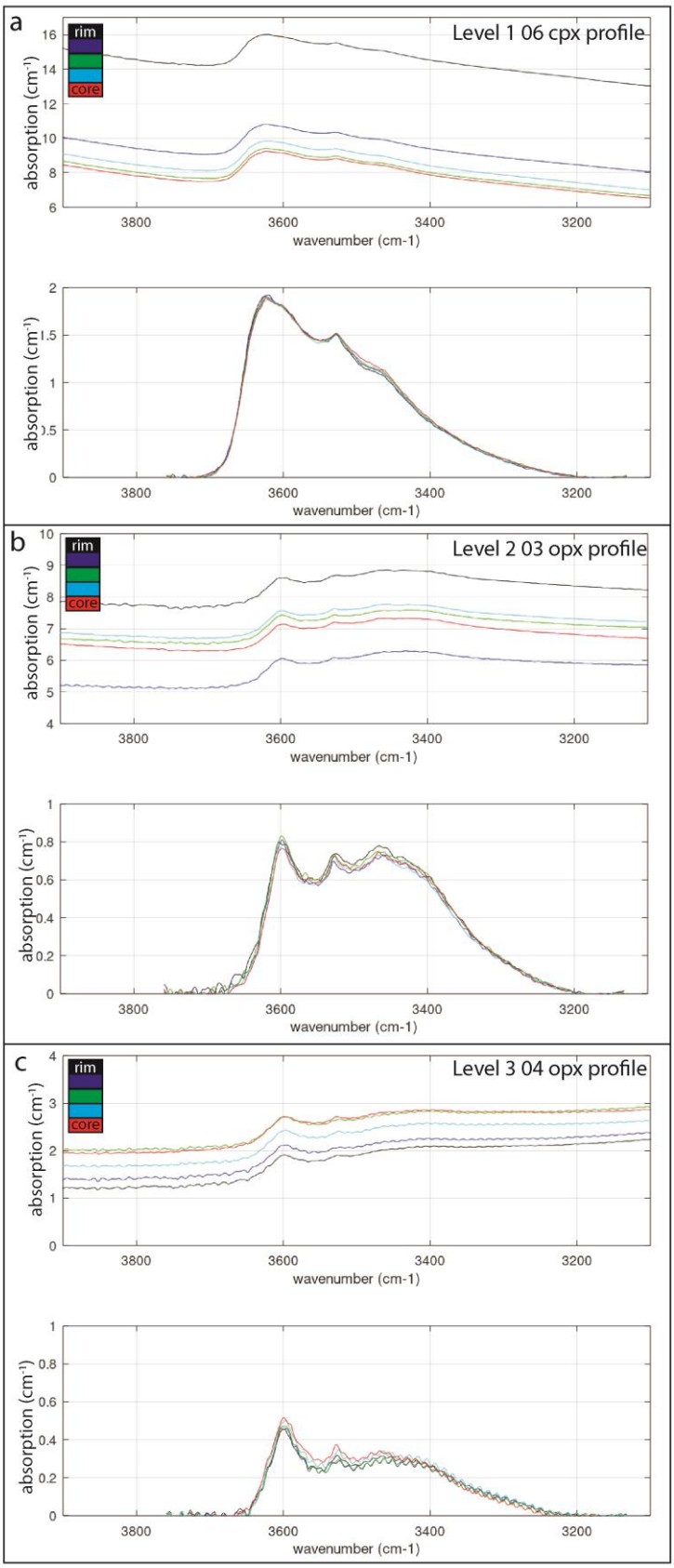

Figure 5.4: a) Profile measurement in a cpx crystal from level 1. **b)** Profile measurement in an opx crystal from level 2. **c)** Profile measurement in an opx crystal from level 3. For all analyses first measurement is 30-40 μm from the rim and then progress towards the core with 50 μm step (spot size 50 x 50 μm^2).

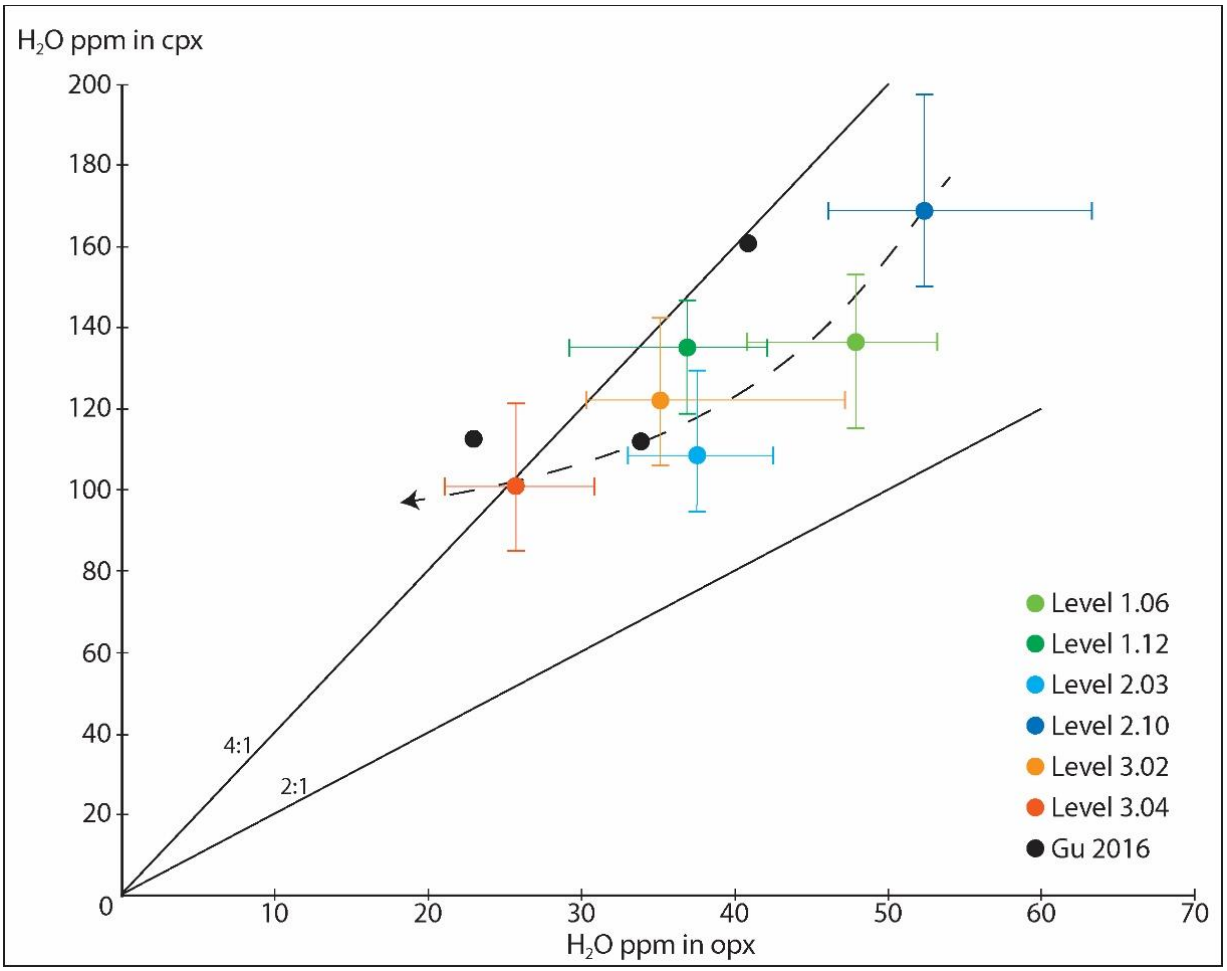

Figure 5.5: Water content in cpx vs opx in Allègre samples with their error bars. Data from Gu (2016) are also plotted for comparison. Dashed line showing a possible direction of the decreased water content in pyroxenes.

5.3 Case study Allègre - vertical emplacement in a basalt body - Discussion

Results presented in the Fig. 5.5 may suggest that the water content of pyroxenes may roughly decreases with the level of the xenolith sampling in the quarry. The most enriched sample from level 2 and the most depleted from level 3 decrease by up to 51% for opx and up to 40% for cpx. It would eventually suggest also a small increase of partition coefficient of water of cpx/opx with the water loss (Table 5.2; Fig. 5.5).

However, if we look at the evolution of concentration in each type of minerals with the location of the sample in the quarry the trend is much less obvious (Fig. 5.6). There is sometime more difference between concentrations of samples from the same level than between levels. Furthermore, the concentration of water in olivine does not match with the differences observed

in pyroxenes. Despite, olivine is known to dehydrate faster than pyroxenes and should be more easily affected by the different cooling rates during emplacement than pyroxenes.

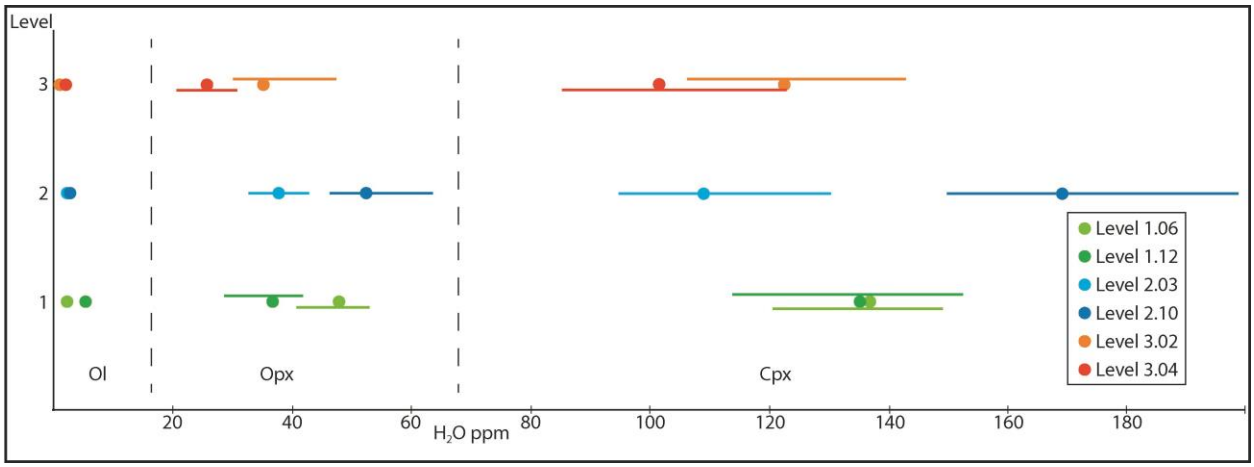

Figure 5.6: Plot of the concentration in cpx, opx and ol vs the levels of the excavations.

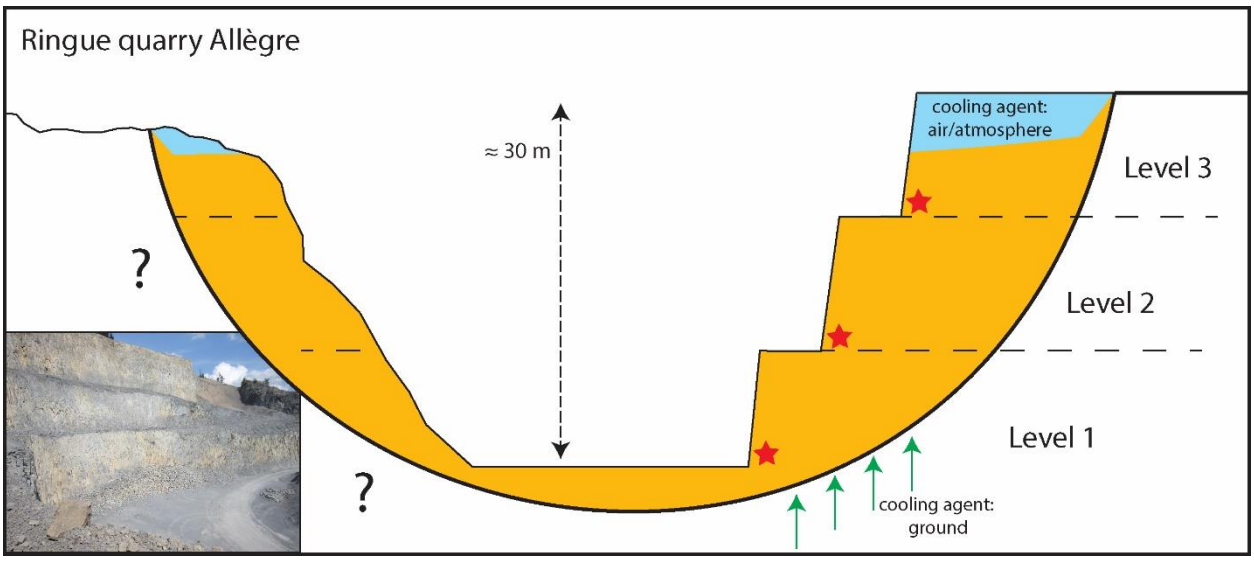

Figure 5.7: Conceptual design of the Allègre quarry with a real photo. Red stars mark the sampling location from the three different excavation levels. Question marks are showing our uncertainty in the actual size of the lava deposit.

During the fieldtrip, no difference in the density of xenoliths in the basalt with the level was observed. There is no evidence that the xenoliths from level 3 had a different history than the ones of the other levels. Although the xenoliths are not all the same in terms of mineral composition, they derived from one magmatic event/eruption, as there is no geological signs in the outcrops in the quarry to support a second event/eruption. Furthermore, as mentioned before,

different rock samples revealed similar water content with identical OH signatures. Considering that we have one magmatic event, the observed differences in water content can be: 1) the result of a different cooling history during the lava emplacement with the included xenoliths or 2) a difference acquired prior to the emplacement and solidification of the body, in a lava lake, a magma chamber or deeper.

It is not clear if the basalt body of Allègre represents a thick lava flow or a lava lake that filled a maar. The cooling conditions and solidification of the two scenarios can be slightly different due to the different boundary conditions (see for instance, Shaw et al. 1977; Peck, 1978; Philpotts and Ague, 2018). In the beginning, there is heat loss from the contact with the atmosphere on the top and the ground in the bottom, resulting in solidifying the outer crust. This outer crust acts as an insulator for the core lava flow. Except the flow thickness, other important factors are wind speeds, rainfall, air and ground temperatures and lava's chemistry (composition, vesiculation, etc.). Roughly, the solidification of a basalt body 10 to 30 m thick can take several years with a slower temperature decrease after solidification (less than 50°C per year; Shaw et al. 1977; Peck, 1978; Wittmann et al. 2017; Philpotts and Ague, 2018).

We ignore the total thickness of the basalt outcrop, what is sure is that there is still basalt present below level 1 (Fig. 5.7). However, considering that the event is recent, the top of the quarry roughly indicates the location of the surface of the body just after its emplacement. Therefore, we can assume without risk that the main source of cooling of that part of the body exposed in the quarry was the very top surface. The cooling rate of level 1 and 2 was higher than the one of level 3 itself. This hypothesis is also confirmed by the progressive disappearance of the well-defined structure of the columnar structure of the basalt to a more disorganized from the level 1 to the level 3 (see Fig. 5.8) The propagation of the solidification was definitely downward in this part of the basalt body sampled.

However, the absence of diffusion profiles in the pyroxenes of the xenoliths in the samples suggests that the effect of the difference of cooling within the basalt body during solidification has negligible effect on the final water content. How it would have been possible to reset the water content of the pyroxenes in the xenoliths without leaving traces of unachieved exchange in any level through diffusion profiles? It does not mean necessarily that the concentration of water inside pyroxenes has not been reset in contact with the basalt at some stage, but if it happens, it was prior the solidification of the basalt body.

The significant difference of water content in pyroxenes from xenoliths at the same location in the quarry and comparable lithology like for the two samples in level 2 (Lev2 03: 108.9 and 37.5 wt. ppm for cpx and opx; Lev2 10: 169.0 and 52.3 wt. ppm for cpx and opx) suggests that the origin of the difference is not link to the immediate location of the xenolith and therefore was acquired before the solidification. It could seem that the concentration of water in pyroxenes from the upper level of the quarry (Level 3) is slightly lower than in the other levels. However, the two xenoliths of this level are the ones with the extreme lithology and the differences still remains within the errors bar. The difference is therefore not significative.

The water content of olivine seems to point out toward a progressive water loss toward the surface (from level 1 to level 3). This does not fit with a faster cooling of the levels closer to the surface. However, it could fit with a stratified degassing of a lava lake.

Finally, the observations made reveal no evidence of water loss during the cooling of the basalt after its emplacement and progressive solidification. The water concentration of pyroxenes seems to be independent of the position of the xenolith in the basalt body while the one of olivine may have been affected by a late stage of degassing in the lava lake. At least, it means that if the outcrop represents a frozen lava lake, no water exchange between the pyroxenes and the lava has been recorded since the convection in the lake has stopped. The origin for the differences between pyroxenes in the xenoliths from the same level, should be from events that occurred prior possible homogenization with the fluid lava lake.

Figure 5.8: Outcrop photo (zoom in) showing the better-structured prismatic-columanr basalt from the bottom, while the top part is more disorganized, entablature basalt.

5.4 Case study Ray Pic – pyroclastic deposit and evolution along a lava flow - Results

For Ray Pic we examined ten xenoliths, four sampled from a pyroclastic deposit on the east side of the volcanic edifice, nearby the cascade of Ray Pic and six sampled along the basaltic flow at different distances from the volcanic center (Fig. 5.12). Nine xenoliths are lherzolites and one (Lep4) is a harzburgite. Results of FTIR measurements are presented in Table 5.3. Major elements from the surrounding basalt are presented in Table 5.4 and trace elements in Appendix D1. All results from the xenoliths sampled in the pyroclastic products are enriched in water content in comparison with the samples from the lava flow (Table 5.3, Fig. 5.11).

Sample	Ol	Cpx		Opx		H_2O	profiles
	ppm	A_{OH} (cm^{-2})-n	ppm	A_{OH} (cm^{-2})-n	ppm	cpx/opx	
Pyro1	11.9	882.7-5	$373.5 \pm^{29}_{32}$	333.4-13	$67.4 \pm^{9}_{5}$	5.5	flat
Pyro2	4.8	846.3-12	$358.1 \pm^{40}_{37}$	348.1-8	$70.4 \pm^{6}_{5}$	5.1	flat
Pyro3	3.3	885.4-9	$374.6 \pm^{26}_{27}$	459.9-10	$93.0 \pm^{9}_{9}$	4.0	flat
Pyro4	5.5	807.2-12	$341.6 \pm^{25}_{32}$	453.1-12	$91.6 \pm^{10}_{11}$	3.7	flat
RayPic16 02	≤ l	493.9-15	$209.0 \pm^{38}_{33}$	229.4-41	$46.4 \pm^{11}_{8}$	4.5	flat
RayPic16 04	≤ l	547.2-5	$231.6 \pm^{30}_{25}$	266.8-5	$53.9 \pm^{11}_{6}$	4.3	flat
Lep4	≤ l	-	-	187.4-27	$37.9 \pm^{3}_{4}$	-	-
Burz16 01	≤ l	428.1-35	$181.1 \pm^{22}_{20}$	273.4-67	$55.3 \pm^{12}_{6}$	3.3	flat
Mon1	≤ l	637.6-9	$269.8 \pm^{22}_{23}$	245.1-14	$49.5 \pm^{5}_{5}$	5.4	flat
Col2	≤ l	244.5-4	$103.4 \pm^{9}_{12}$	152.0-17	$30.7 \pm^{2}_{4}$	3.4	flat

Table 5.3: Ray Pic data. Wt. ppm H_2O values are derived from the same calibration than for Allègre sample; n denotes the number of different crystals used to calculate the average A_{OH}.

All the spectral signatures of cpx and opx are similar except the ones from two samples, Burz16 01 and Col 2 (Fig. 5.9). Most of samples have spectral signatures dominated by the band at high frequency, which is the most frequently observed signature in mantle xenoliths (type 1). In the two samples Burz16 01 and Col, at contrary to others, the high-frequency band is not the dominant one. The behavior is the same for cpx and opx. The band at 3520 cm^{-1} becomes dominant in cpx and the doublet at 3570 and 3520 cm^{-1} becomes dominant in opx. These particular band signatures (type 2) have been already observed in several places. Its end-member has been observed in pyroxenite xenoliths from the FMC (Azevedo-Vannson et al. 2021) and a progressive change of signature has been identified among peridotite xenoliths from the same volcanic field of

Nógrád–Gömör (Patkó et al. 2019). The same dichotomy of signatures has also been observed in mantle xenoliths from different sites of Southern Patagonia in Argentina (Demers-Roberge et al. 2021). In these studies, like here for Col's sample, the pyroxenes with signature closer to type 2 have a lower water content than pyroxenes of type 1.

It is interesting also to notice the presence of two small bands at 3685 and 3710 cm^{-1} in several cpx spectra. They are clearly visible in three samples (Pyro3, Pyro4, Mon1) and are suspected to be related to the presence of amphibole lamellae (Ingrin et al. 1989, Skogby et al. 1990). They are probably of pargasite composition, which has dominant OH bands at the same frequencies (see Della Ventura et al. 2003). Despite we did not observe macroscopic amphiboles in the thin sections, it is coherent with the observation of pargasite in some of the Ray Pic xenoliths studied by Denis et al. (2015). The same bands were also observed in the spectra of cpx in a harzburgite sample studied by these authors (sample 13RP14).

For olivine, we can divide the spectra into two groups a) the pyroclastic samples and b) the depleted lava flow. The pyroclastic samples have a more common signature with peaks at 3230, 3527 and 3573 cm^{-1}, a signature akin with olivines from Denis et al. (2015). The samples of group 2 have water concentrations below detection (≤1 wt. ppm H_2O, no peaks); flat average spectra are shown for Lep, Burz, Mon and Col in figure 5.9. We specifically extracted and prepared six single olivine crystals from Burz to investigate the water content on thicker grains (thickness ranging 3 to 6 mm). The olivines of sample Burz 16 01 had a concentration of 0.32 wt. ppm H_2O.

Plot of water concentrations as a function of the distance from the source of the basalt flow shows no clear correlation of the water content with the distance from the source (Fig. 5.10). In fact, the water content of opx from the basalt flow looks relatively constant all along the valley. Samples RayPic, Lep, Burz and Mon have an average concentration of 46 ± 9 wt. ppm H_2O for opx and 226 ± 44 wt. ppm H_2O for cpx. The dispersion of data is low for opx and cpx, close to the value of individual error bars. All concentration values of olivines from the lava flow have ≤ 1 ppm H_2O.

Fig. 5.11 shows that the cpx from the pyroclastic deposit have relatively constant water concentrations (358 ±17 wt. ppm H_2O) but slightly more variable concentrations in opx (80 ±13 wt. ppm H_2O), with cpx/opx ratios between 3.7 and 5.5. The study by Denis et. al. (2015) reported water content in Ray Pic xenoliths, with cpx containing 335-623 ppm, opx 68-171 ppm and ol 4.4-12.1 ppm, values that are compatible with the ones of the pyro samples.

Sample	SiO_2	Al_2O_3	Fe_2O_3	MnO	MgO	CaO	Na_2O	K_2O	TiO_2	P_2O_5	Total
RayPic16 02	45.03	12.98	11.17	0.20	11.95	9.48	4.53	1.86	2.09	0.72	99.74
Lep 4	44.49	13.08	11.53	0.20	11.65	9.25	4.21	1.95	2.17	0.75	99.32
Burz16 06	45.68	13.09	11.32	0.20	11.59	9.16	4.33	2.01	2.14	0.74	100.16
Mon 1	44.50	13.16	11.42	0.20	11.91	9.44	3.71	1.70	2.17	0.74	100.01
Col2	44.78	13.18	11.44	0.20	11.21	9.52	4.29	1.81	2.18	0.76	99.48

Table 5.4: Ray Pic basalt data. All values are in wt %. There was not enough material to analyze basalt surrounding sample Burz16 01 and therefore we picked the basalt from another sample at the same location.

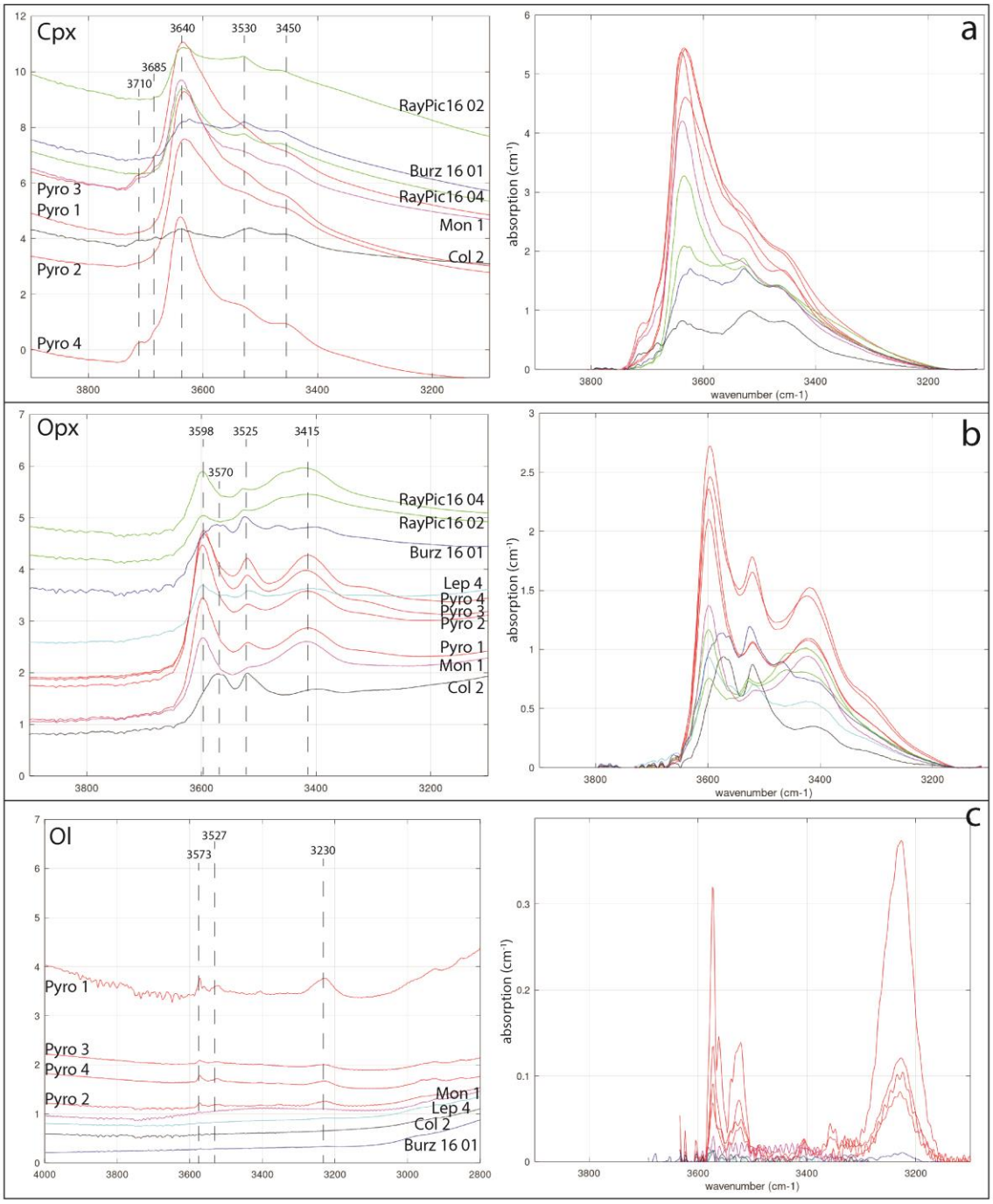

Figure 5.9: Average cpx (a), opx (b) and ol (c) spectra for all the Ray Pic samples. On the right, we plot the integrated area.

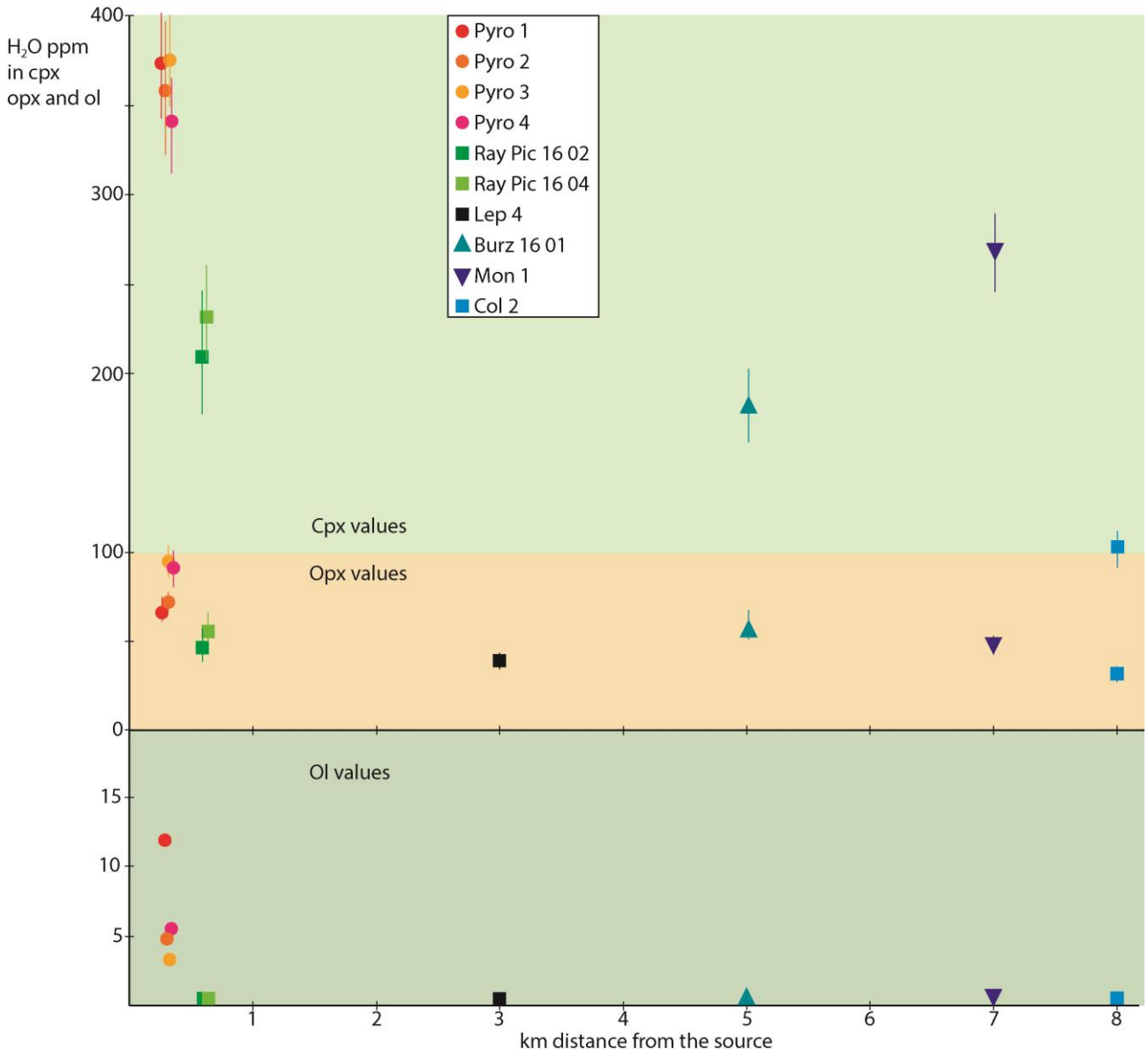

Figure 5.10: Water content in cpx, opx and ol in Ray Pic samples versus their distance from the source.

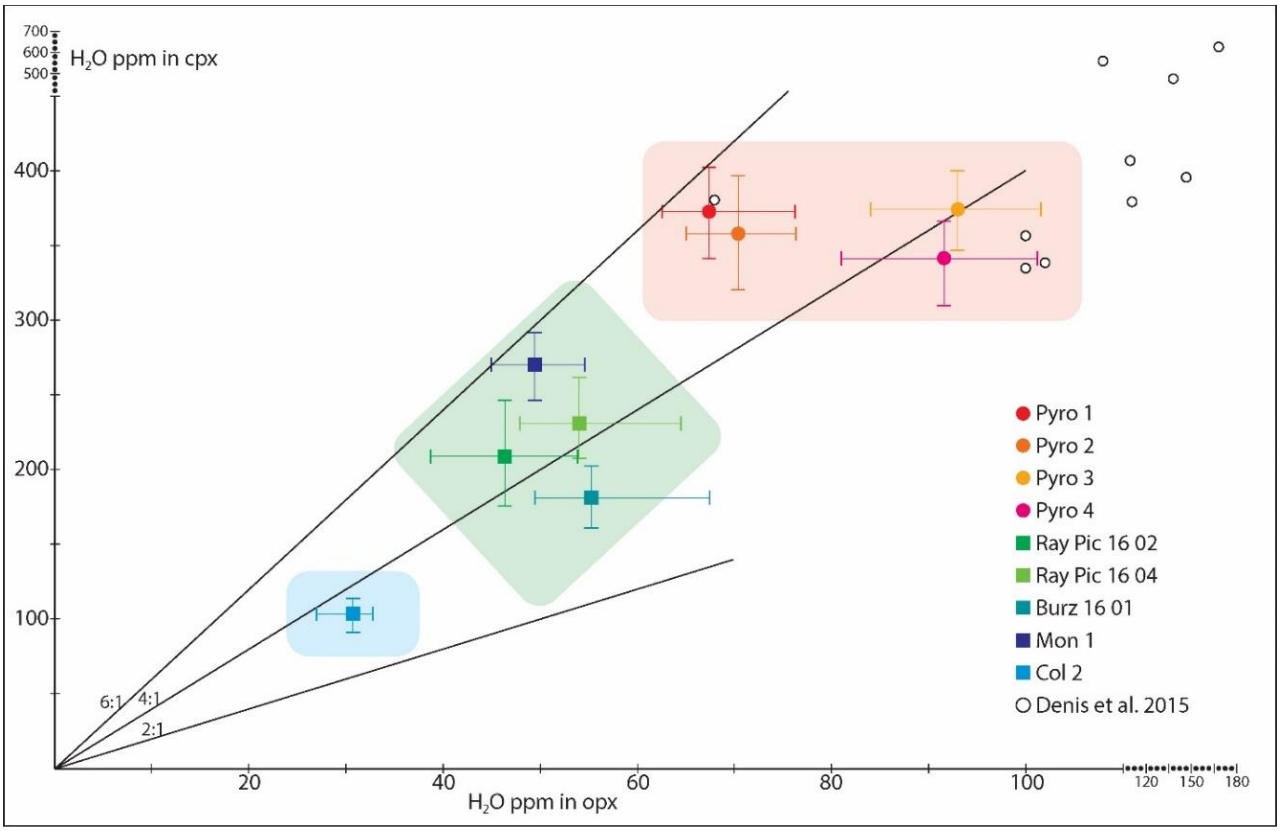

Figure 5.11: Water content in cpx vs opx in Ray Pic samples with their error bars.

All results from the pyroclastic deposit are enriched in water content in comparison with the samples from the lava flow (Fig. 5.11) in cpx, opx and ol.

5.5 Case study Ray Pic – pyroclastic deposit and evolution along a lava flow - Discussion

Samples included in basalt

The chemical analyses (both major and trace elements) performed on basalt bodies where the different samples have been collected, shows no significative differences (Table 5.4, Appendix D1). It confirms that we have sampled the same lava flow. Basalt from the lava flow where samples RayPic16, Burz16 and Mon were collected has a well prismatic structure, while for samples Lep and Col the prismatic structure is less visible (Fig. 5.12). It may suggest that the latter two samples were collected from a level in the lava flow shallower than the ones where prismatic structure formed during solidification. However, the water content of opx in Lep sample was not significantly different of the ones of other samples from the lava flow with the same type of signature (type 1). Unfortunately, due to the small size of the opx it was not possible to measure

profiles in this sample. Nevertheless, considering the data collected, there is no evidence that the samples from these two outcrops had loss water compared to the others. The lower concentration observed in the sample from Col is attributed to the general trend of type 2 spectra, which have lower concentrations than type 1.

Therefore, there is no clear trend of evolution of water content in minerals of the xenoliths with distance from the source of the lava flow or in different locations inside the basaltic flow. These results are in full agreement with what we observed in the case of Allegre. The emplacement and solidification history of the basalt bodies does not alter the initial water content of pyroxenes (and probably olivine too) acquired prior the eruption.

Samples from the pyroclastic deposit

At contrary, the difference between lava flow and pyroclastic samples is evident. The water concentrations of pyroxenes from the pyroclastic deposit are 60 % higher than the ones from the basalt at the waterfall (Ray Pic samples) and even more if we compare with some of the pyroxenes analyzed in Denis et al. (2015). The depletion of water in olivines from the basalt compared to the olivines from the pyroclastic deposit is even stronger with more than 300% decreases. There was not enough basalt material surrounding the xenoliths from the pyroclastic deposit so we ignore if the composition of the magma involved had the same composition than the basalt surrounding the other samples along the river. However, even if the two eruptions were not exactly the same, the events were probably contemporaneous and the hydration of the lithospheric mantle below has certainly not drastically changed between the two events. Therefore, we must conclude that the xenoliths in the basalt flow had lost part of their water and were re-equilibrated at lower water fugacity compared to the xenoliths from the pyroclastic deposit. We have shown before that the emplacement of the flow has not significantly affected the water content of the xenoliths of Ray Pic, like in Allègre event. The modification of the water content of the pyroxenes is most probably due to exchange with the magma prior the eruption. It is frequently argued that the sampling of xenoliths among pyroclastic is more reliable than in basalt flow because they are rapidly quenched compared to the later. Our study on the impact of the cooling of basalt flows shows that the effect of basalt cooling on water content of xenolith is limited. It points out, another explanation for the origin of the difference between the two set of data: a complete re-equilibration with a largely degassed magma just prior the eruption for the xenoliths embedded in the lava flow (no profiles

observed) and a re-equilibration with a less (or not) degassed magma for the xenoliths in the pyroclastic deposit. The effusive nature of the basalt flow compared to the explosive one that characterize production of pyroclastic products is generally a sign of a more degassed magma. It makes sense, but to our knowledge, its impact on the water content of the xenoliths was not clearly demonstrated.

A consequence of this result may have a wide impact. It seems easy to completely re-equilibrate the water content of xenoliths along successive eruptions. The water content of the magma settled in the crust may evolve during the eruption cycle of a volcano. Even xenoliths sampled in products from explosive eruptions may have re-equilibrate with a magma that was already partially degassed. It means that data collected from many xenoliths may represent only a lower limit of the water content of the lithosphere, not necessarily the true value. Another interesting observation from the study comes from the observation in Col and Burz16 01 of pyroxenes with spectral signatures of type 2. It is particularly interesting because it proves that despite the slow cooling of the basalt flow and a complete re-equilibration of the total water content of the xenoliths prior eruption, the difference of the spectral signatures of pyroxenes was not erased. It shows that these signatures are inherited from previous equilibration and very probably from deeper events. It raises hope, after our moderately negative conclusion about the total water 'memory' of mantle xenoliths.

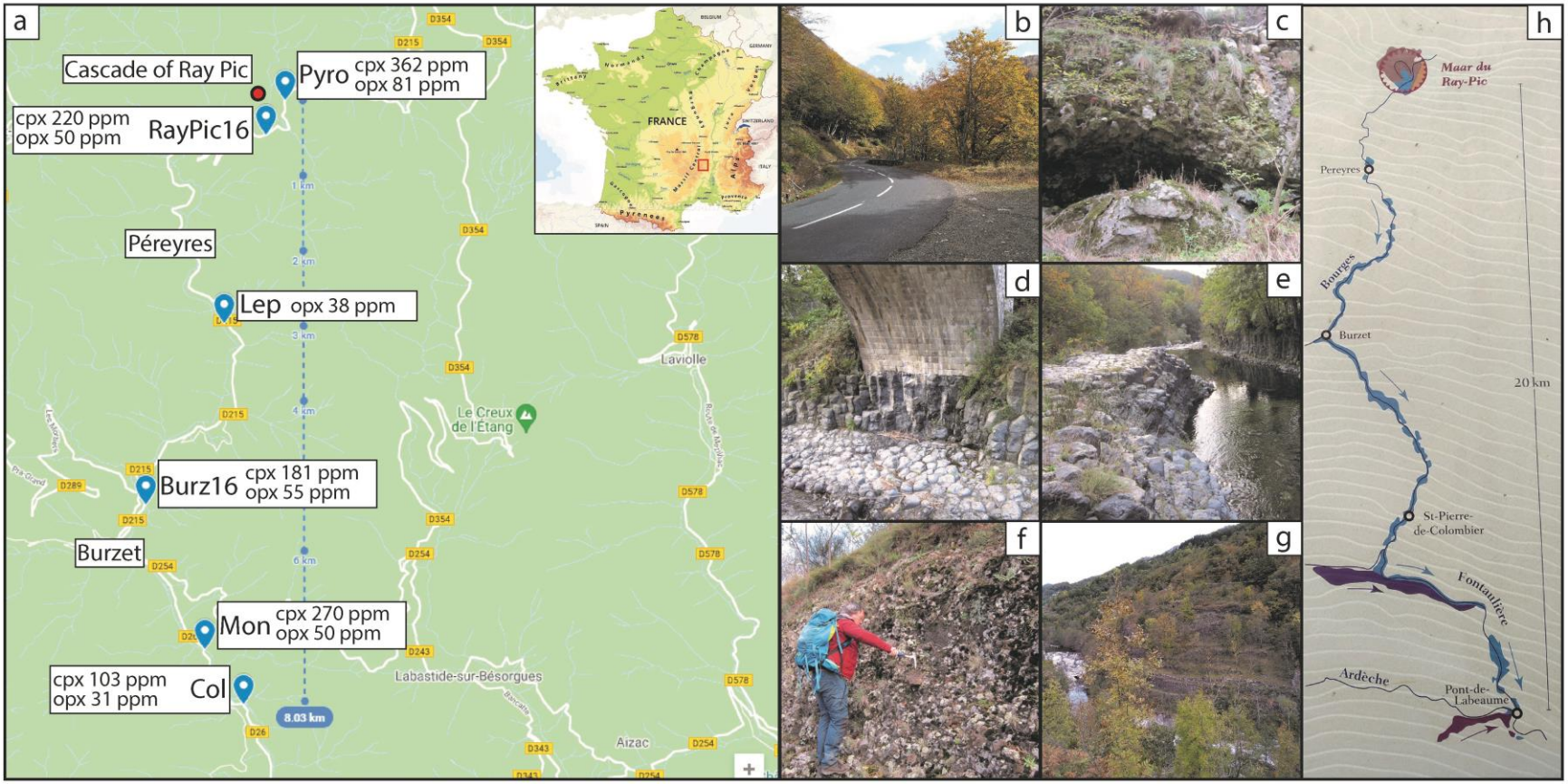

Figure 5.12: a) Broader map of Ray Pic with marks on the sample localities and the water content in opx and cpx. **b)** View of the road followed for sampling the pyroclastic samples. **c)** Le Peyral, location of Lep 4 sample. **d,e)** Monteil bridge, location of Mon 1 sample. **f, g)** Collanges, location of Col 2 sample. In f) we can see a similar outcrop from where we sampled and in g) is the opposite view from the outcrop, showing our level in relationship with the river. **h)** Schematic presentation of the Ray Pic lava flow from the information board in the Cascade Ray Pic touristic site.

5.6 Conclusion

In general, so far, scientists have not found a solid straight correlation between major element composition and hydrogen content in pyroxenes. This difficulty may be derived because of the different factors that control the incorporation of water in the mantle xenoliths such as, temperature, pressure, chemistry, previous lithospheric history, eruption dynamic and conditions of emplacement volcanic material. A good overview on the topic is the review paper of Peslier (2010) where is compiled data from water content in mantle pyroxenes, but not strong correlation was found.

We observe the same situation regarding hydrogen content in pyroxenes from mantle xenoliths and their magma emplacement. There is no evidence that cooling and solidification of basaltic flows affect the total water content of pyroxenes in mantle xenoliths. The studies of samples from a frozen lava lake (Allègre) and basaltic flow along a river on more than 20 km long (Ray Pic) confirm it. An important result of our study confirms in the case of Ray Pic that the total water concentration of pyroxenes is strongly affected by the degree of degassing of the magma prior to eruption and that this amount can change along the full sequence of eruption of a volcano. However, the spectral signatures of pyroxenes do not seem to be affected by this degassing and pyroxenes with signatures of type 1 and type 2 can coexist within a same event and preserve signatures acquired earlier (Ingrin, 2021).

6. Hydrogen isotopic diffusion experiments and numerical modelling

In this chapter, we will present the results and interpretations from the H/D diffusion experiments and the numerical modelling. Prior to the experiments, we prepared single crystals that were used in the experiments as sensors of the exchange process and a cube slice from an untreated cube, which was used as a reference for comparison with the cubes after the experiments.

6.1 Results

Experimental run conditions for all the samples are presented in Table 6.1. In total, we performed six H/D experiments at 600, 700, 800 and 900ºC lasting from 2 hours to 135 hours.

Analyses performed in thin sections of various xenoliths from the same locality at various distances from the edge of either the sections or the crystal (profiles, see chapter 5) show that homogeneous distribution of OH inside pyroxenes is a general feature. From the untreated cube and the single crystals, that both derived from the sample Allègre Level 2 07, we found that Opx have 39±5 wt. ppm H_2O (n=10, Appendix D2). It confirms that the xenolith is comparable to the rest of the samples from the same locality. In addition, the pyroxene single crystals were carefully inspected to confirm the absence of any mineral alteration. The cube slices after annealing show the same texture as the reference untreated one. No specific features induced by the heat treatment or formation of new cracks were observed (Fig. 6.1).

T (ºC)	Total time after each time steps (' and h)	Cubes #	Single crystal # and thickness	Cube slices # and thickness
untreated	-	7d	-	7d (324µm)
600	10', 90', 15, 45, 135	5b	-	5b (295µm), 5bb (314µm)
700	1, 4, 12, 36, 108	5a	opx 1 (151 µm)	5ai (297µm), 5aii (306µm), 5ac (303µm)
800	8, 16	7a, 7b	opx 5 (370 µm)	7a (323µm), 7aa (357µm), 7b (338µm), 7b2 (315µm)
800	5	3d	opx 2 (325 µm)	3d (327µm)
900	1, 4	6a, 6b	opx 3 (219 µm)	6a (335µm), 6b (314µm), 6b2 (347µm)
900	2	6c, 6d	-	6c (324µm), 6d (322µm)

Table 6.1: Summary of H/D exchange experiments and samples.

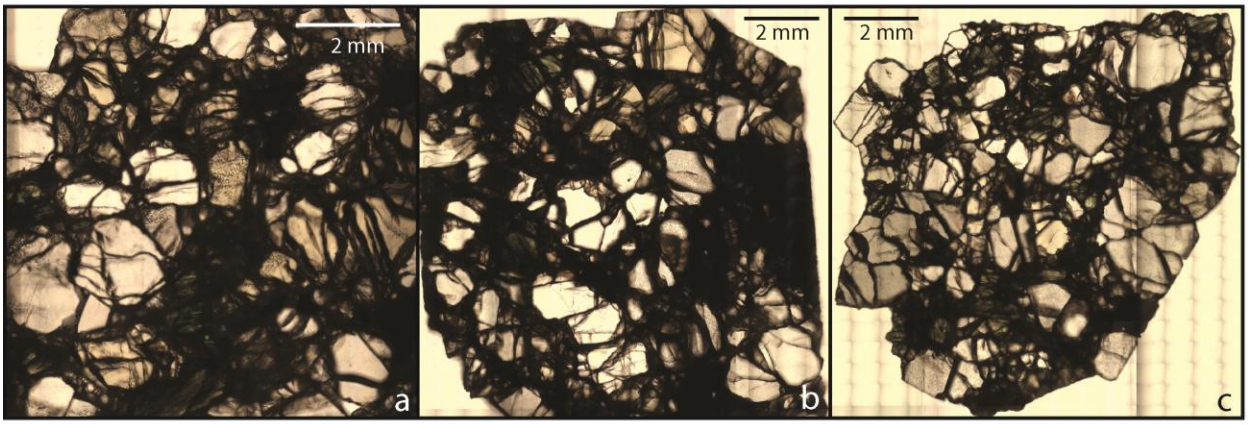

Figure 6.1: Cube slices comparison. White to grey is ol, brown to light brown is opx and light green is cpx. **a)** 7d untreated cube slice, **b)** 5ac cube slice, 108 hours at 700°C, **c)** 7b cube slice, 16 hours at 800°C.

H/D exchange in opx single crystals

Single crystal H/D exchange in mantle opxs of the peridotite xenolith have been controlled through the results of FTIR measurements performed at the center of annealed single opx crystals after each annealing step. A summary of the diffusion coefficients for H/D exchange obtained from the opx single crystals is presented in Table 6.2 together with the evolution of the integral absorptions for each single crystal with its crystallographic orientation. An example from opx5 (annealing at 800°C) is presented in Fig. 6.2a,b where the evolution of the representative FTIR spectra at the center of the single crystal is plotted together with the integrated area. For detailed graphs, all data from single crystals are presented in the Appendix D3. For the fit of the progressive H/D exchange and the determination of the diffusion coefficient in the direction perpendicular to the slice of the single crystals, we used the same approach as the one used in Blanchard and Ingrin (2004).

The thickness of the crystals slices is very small compared to their surface dimensions (length and width), that allows us to consider only diffusion in one direction, perpendicular to the surface. Diffusion can therefore be described by the equation for diffusion in an infinite plate with homogenous initial concentration (equation 2.6, chapter 2; Blanchard and Ingrin, 2004).

T (ºC)	700			800			800			900		
Opx# and orientation	Opx1 α			Opx5 γ			Opx2 γ			Opx3 α		
logD (m^2/s)±	**-13.70** $(^{-13.52}_{-14.00})$			**-12.40** $(^{-12.30}_{-12.52})$			**-12.30** $(^{-12.26}_{-12.35})$			**-12.19** $(^{-12.10}_{-12.30})$		
	t (h)	A_{OH}-A_{OD}	Σ_{HD}	t (h)	A_{OH}-A_{OD}	Σ_{HD}	t (h)	A_{OH}-A_{OD}	Σ_{HD}	t (h)	A_{OH}-A_{OD}	Σ_{HD}
	0	138.7 - 0	138.7	0	242.9-0	242.9	0	207.3-0	207.3	0	188.0-0	188.0
	1	123.4-8.2	133.5	8	69.4-70.2	233.7	5	69.6-63.0	207.3	1	98.8-24.8	186.1
	4	92.5-31.4	131.2	16	49.3-84.8	248.0				4	19.5-47.9	188.1
	12	60.7-58.1	132.3									
	36	47.0-72.9	136.8									
	108	19.6-94.4	135.9									

Table 6.2: Diffusion coefficients deduced from analyses in opx single crystals. The evolution of the integral absorption of OH (A_{OH}) and OD (A_{OD}) bands is also presented. Time is the total time after each steps. Σ_{HD} is the total absorbance $A_{OH} + b*A_{OD}$ as defined in the procedure to verify that no hydrogen species have left the crystal during the exchange (see text).

We collected all the spectra from the center of the single crystals after each time step and we used the following procedure in order to deduce the diffusion coefficients:

- First, we verified that we did not have any hydrogen species (D or H) loss during the exchange experiment. In order to do it we plot value of $A_{OH0} - A_{OHt}$ versus A_{ODt} where A_{OH0} is the integral absorption of the initial OH bands at t = 0, A_{OHt} the integral absorption of the OH bands after each step at time t and A_{ODt} the integral absorption of the OD bands after each step, at time t. If there is no loss during the exchange the two values must be linearly correlated (Fig. 6.2). The quantity of H exchanged is equal to the D exchanged; the diminution of A_{OH} must be equal to the increase of the A_{OD} modulo the ratio b of the two extinction coefficients of OH bands and OD bands. The slope of the linear plot gives the value of b (Fig. 6.2). We verify then that $A_{OH} + b*A_{OD}$, which is proportional to the concentration of all hydrous species remains constant all along the exchange (Fig. 6.2).

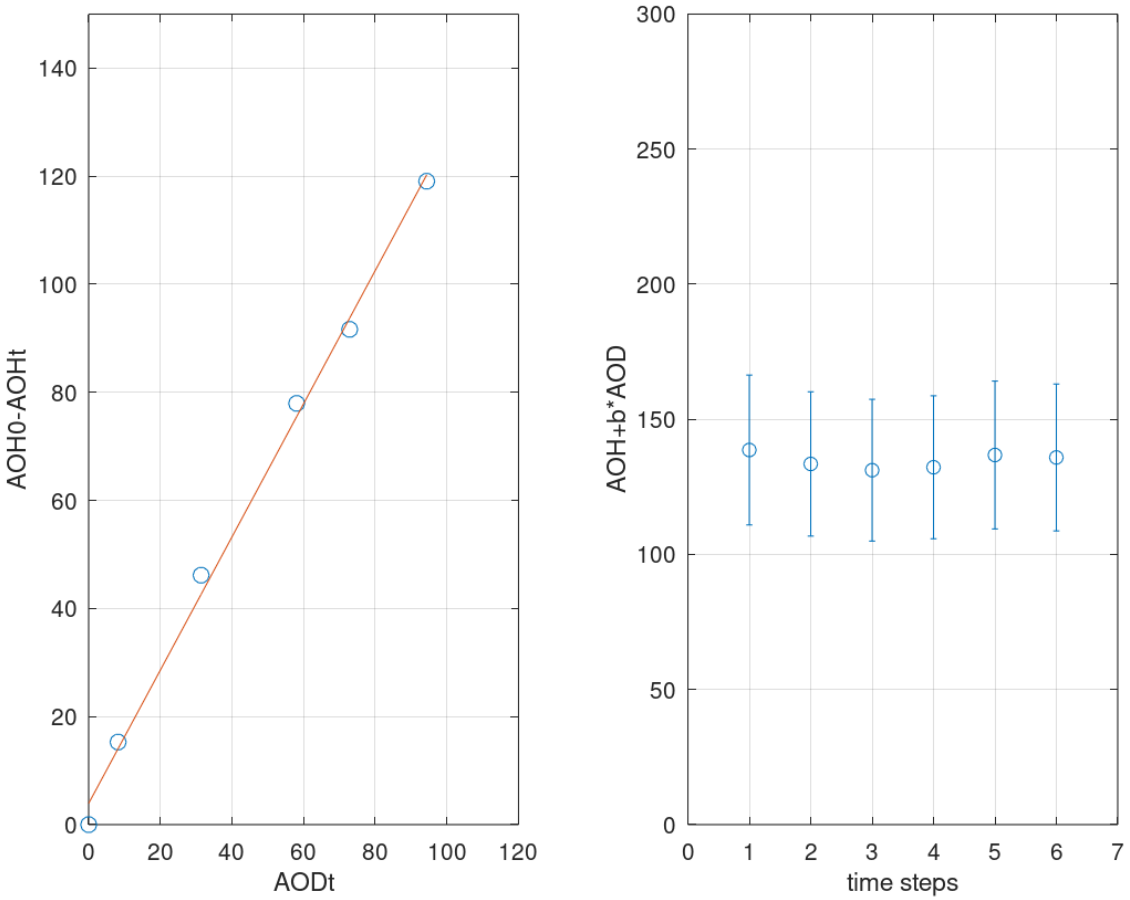

Figure 6.2: Plots derived from computing b value (left) and constant ratio with error bars of A_{OH} + b*A_{OD} for single crystal opx1 (right). Notice that for plot convenience, the initial value is labeled as step 1.

- Second, from the computed value of b, we calculate A_{ODs}, the maximum OD absorbance at saturation when all original H have been exchanged into D.
- Third, we compute A_{OHt} / A_{OH0} and 1- (A_{ODt} / A_{ODs}) versus time. These two values were finally plotted together and were fitted numerically by the solution of the equation 2.6 in order to find the best diffusion coefficient that fit the data (Fig. 6.3c). Therefore, the diffusion coefficient (logD) in Table 6.2 is the best fit of data (green fit in Fig. 6.3d) and uncertainties correspond to the min and max fits that still can be considered acceptable (Fig. 6.3d).

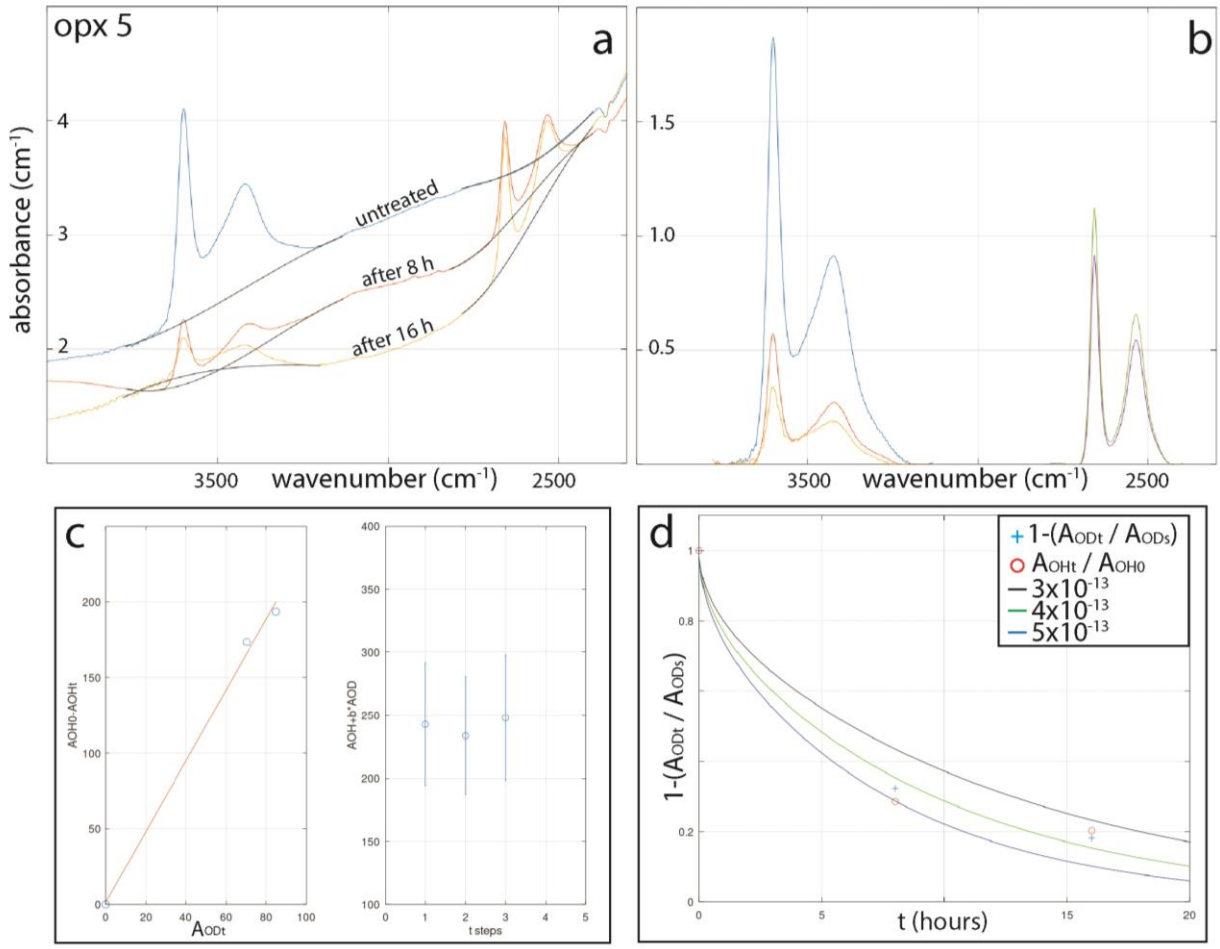

Figure 6.3: a) FTIR spectra of H/D exchange in opx5 single crystal, 16 hours at 800°C. **b)** Extraction of the baseline. **c)** Plots for calculation of b and A_{OH} + b*A_{OD} = constant, with error bars, showing that no hydrous species was lost during the time-steps for this experiment. **d)** Fit of H/D exchange and determination of diffusion coefficient.

H/D exchange in opx at cube's edge

Profiles were also measured in opx crystals from the cube slices, which were directly in contact with the gas on the edge of the cubes at the end of each experiment series. A summary of the diffusion coefficients for H/D exchange obtained from these opxs, is presented in Table 6.3. For detailed graphs, are presented in the Appendix D4. Fig. 6.4 shows a representative profile measured in an opx at the edge of the cube slice 5b. The fit of the diffusion profile in the opx crystal at the edge of the cube slice 5b is presented in the Fig 6.4. Fit was performed following the same approach as in Ingrin and Blanchard (2006) (equation 2.7, chapter 2).

T (°C)	600	600	700	900	900
Cube # and orientation	5b.4 α	5b.10 γ	5ac.3 α	6b2.3 α	6b2.4 α
S.logD (m^2/s)±	**-14.40** $(^{-14.30}_{-14.52})$	-14.22$(^{-14.10}_{-14.40})$	-14.45$(^{-14.22}_{-15.00})$	-12.22$(^{-12.10}_{-12.40})$	-12.30$(^{-12.22}_{-12.40})$
I.logD (m^2/s)±	A_{ODx}=0	**-14.05**$(^{-14.00}_{-14.10})$	**-14.00**$(^{-13.70}_{-14.05})$	**-12.15**$(^{-12.10}_{-12.22})$	**-12.15**$(^{-12.10}_{-12.22})$
Contrib. (m^2/s)±	-	α or β 2-5x10^{-12}	γ or β 5-7x10^{-14}	β or γ 2-6x10^{-12}	β or γ 2-6x10^{-12}
Lateral diffusion range (μm)	-	120-170	60-100	170-310	250-420

Table 6.3: Diffusion coefficients deduced from analyses in opx crystals at the edge of cube slices.

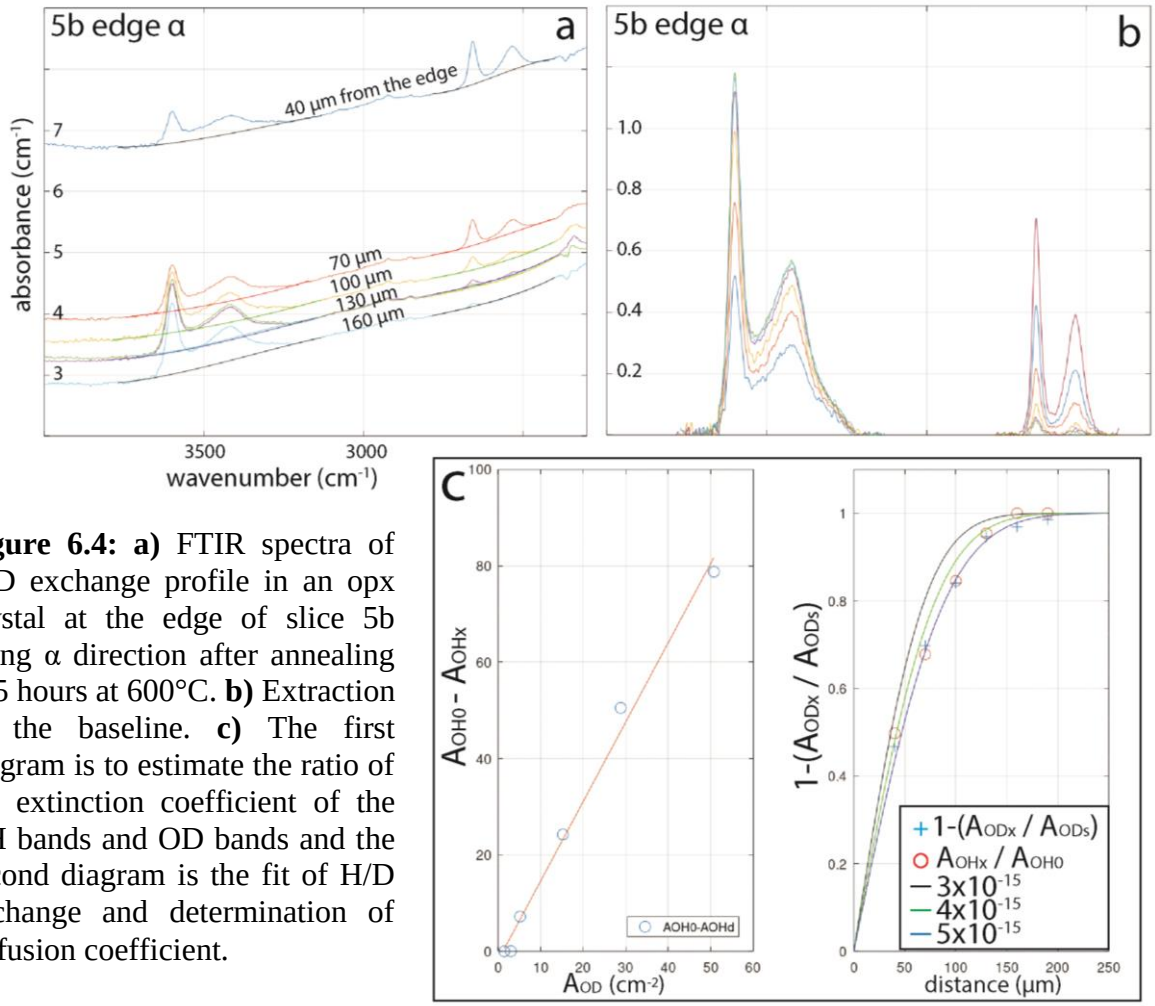

Figure 6.4: a) FTIR spectra of H/D exchange profile in an opx crystal at the edge of slice 5b along α direction after annealing 135 hours at 600°C. **b)** Extraction of the baseline. **c)** The first diagram is to estimate the ratio of the extinction coefficient of the OH bands and OD bands and the second diagram is the fit of H/D exchange and determination of diffusion coefficient.

The diffusion coefficients deduced from measurements of profiles presented in Table 6.3 have been processed differently from the single crystals. Although, the same calculations performed here as well, but instead of the A_{OHt} we now have A_{OHx} as the variable is not any more time but distance, two different cases have been identifying. First, when A_{OD} at the end of the

profile towards the center of the crystal is equal to zero, there is obviously no contribution of lateral diffusion and the profile can be treated simply as the result of a 1D diffusion (equation 1.3, chapter 2). This corresponds to the values labeled S.logD in the Table 6.3. Second, when 1-(A_{ODx} / A_{ODs}) values create a flat plateau, below value 1 it means that a contribution from lateral diffusion was present and a 2D analysis is necessary.

For the second case profiles, we first try to estimate logD by doing a rough assumption that the effect of the lateral diffusion produced a simple shift in the values by adding a constant amount of H/D exchange in the profile (see Fig. 6.9b left). One approximate way we treat these cases is to simply subtract the value of A_{ODx} from the end of the profile (inside the cube) from all the profile values, recalculate A_{OH} , A_{OD} and then follow the same approach as in the first case. This is of course an oversimplification with a very crude approximation but we also listed these values as S.logD in the tables for comparison with the corrected I.logD that were derived from a 2D modelling. All these S.logD for profiles from the edge of the cube slices are slower than the corrected I.logD.

The need for understanding the effect of lateral diffusion contribution leads us to the 2D modelling with Idefick. The profiles that were evaluated with the Idefick software and values obtained from this procedure are labeled as I.logD in the tables.

Numerical modelling for the profiles in opxs at cube's edges

The procedure followed for the modelling of the impact of the lateral diffusion with Idefick is described below.

For the simulation of the profile, we arbitrarily decided that they are measured along the y axis of the simulation and the contribution from the lateral diffusion come from the x axis (Fig. 6.5). It could have been the opposite but it does not change the results for this particular simulation, as the grain boundary diffusion was set very high and as a very large layer (70μm) to simulate an almost instantaneous diffusion at the edge of the cube. The lateral diffusion can come from a side of the crystal that can be identified in the plan of the slice or a side that was in the direction perpendicular to the cube slice and that has been removed from the cutting.

We set the deuterium infinite gas at x: 0-20μm y: 0-1000 μm and fixed concentration at zero, to act as a "sink" for the hydrogen diffusion (hydrogen concertation for this reservoir is equal to zero, Fig. 6.5). We define a grain boundary along x direction with size 70μm at x:430-500μm

and the rest of the area represent two separated opx crystals. Crystals and grain boundary concentration is set to 1 as a state of equilibrium. We need to emphasize that the grain boundary in this numerical modelling experiments is considered like a layer with extremely fast diffusion coefficient (logD = -9) and not as an actual grain boundary. We used very high diffusion rate in this layer to estimate the contribution of lateral diffusion because we assume that there is no significant difference due to grain boundary for the lateral diffusion contribution. This is an acceptable approximation for the lateral diffusion in the opx crystals at the edge of the slice, but also for the profiles in opx inside the cube (see next paragraph). Indeed, in both cases, in a first approximation, the impact the difference of length of the grain boundary path to reach the sides of crystal involved in the two directions diffusions can be considered negligible. The first tests were with diffusion values for Dx and Dy based on the single crystals and depending of the orientation. These two were the only parameters changed for this part of the modelling. We fit the experimental profile with the best modelling profile (Fig. 6.6) and we deduced the possible distance of the 'edge' of the crystal in the x direction (Table 6.3) from the lateral (or perpendicular) side of the crystal. The range of distance is depending on the range of the diffusion value in Dx, faster diffusion shorter distance and vice versa. Photos of the crystals and their orientation were used in the end to identified possible origin of lateral diffusion (all profiles were treated like this and presented in Appendix D4).

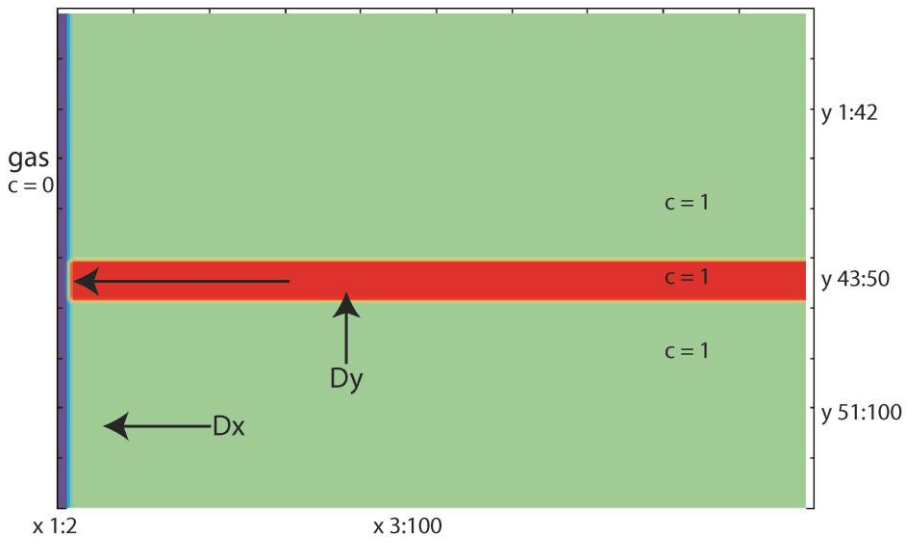

Figure 6.5: Initial parameters for the numerical simulations. The arrows indicate the direction of the hydrogen flux. Concentration 1 refers to an equilibrate state of hydrogen in the crystal while in the deuterium gas is 0.

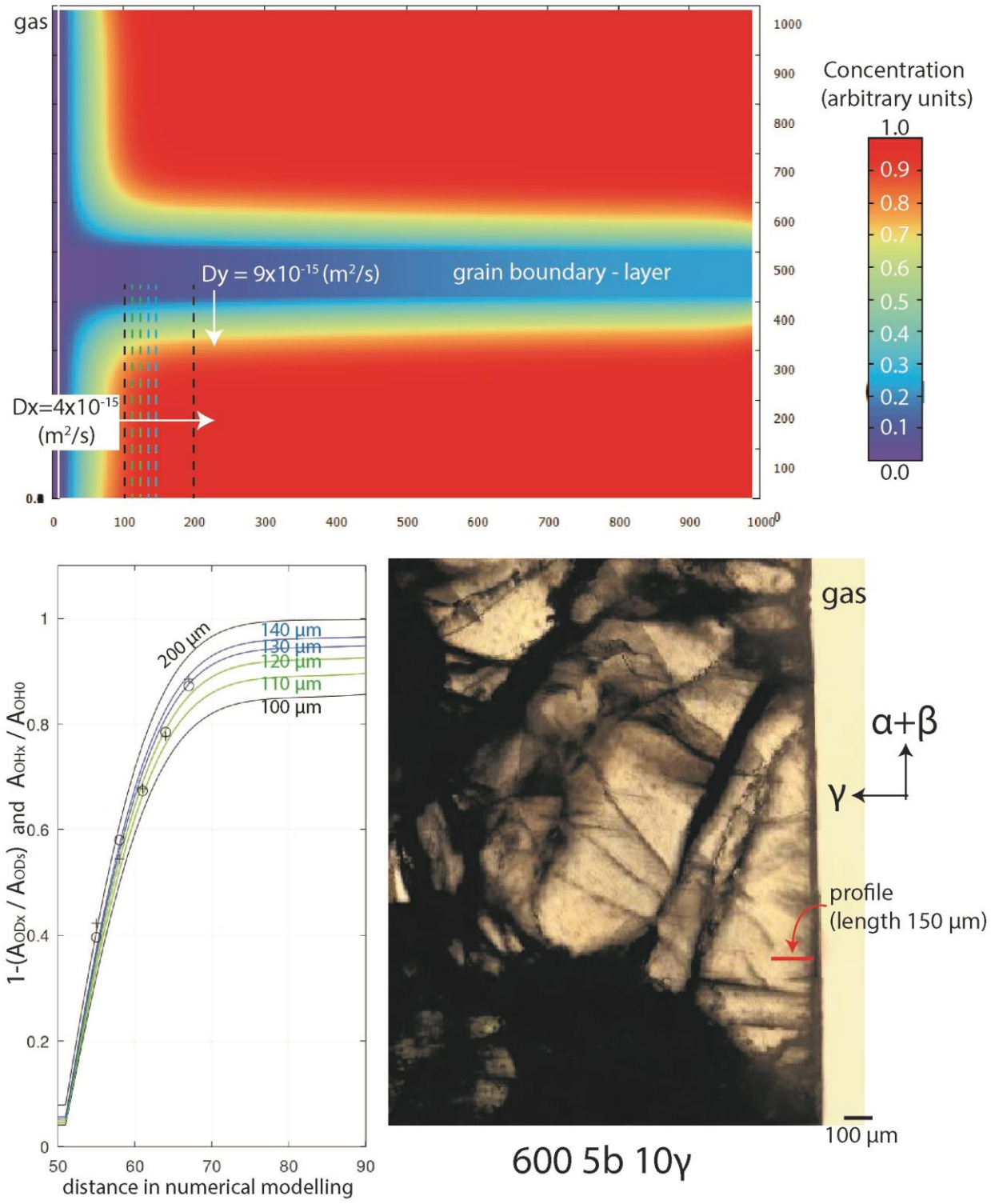

Figure 6.6: One example of the 2D Idefick modelling showing the final results of a numerical experiment and how it is connected with our experimental results. The Dx shows the diffusion on x axis while Dy represents the direction of our measured profile in opx crystal from the edge of the cube.

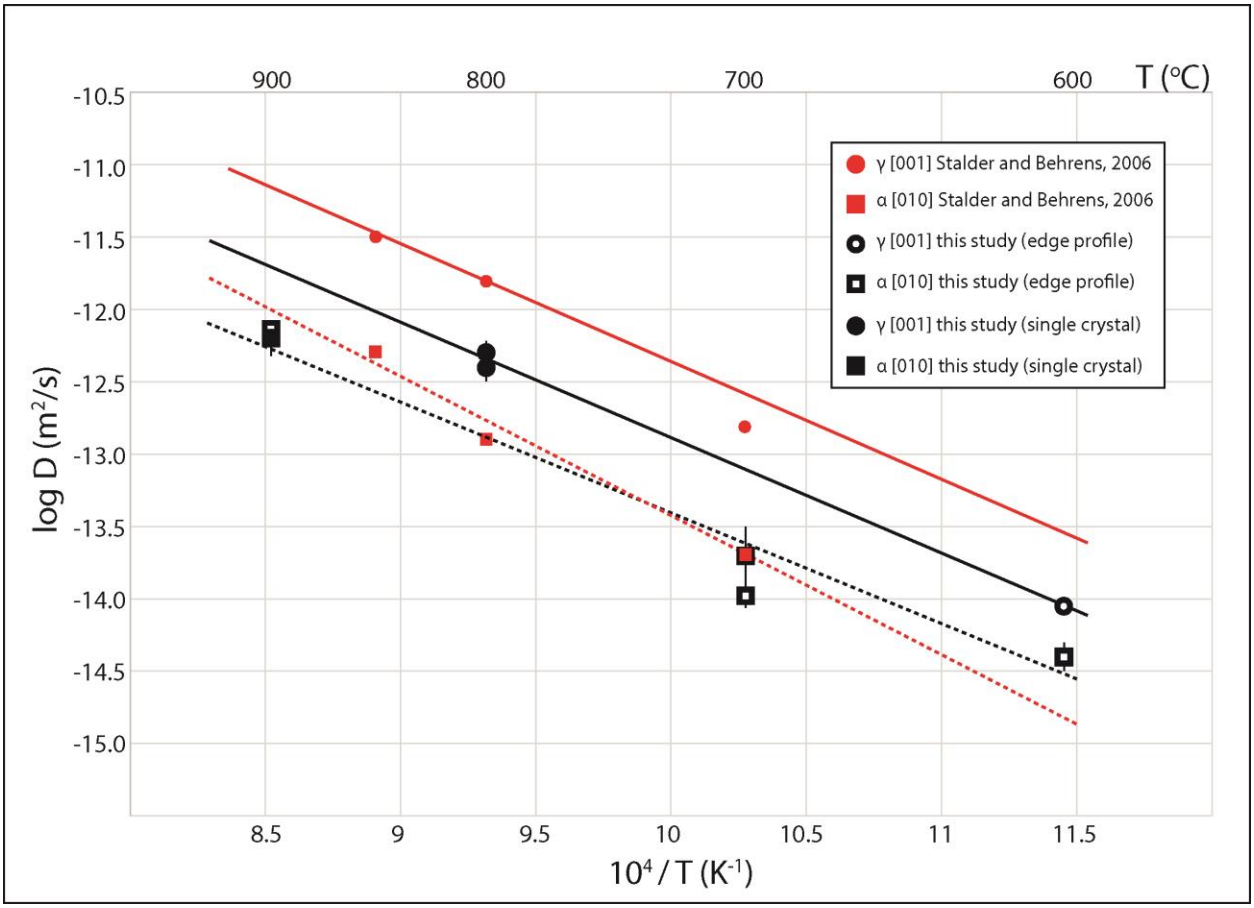

Figure 6.7: Arrhenius plot showing H/D intra-crystalline diffusion coefficients deduced from the measurements in opx single crystals and at the edge of the cubes, compared to results from the previous study in pure synthetic enstatite of Stalder and Behrens (2006). All error bars are indicated when larger than the size of the symbols.

Results from the single crystals and the profiles at the cube's edges are comparable to the values proposed by Stalder and Berhens (2006) for synthetic enstatite (Fig. 6.7). We confirm the anisotropy of diffusion observed before with γ direction faster than the α direction. We extend the domain of temperature of validity of the previous data by 50°C above and 100°C below. 'Self-diffusion' of hydrogen (H/D exchange) is slightly slower in mantle opx than in pure enstatite and activation energy are comparable (152.4 versus 158 kJ/mol for γ and 157.8 versus 185 kJ/mol for α):

$$D_{\gamma}^{H} = D_0 \exp\left(\frac{-152.4 \pm 7{,}8\ kJmol^{-1}}{RT}\right), \text{ with } D_0 = -1.2\ (\pm 2.6)\ x10^{-5} \qquad (6.1)$$

$$D_{a}^{H} = D_0 \exp\left(\frac{-157.8 \pm 14.5\ kJmol^{-1}}{RT}\right), \text{ with } D_0 = -6.5\ (\pm 5.4)\ x10^{-6} \qquad (6.2)$$

These results and the diffusion laws deduced for the intra-crystalline 'self-diffusion' will be used as reference for comparison with profiles measured in opx inside the cubes.

H/D exchange in opxs inside the cube

The same approach than the one used for opx at the edge of the cubes was used to analyze the diffusion profiles inside the cubes. Results are presented in Table 6.4. We reported in this table the shortest length of the straight path from the edge of the crystal to the beginning of a profile measurement (bird's-eye distance). We also reported grain boundary paths that were calculated from 2D images, but these values are an overestimation because we have only a 2D representation of the grains' interface and it represents only a maximum path length. We reported both values in Table 6.3, but we decided to utilize the first value in the rest of the study to be most conservative as possible (Fig. 6.8).

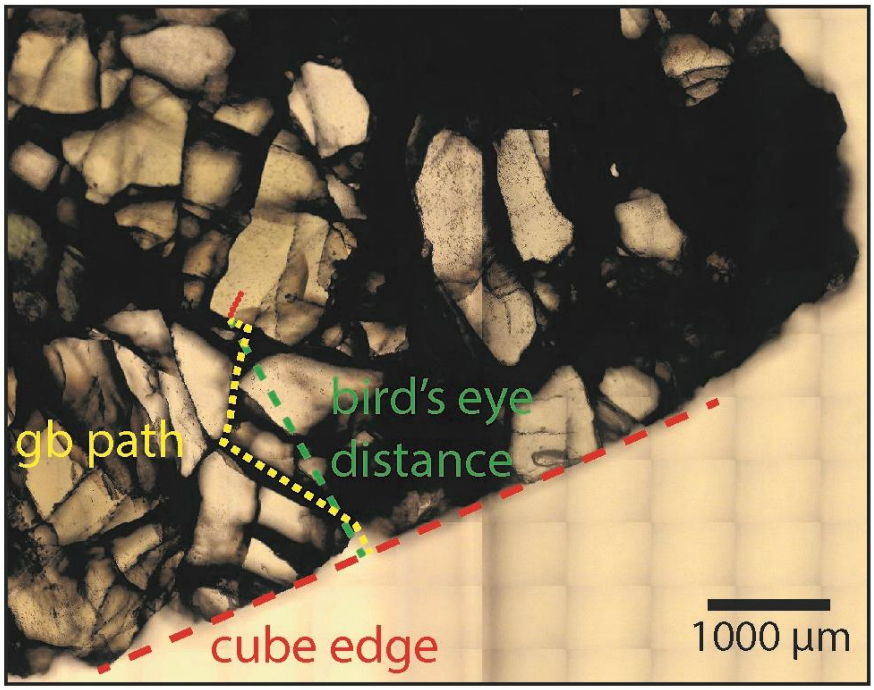

Figure 6.8: Example of the two types of distances from the edge: bird's eye distance with green color and 2D grain boundary path with yellow. Red dots in the crystal represent the profile measurement.

In case (a) after check of the absence of any deuterium in the center of the crystal, 1D profiles were fitted by equation 1.5 (chapter 2) and diffusion coefficient deduced from the fit with uncertainties. An example is presented in Fig. 6.9a. In case (b) We first performed the same approximation as mentioned before. Example is shown in Fig. 6.9b left, the original position, black symbols become the red symbols. Results of this approximation are reported as S.logDa in Table

6.4. The corrected complete fit of the original profile using the modelling by the 2D Idefick software is shown in the plot on the right side of Fig. 6.9b and results are reported as I.logDa in Table 6.4.

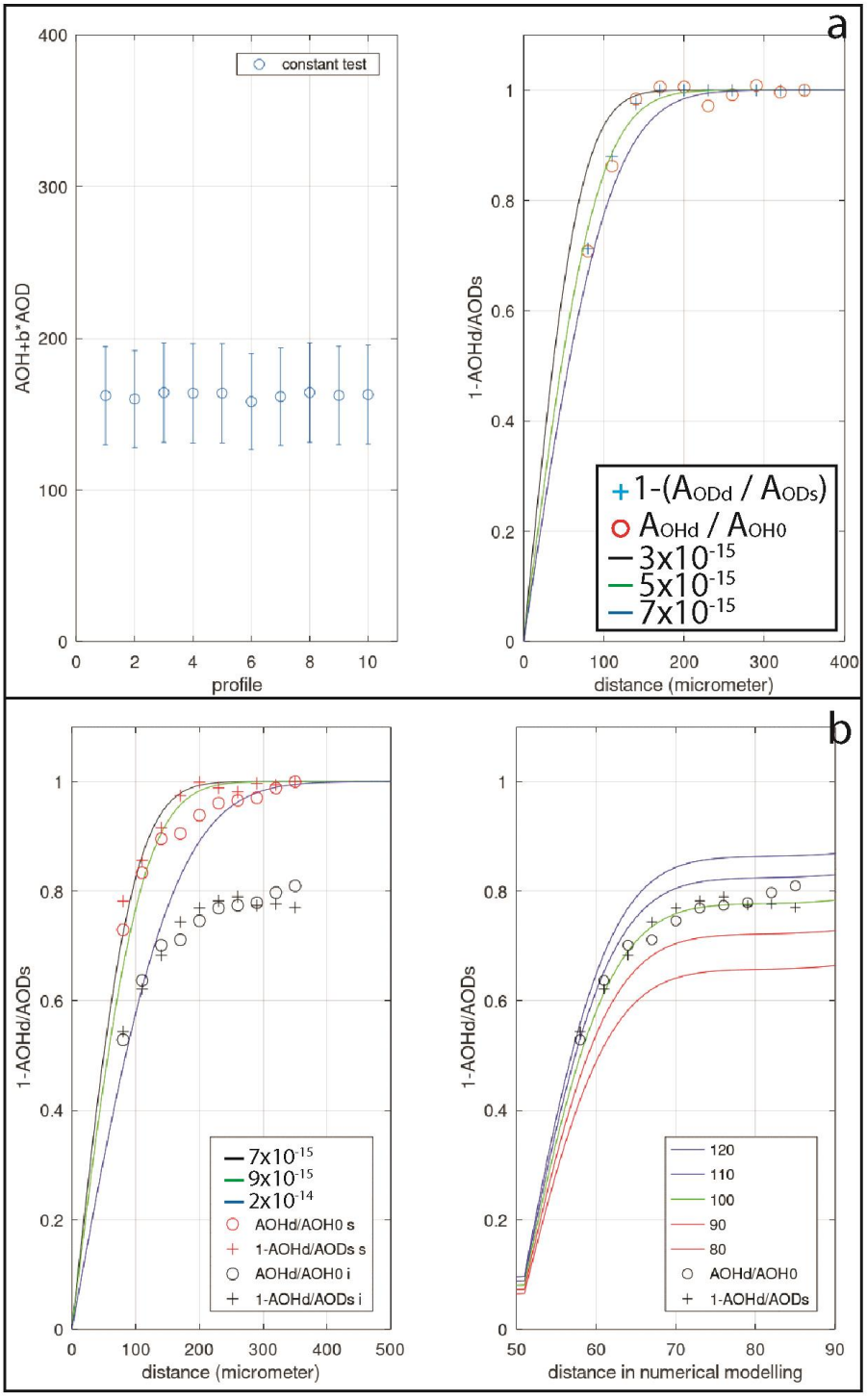

Figure 6.9: a) Fit of profile from inside the cube 5b 600°C γ [001]. On the left is the test we perform to verify that we do not have any hydrogen loss during the experiments. b) On left, fit of profile from inside the cube 5aii.0 700oC γ [001] after simplification (red symbols) and on right after Idefick processing. For more information, see text.

Temperature (ºC)	600	600	600	600	700	700
# and orientation	5b.2 α	5b.8 γ	5bb.2 γ	5bb.6 α	5ac.5 γ	5aii.0 γ
Distance from edge (mm)	0.7 (0.7)	1.7 (2.0)	1.3 (1.4)	1.0 (1.1)	0.5 (0.5)	2.3 (2.7)
S. logDa (m^2/s)±	-15.05 ($^{-15.00}_{-15.10}$)	**-14.52** ($^{-14.40}_{-14.70}$)	**-14.30** ($^{-14.15}_{-14.52}$)	**-14.70** ($^{-14.52}_{-15.00}$)	-14.15 ($^{-14.05}_{-14.30}$)	-14.05 ($^{-13.70}_{-14.15}$)
I. logDa (m^2/s)±	**-15.05** ($^{-15.00}_{-15.10}$)	A_{ODx}=0	A_{ODx}=0	A_{ODx}=0	**-13.52** ($^{-13.40}_{-13.70}$)	**-14.05** ($^{-14.00}_{-14.10}$)
gb Dif. (m^2/s)±	1-3x10^{-12}	-	-	-	3-8x10^{-12}	3-8 x10^{-12}
Contribut. (m^2/s)±	γ 2.5-4 x10^{-15}	-	-	-	β 7-9 x10^{-15}	α or β 6-8x10^{-15}
Lateral diffusion range (μm)	80-110	-	-	-	50-70	90-110

Temperature (ºC)	800	800	800	800	900	900
# and orientation	7b.1 γ	7b.5 γ	7b2.3 γ	7b2.7 γ	6b2.9 α	6c.7 γ
Distance from edge (mm)	0.5 (0.5)	2.8 (3.0)	1.6 (1.7)	2.2 (2.4)	3.0 (3.3)	2.4 (3.0)
S. logDa (m^2/s)±	-13.22 ($^{-13.05}_{-13.52}$)	-13.26 ($^{-13.05}_{-13.70}$)	-13.34 ($^{-13.22}_{-14.00}$)	-13.18 ($^{-12.82}_{-13.52}$)	-12.30 ($^{-12.10}_{-12.70}$)	-12.02 ($^{-11.82}_{-12.10}$)
I. logDa (m^2/s)±	**-12.35** ($^{-12.30}_{-12.40}$)	**-12.52** ($^{-12.40}_{-12.70}$)	**-12.40** ($^{-12.30}_{-12.52}$)	**-12.52** ($^{-12.40}_{-12.70}$)	**-12.22** ($^{-12.15}_{-12.30}$)	**-12.05** ($^{-12.00}_{-12.10}$)
gb Dif. (m^2/s)±	8x10^{-12} – 1 x10^{-11}	8 x10^{-12}	3 x10^{-11}	3 x10^{-11}	3 x10^{-10}	3 x10^{-10}
Contribut. (m^2/s)±	α + β 2-3 x10^{-13}	α + β 9 x10^{-14}-1 x10^{-13}	α or β 2-3x10^{-13}	β 2-3 x10^{-13}	γ 9 x10^{-13}-1 x10^{-12}	a or β 7 x10^{-13}
Lateral diffusion range (μm)	70-100	80-100	100-170	110-180	110-150	150-190

Table 6.4: Apparent diffusion coefficients (D_a) deduced from analyses in opx crystals inside the cube slices. S. is for the simplification mode and I. is for the result of Idefick modelling (see text for details). Both values are presented for comparison. Distance from edge in brackets is the evaluated 2D grain boundary path.

In Figure 6.10, we plotted the apparent diffusion coefficients (D_a) of profiles with the same orientation versus their distance from the edge of the cube (S.logDa for cases (a) and I.LogDa for cases (b)). We can see that the diffusion coefficients are systematically lower from data inside the cubes. Only slightly lower at the higher temperatures (800 - 900°C), more significantly lower for experiments performed at 600°C and 700°C. At 900ºC, the value for α [010] is similar within error and the value along γ [001] is 0.35 log unit below the one predicted from the intracrystalline diffusion law. At 800°C, only profiles along γ [001] could be measured, the two data closer to the edge give values similar to the ones predicted by the intracrystalline diffusion law (log D = -12.35 and -12.40) while the two further away give values slightly lower (log D = -12.52 in the two cases). The later values remain within the error bars, but the apparent trend go in the right direction. At 700°C and 600°C the differences are more important with values clearly out of the error bars: -0.3 to -0.8 log unit at 700°C along γ, -0.3 to -0.65 log unit at 600°C along α and -0.25 to -0.45 log unit at 600°C along γ. Except for the two profiles at 600°C along α, the general tendency is a decrease of the apparent diffusion coefficient with the increase of the distance from the edge of the cube. We also represented the average difference of diffusion coefficients in function of temperature (Fig. 6.11). This is a semi-quantitative representation, because it neglects the role of the position of the crystals inside the cube, but it gives a general figure of the evolution of the diffusion differences with temperature and orientation. The figure confirms what we have noticed before the difference seems to increase when temperature decrease. Fig 6.11 also highlight that the difference between apparent diffusion coefficients is higher for the fast direction γ than for the slowest α.

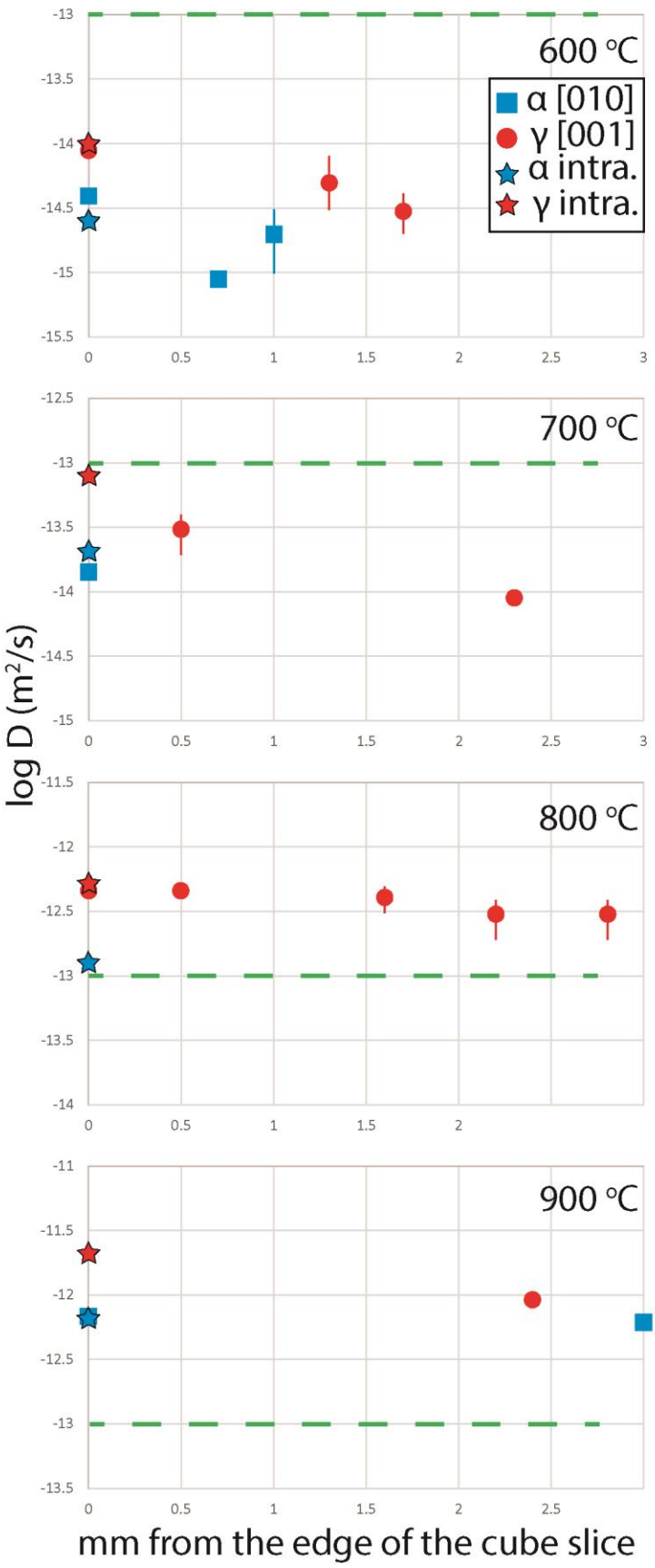

Figure 6.10: H/D diffusion coefficients versus the bird's eye distance to the edge of the cube slice. Stars are value of intra-crystalline diffusion coefficient along γ [001] and α [010] calculated from the diffusion laws. Green line indicates $D=1x10^{-13}$ m^2/s for visual comparison between the different temperatures. All error bars are indicated when larger than the size of the symbols.

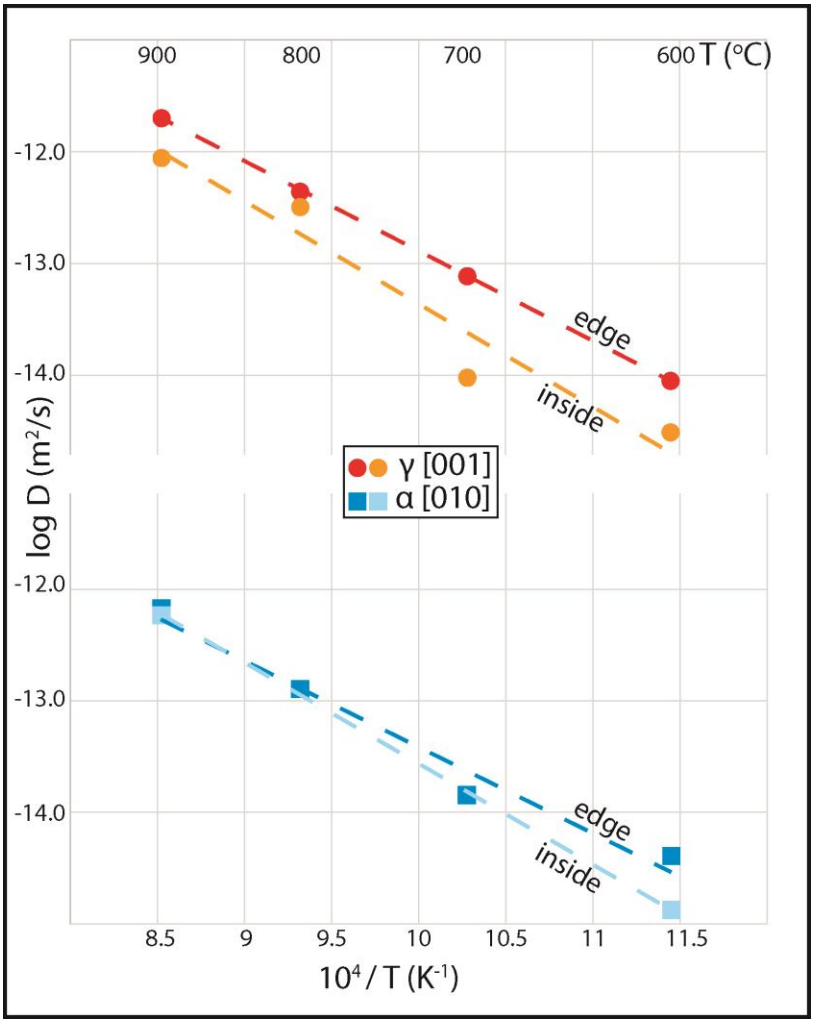

Figure 6.11: Comparison of apparent diffusion coefficients for opx at the edge and inside the cube, for the two orientations versus temperature. The value plotted for α at 600°C inside is the average. For γ we choose profiles between 1.6-2.4 mm from the edge of the cube slice to lower any bias from the various distances.

6.2 Discussion

In our H/D diffusion experiments, only H and D isotopes were exchanged, there was no loss or gain of hydrous species during the whole process. The decrease of the integral absorbance of OH bands with time (single crystals) or with distance from the edge of the crystals (profiles in cubes) are totally compensated by the increase of the integral absorbance of the OD bands.

Interpretation of results for single crystals diffusion and profiles from the edge of the cubes

From our results, from the single crystals and the profiles in the edge of the cube's slice we propose two diffusion laws for α and γ orientation (equation 6.1, 6.2) that are slightly different compared

to Stalder and Behrens (2006). These diffusion laws can be directly used for mantle opx. We estimate that our small differences in the importance of anisotropy can be related from the uncertainty of our method to identify the orientation of the grains. We used the lattice overtones (1250–2350 cm^{-1}), the uncertainty of the method is higher than the optical method used by Stalder and Behrens (2006) for their well crystallized synthetic samples. A small contribution of the [010] direction, the intermediate diffusion rate in opx, can be present in some of our analyses. Otherwise, we are confident in our activation energy that are comparable for the two directions and are obtained from a larger temperature range.

Bulk diffusion inside the cubes and numerical modelling

The main result of our analyses is that we see a slight effect of the transport of deuterium through grain boundaries on the diffusion in the opxs inside the cubes. The apparent H/D exchange in the single grains is slightly slower inside the cubes than at their edges. The effect is larger further inside the cubes than closer to their edges and larger for the fast intra-crystalline diffusion along γ than in the slower along α. These characteristics are in line with the impact of the deuterium diffusion through grain boundaries, limiting deuterium availability to the grains. Faster the intracrystalline diffusion inside the opx, stronger the effect of rarefaction of deuterium available in the grain boundary for the exchange, explaining the larger effect on the γ direction compared to the α direction.

The apparent limited effect of grain boundaries at the higher temperatures is probably because in the experiments at lower temperatures, due to the slower intracrystalline diffusion rate, the H/D exchange was less pronounced than at higher temperatures. Diffusion profiles were shorter, as evidenced by the larger number of cases (α) without contribution from lateral diffusion (see also profiles reported in Appendix D4). Impact of grain boundary is probably more easily visible at the beginning of the intracrystalline diffusion inside the cube (closer to the diffusion regime C, see later discussion).

Nevertheless, the effect is very limited, it is especially interesting result for the higher temperatures of experiments, which are closer to the temperature of magma that transport xenoliths to the surface. The hydrogen isotopic transport in grain boundaries is fast enough to equilibrate rapidly the isotope signature of the opx grains inside the xenolith with the surrounding magma.

Most of basaltic magma have temperature above 900°C. Our results suggest, that even at 900°C the hydrogen isotopic signature of opxs is strongly modified in few hours even at a bird's-eye distance from the edge of the xenolith of 3 mm. Even without sophisticated numerical modelling, it is clear that the main hydrogen isotopic signature of mantle xenoliths corresponds to late equilibrium with the magma. This is surely true for any peridotite xenolith with homogeneous hydrogen isotopic signatures. In most cases it would be rather impossible for opxs within less than one centimeter of the edge of the xenolith to remain unaffected. This will be true also for olivine and cpx which have respectively, comparable and slightly faster intracrystalline H isotope diffusion coefficients (see for instance, Farver, 2010; Du Frane and Tyburczy, 2012; Tian et al., 2017). The transport through the grain boundaries is not a strong limitation to the isotopic exchange with the magma.

Grain boundary diffusion in the xenoliths and numerical modelling

Can we go further and propose quantitative values for grain boundaries diffusion of hydrogen in mantle xenoliths from our data? These data are the results the flux of H/D through the grain boundaries and they are not only a function of the grain boundary diffusion coefficient (D_{gb}), but also are a function of the amount of H/D present in the grain boundary (gb). Roughly, it is a function of the product $\delta.s$, δ being the width of the grain boundary and s the segregation coefficient, term which is proportional to the partition coefficient of H/D between the gb and the crystal. The question is complex, because despite some values of s have been proposed for olivine-olivine interfaces (Fei et al., 2006; Gardner et al., 2020), we ignore the values of both D_{gb} and $\delta.s$ and these values may vary with the nature of the interfaces (ol-ol, ol-opx, opx-opx, ol-cpx etc…).

In the present stage of our knowledge, it is acceptable to consider an average behavior, assuming a common behavior for all interfaces. With this assumption, we can easily estimate a lower limit for D_{gb}.

Our diffusion experiments are conducted in what is called the regime B defined by Harrison (1961) (see Fig. 6.12). In regime B, the diffusion within the grains size is significantly smaller than the grains (here we observe profiles in opx grains), or the diffusivity in the crystal is significantly slower than in the grain boundary (it is what we observed in our experiments).

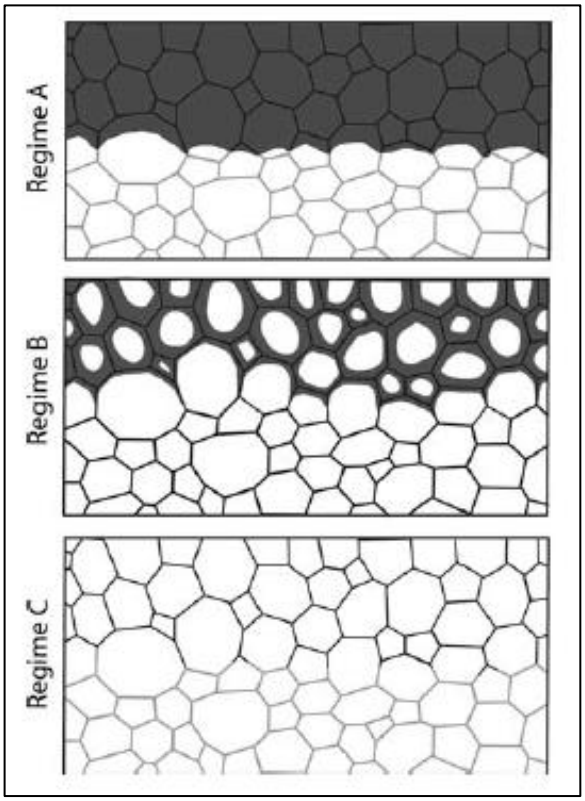

Figure 6.12: Regimes of diffusion in polycrystals with stationary grain boundaries. The diffusion species is diffusing from the surface at the top of each box. Figure reproduced from Demouchy 2010 modified from Balluffi et al. 2005.

In the experiments, we measured the intra-crystalline profiles in opx at different depths within the cubes (Regime B). Therefore, if a profile is observed it means that the grain boundary surrounding the grain has been saturated in deuterium through gb diffusion in a time smaller than the complete experimental time. It means that we can have a first estimation of a lower limit of D_{gb} by using the simple expression:

$$d = sqrt(D_{gb}t)$$

where d is the bird's-eye distance of the opx from the surface and t is the time of the experiment. This is of course a rough estimation because in Regime B the grain boundary surrounding the opx where has been measured the profile have been filled in with deuterium much earlier. It is why we observed an intracrystalline diffusion profile. Furthermore, part of the deuterium may diffuse to the side crystals along the gb path during its migration toward the opx grain. This decreases the efficiency of the transport increasing the range of the underestimation of D_{gb}. Fortunately, a majority of the side grains on the path may be olivine grains that have low hydrogen content, limiting the bias effect of lateral diffusion of hydrogen.

This rough estimation of the lower limit of D_{gb} provides already interesting values: $8x10^{-10}$ m^2/s at 900°C for the profile 6c.7γ (d = 2.4 mm), $1.4x10^{-10}$ m^2/s at 800°C for the profile 7b.5γ (d=2.8 mm) or $1.4x10^{-11}$ m^2/s at 700°C for the profile 5aii.0γ (d = 2.3 mm). These values of the diffusion coefficients are already 2.3 to 2.6 log units higher than the diffusion coefficients of the intracrystaline diffusion along the fast direction γ (equation 6.1, Figure 6.13).

But we can even be more restrictive in the estimation of the lower limit of D_{gb} by looking at the diffusion profiles that show significant difference with the diffusion profiles expected if the opx was directly in contact with the gas (at the edge of the cube). Let see for instance, the case of the profile 6c.7 along γ, which require a gb diffusion path d of 2.4 mm. If we assume that the deuterium flow in the gb is not a limiting issue (they can transport as enough deuterium as needed), only time of transport controlled by D_{gb} is the limiting factor, the difference is mostly due to a time delay for the deuterium to arrive close to the grain. We can estimate a corrected time t_c of intracrystalline H/D exchange t_c from the difference between the apparent diffusion coefficient D_a and the intracrystalline coefficient D and the experiment time t through:

$$sqrt(Dt_c) = sqrt(D_at)$$

or

$$t_c = D_at/D$$

The apparent delay in this case (t-tc) corresponds to the maximum time for the deuterium to reach the opx grain at the distance d. The minimum grain boundary diffusion can again be estimate through the equation:

$$d = sqrt(D_{gb}(t-t_c))$$

or

$$D_{gb} = d^2/(t- D_at/D) = d^2/t(1- D_a/D)$$

If we come back to the case of the profile 6c.7 at 900°C, we should have:

$$D_{gb} \geq (2.4x10^{-3})^2/[2x3600(1 - 10^{-12.05}/10^{-11.70})]$$

$$D_{gb} \geq 1.49x10^{-9}\ m^2/s$$

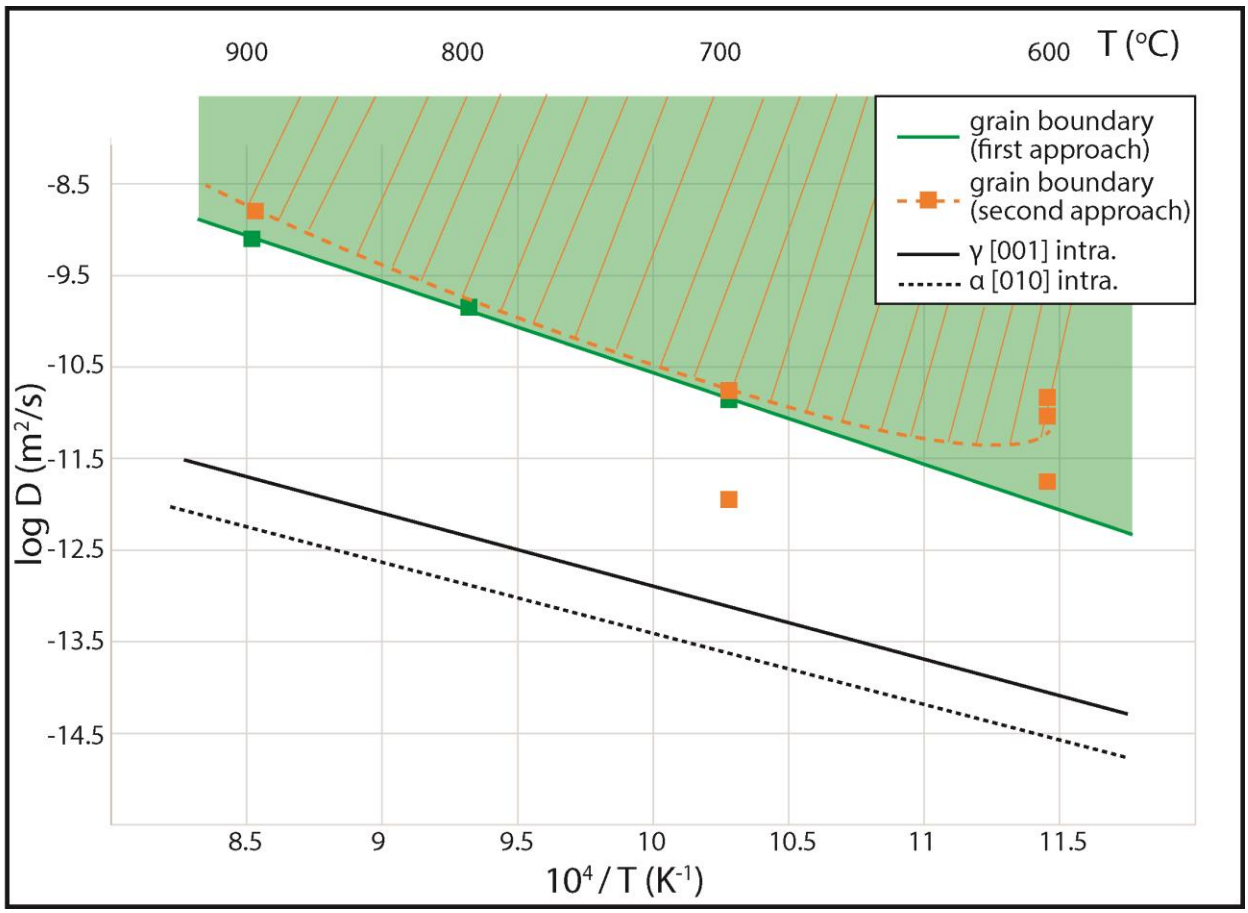

Figure 6.13: Comparison between H/D diffusion laws for intracrystalline diffusion and estimated lower limits of grain boundary diffusion with our two approaches.

We can use this approach to estimate at best the minimum value of D_{gb} in all the cases where a significative difference is obsreved between D_a and D. It means for any difference larger than the largest error bar (differences higher than 0.3 in log units). Below this values the approach is not valid because the estimation of the time delay become too close to zero. For instance, this approach cannot be used for the data at 800°C and the data in the direction α at 900°C (Table 6.5; Fig. 6.13).

Profiles	d (µm)	Dgb	logDgb
600 5b.2 α	0.7	1.62×10^{-12}	-11.79
600 5b.8 γ	1.7	8.98×10^{-12}	-11.05
600 5bb.6 α	1	1.34×10^{-11}	-10.87
700 5ac.5 γ	0.5	1.05×10^{-12}	-11.98
700 5aii.0 γ	2.3	1.54×10^{-11}	-10.81
900 6c.7 γ	2.4	1.49×10^{-09}	-8.83

Table 6.5: Calculation of lower limits of diffusion coefficients for grain boundaries from the selected profiles.

The advantage of these minimum estimations is that they do not need to do any assumption on the value of δ.s. The prediction is based on an estimation of the maximum diffusion time for the gb around the opx grain to be deuterated whatever the value of the hydrogen concentration in the gb.

The only limitation of this approach is linked to the presence of cracks inside some of the crystals of the xenoliths. We did not observe the formation of new cracks during the experiments but some cracks were initially present in the xenolith (see Fig. 6.1a). Some of them may be acting as shortcuts of diffusion, within the crystals of the cubes of xenolith. It is difficult to estimate their real contribution to the diffusion process. What is sure is that they do not form a continuous network, otherwise the cubes and the slices would have completely broken in small pieces. It means that even if some cracks are active as diffusion path at some stage of the migration of H/D, diffusion along grain boundaries needs to be active and take over the transport of hydrogen into the cube. We do not think that it will change significantly the conclusions above. The estimation was sufficiently conservative to allow even overestimation of the grain boundary path by a factor of two.

Assuming the effect of cracks is limited, if we want to go further, in the estimation of D_{gb} we must simulate numerically the effect of a credible range of values of δ.s on the observed diffusion profiles in an opx grain at distance d from the edge of the cube. We started to explore this approach in the § below. The approach is still at an early stage and what is presented shortly below is an exploratory work, not an achieved one. Nevertheless, we think that the approach deserves to be presented, because even incomplete and still in development, it offers an interesting perspective.

Toward the modelling of the contribution of gb to the observed diffusion profiles

In order to explore further the diffusion along grain boundary and to fit experimental data at 700°C we perform a series of numerical modelling experiments (Fig. 6.14). In these numerical experiments, we set intracrystalline diffusion rates for α ($Dx = 2x10^{-14}$ m^2/s) and γ ($Dy = 8x10^{-14}$ m^2/s) based on the diffusion laws and grain boundary diffusion D_{gb} at $8x10^{-11}$ m^2/s. What was changing in the tests was the thickness of the grain boundary area (20, 40, 80 μm). Of course, these are not real gb thicknesses, which are of the order of 1nm, but it allow to explore the impact of s

without changing in our experiments the concentration at the grain boundary. In these three experiments we changed δ.s by a factor of 1, 2, 4 respectively. What we can see is that while the grain boundary size is increasing, D_a deduced from the profiles at d = 400μm are shifting for 20 μm from values slightly slower than the intracrystalline diffusion (7-7.5x10^{-14} m^2/s) to the intracrystalline diffusion value Dy = 8x10^{-14} m^2/s when grain boundary is 80μm. We see also for instance, that D_a deduced from the profiles at a distance comparable to the condition of our experiments, d = 1800μm is shifting from values of 2x10^{-14}, 4x10^{-14}, 6x10^{-14} m^2/s when grain boundaries thickness pass from 20, 40 and 80 μm respectively. 2x10^{-14} m^2/s is not far from the value of apparent diffusion coefficient we observed at 700°C in experiment 5aii.0 at 2.3 mm from the edge of the cube.

Of course, the values of δ.s by in these numerical experiments are not the same as the ones in reality: δ.s in the numerical experiment with a 20 μm large gb with a concentration of 1is of the order of 20000 nm, while for a 1nm gb and a partition coefficient of 500 (Fei et al. 2006), δ.s = 500 nm. A re-scaling is needed, it would suggest that to have the same effect with a 1 nm grain boundary; D_{gb} should be 40 times faster than in our numerical experiment, a value D_{gb} = 3x10^{-9} m^2/s. More than 4 orders of magnitude than the intracrystalline diffusion along γ at 700°C.

Figure 6.14 (next page): Numerical modelling of the contribution of δ.s on H/D exchange with Idefick. Diffusion coefficient for the experiments were set along α (Dx = 2x10^{-14}), along γ (Dy = 8x10^{-14}) and gain boundary diffusion (Dgb = 8x10^{-11}).

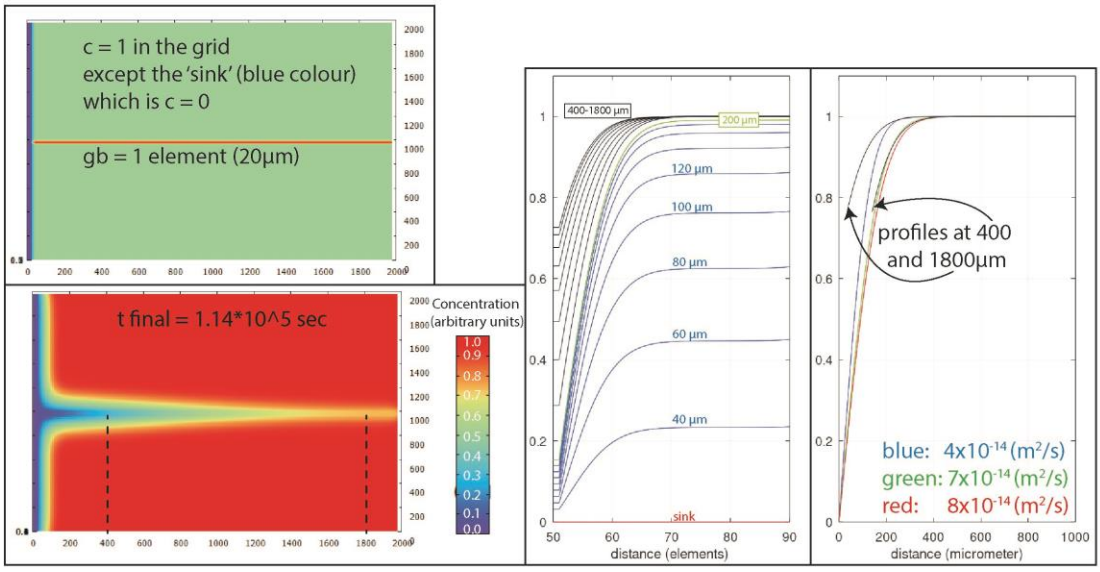
c = 1 in the grid
except the 'sink' (blue colour)
which is c = 0
gb = 1 element (20µm)
t final = 1.14*10^5 sec
Concentration
(arbitrary units)
400-1800 µm
200 µm
120 µm
100 µm
80 µm
60 µm
40 µm
sink
distance (elements)
profiles at 400
and 1800µm
blue: 4x10-14 (m2/s)
green: 7x10-14 (m2/s)
red: 8x10-14 (m2/s)
distance (micrometer)

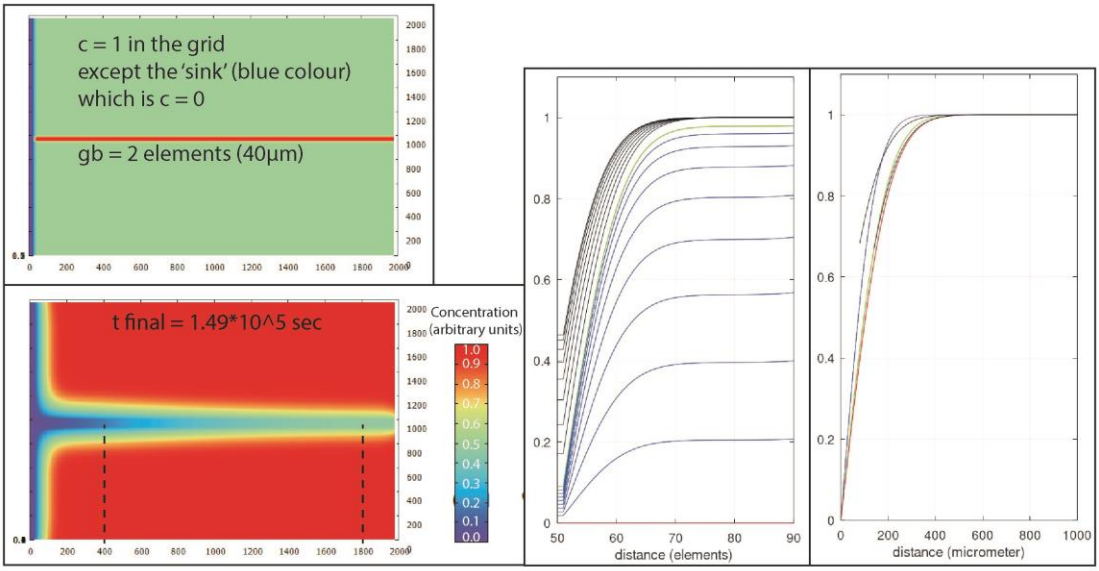
c = 1 in the grid
except the 'sink' (blue colour)
which is c = 0
gb = 2 elements (40µm)
t final = 1.49*10^5 sec
Concentration
(arbitrary units)
distance (elements)
distance (micrometer)

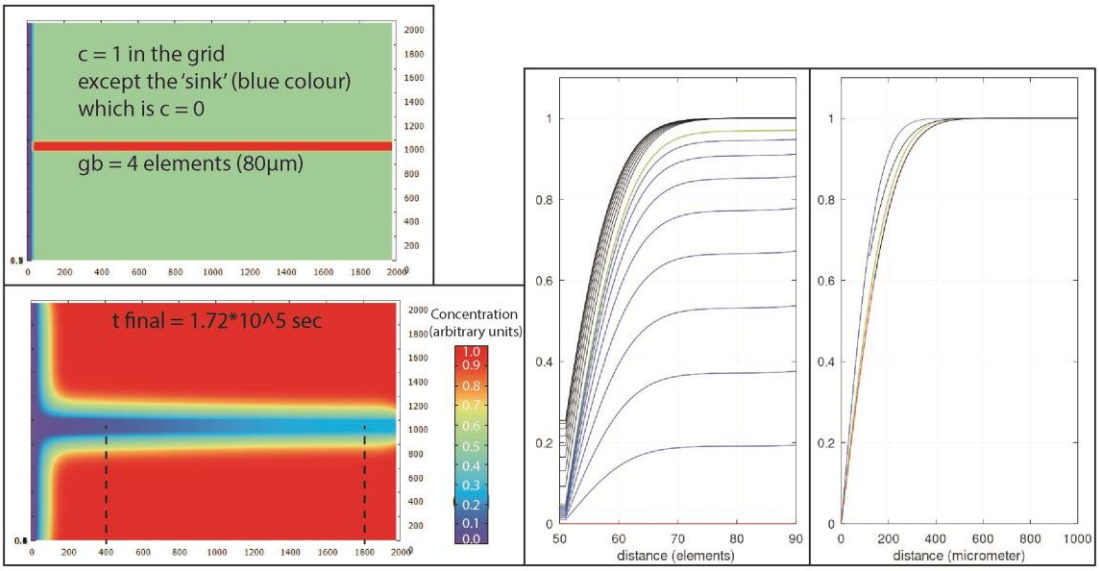
c = 1 in the grid
except the 'sink' (blue colour)
which is c = 0
gb = 4 elements (80µm)
t final = 1.72*10^5 sec
Concentration
(arbitrary units)
distance (elements)
distance (micrometer)

Implication for the interpretation of hydrogen isotope signatures of NAMs minerals in xenoliths

In their study of the isotopic composition of hydrogen in nominally anhydrous mantle minerals Bell and Ihinger (2000) reports analyses performed on cpx and garnet megacrysts and from opx single crystals from a spinel lherzolite xenolith. All samples record low δD values between -90 and -120‰. Without excluding the possibility of late exchanges with fluid or magma, the authors favored a primary mantle origin of this depleted signatures. They claimed that mantle NAMs may represent an isotopic mantle hydrogen reservoir distinct of the one of hydrous minerals. Harmon et al. (1987) in a study of hydrogen isotopic composition of basalts and the associated xenoliths from the Rhine valley had already obtained similar isotopic values for both whole rocks, mantle peridotite xenoliths and basalts (-83 to -95 ‰ and -76 to -106 ‰ for peridotites and basalts, respectively).

Later, two isotopic studies by ion probe were conducted on different samples from Nushan volcano (SE China); one on cpx megacrysts (Xia et al. 2004) and a second on cpx and opx crystals from peridotite xenoliths (Yu et al. 2005). The studies show that megacrysts, which are larger than 2 cm in size, have a less depleted hydrogen signature than the mm size cpx and opx grains within xenoliths (-45 to -111‰ versus -90 to -140 ‰, respectively).

The first study shows that the megacrysts were homogeneous in elements composition, as well as O, and H isotopes. They were all crystallized from parent magmas of the host basalt. Two distinct groups of megacrysts were identified and the difference between the two groups was interpreted by a crystallization inside different magma chambers, probably at different depths (Group I and II, Fig. 6.15). The decrease of δD with the decrease of Mg# in group II was interpreted as due to a possible crustal contamination and magma degassing during the crystallization.

The second study shows also that δD is constant within a single grain and among grains from the same xenolith. All xenoliths were spinel lherzolites. Cpx grains from three xenoliths and cpx and opx grains from a fourth xenolith were analyzed. All grains except those from one xenolith have δD depleted signatures. No difference is observed between cpx and opx. Like Bell and Ihinger (2000) before, the authors assume that the hydrogen isotopic compositions of the pyroxenes from these xenoliths represent the isotopic composition of the mantle source.

The results of our diffusion experiments raise doubt about theses interpretations. In few hours, a degassing magma would have affected the isotopic signature of pyroxenes in most parts of the

xenoliths (if not all). Considering their large size (2 cm) it is possible that cpx megacrysts preserved evidence of late magma degassing but a mm-size pyroxenes in a xenolith with fast grain boundary diffusion is unable to preserve mantle isotopic signature. The signature recorded by the pyroxenes of the Nushan xenoliths are more probably representative of the re-equilibration of the xenolith at the late stage of the degassed magma as recorded by the most depleted cpx megacrysts of group II in the study by Xia et al. (2004). These megacrysts have δD values below 100 ‰ comparable to the one recorded by xenoliths (Fig. 6.15).

Few years later, O'Leary (2007) reported in their thesis hydrogen isotopic analyses performed by continuous-flow mass spectrometry in mantle pyroxenes from three xenoliths, one spinel lherzolite from Kilbourne Hole (USA), one spinel lherzolite and one pyroxenite from Cerro Mercedes (Nicaragua). To our knowledge, these data have not been published as a paper in an international journal. The method they developed need only 5 – 40 mg of pyroxenes (O'Leary et al., 2007). With δD_{cpx} = -113 ± 6, δD_{opx} = -127 ± 6 ‰ for Kilbourne Hole and δD_{cpx} = -97 ± 12, δD_{opx} = -78 ± 1 ‰ for the Cerro Mercedes, they also confirm the δD depletion of these mantle xenoliths. They interpret their results by an effect of degassing of H_2O in the magma, suggesting that the isotopic signature of the pyroxenes could be re-equilibrated on time-scale of hours or days. This interpretation is validated by our experiments, which suggest that hydrogen isotopic diffusion in gb is fast enough to allow such late re-equilibration at magma temperatures.

In the last years, the study of the relationship between degassing and δD depletion of lava was mostly focused on the study of rhyolitic magmas (see for instance Walter and Castro 2020 and references herein). It has been demonstrated that prior and during eruption degassing fractionation produce a depletion of δD in the melt (Fig. 6.16a). Therefore, it is clear that it would be very difficult to preserve any original isotopic signature in xenoliths from the lithospheric mantle.

In our experiments, only isotopic exchange was observed because it was faster than the water content re-equilibration in the pyroxenes of the xenoliths. However, it is not clear in natural samples if the isotopic depletion is associated or not with a loss of water from the pyroxenes, but it can be legitimate to question it considering our previous observation in Ray-Pic xenoliths.

It was demonstrated in the case of rhyolitic volcanoes, that the passage of the explosive to effusive behavior was a continuous process. Even if degassing is larger in lava flow, it is a continuous process also during the explosive period of eruptions and all the products can be more or less affected by degassing (Castro et al. 2014; Fig. 6.16b). There is no reason to believe that it

would be different for basaltic volcanoes. Therefore, it raises one important question: the water content in the lithospheric mantle may be higher than what is generally estimated from measurements done in xenoliths even if they are sampled in pyroclastic products. It also suggests a new possible approach to estimate this uncertainty, a systematic measurement of hydrogen isotopic concentration in pyroxenes could be a useful method to validate (or not) the water concentration measured and eventually proposed a correction of the estimation of the water content in the lithospheric mantle.

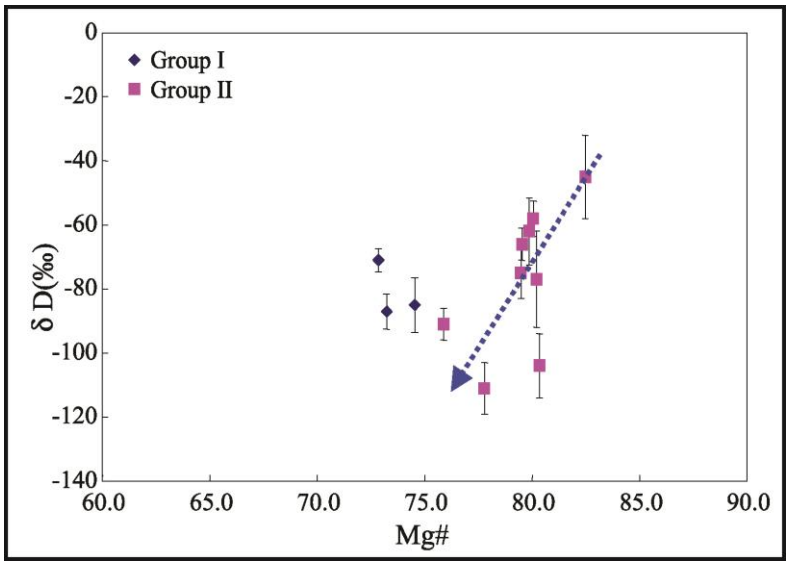

Fig. 6.15: Mg content versus δD values of the Nushan cpx megacrysts. Figure reproduced from Xia et al. 2004.

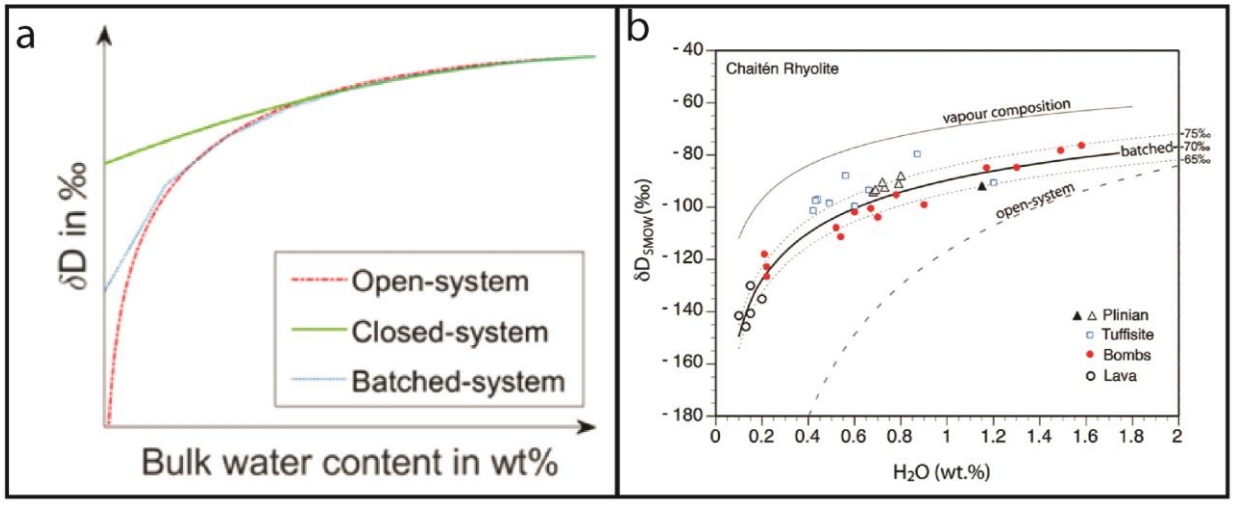

Fig. 6.16: a) Qualitative trends of hydrogen isotope fractionation during different degassing modes. Figure reproduced from Walter and Castro 2020. **b)** Chaitén δD bulk H_2O data compared to open-system and batched degassing models. Figure reproduced from Castro et al. 2014.

6.3 Conclusion

We know that when it comes to hydrogen diffusion in single crystals olivines from mantle xenoliths the time scales they need to reach a steady-state is in the order of minutes to hours (Ferriss et al., 2018), meaning that the hydrogen content in olivines has most of the time re-equilibrated with the host magma during ascent to surface. It may suggest that water in mantle xenoliths is equilibrated with the host magma and any profile observed in olivines from mantle xenoliths is just an updated signature from the final stage of ascent. The same question may be raised for pyroxenes, despite they are generally considered more capable to preserve deep water information than olivine and rarely show diffusion profiles.

However, these interpretations for olivine are based on the assumption that kinetics of hydrogen exchange between grains in xenoliths and melt are the same than the ones in single crystals, like for phenocrysts. It assumes that hydrogen transport through grain boundaries in the xenoliths is fast enough to not delay this exchange. Nobody knows yet if this assumption is true. This exploratory experimental work is a first attempt to constrain the rate of hydrogen isotopes exchange in real mantle xenoliths. It may not be a perfect approach; it nevertheless provides new information on the question; present new data and provides explanation for the observed δD signatures in most mantle xenoliths:

- First we confirm the diffusion laws for intracrystalline 'H self-diffusion' in mantle opx:

$$D_{\gamma}^{H} = D_0 \exp\left(\frac{-152{,}4 \pm 7{,}8\ kJmol^{-1}}{RT}\right), \text{ with } D_0 = -1.2\ (\pm 2.6)\ x10^{-5}$$

$$D_{a}^{H} = D_0 \exp\left(\frac{-157.8 \pm 14.5\ kJmol^{-1}}{RT}\right), \text{ with } D_0 = -6.5\ (\pm 5.4)\ x10^{-6}$$

  They are comparable to the ones proposed by Stalder and Behrens (2006). We confirm that, the fastest diffusion is along γ direction and the slowest along α direction. Diffusion laws have comparable activation energy (around 155 kJ/mol).

- The H/D exchange in opx inside xenolith cubes of 1 cm^3 are only slightly slower than with opx at the surface of the cubes in contact with the deuterium enriched gas. Assuming that the difference of the apparent diffusion rate with the normal intracrystalline diffusion rate is essentially due to a control of the diffusion by the grain boundaries, we estimated a lower limit for 'H self-diffusion' in grain boundaries D_{gb}:

$$\text{Log } D_{gb} \geq \text{Log} D_{\gamma}^{H} + 2.5$$

We cannot totally rule out the possibility of some bias of the results due to the presence of preexisting cracks, acting as shortcuts of diffusion, within the crystals of the cubes of xenolith. However, if there are some, they do not constitute a fully connected network. It means that grain boundaries are still involved, acting as bottleneck for the diffusion along the diffusion path. We believe that our estimations of D_{gb} is still conservative. An even more conservative estimation

- The semi-quantitative result can be used and extrapolated to the natural conditions. A fast exchange of H/D within the xenolith is expected at the temperature of the melt. Any late degassing of the melt will induce a depletion of δD in the melt that will reset rapidly the δD isotopic signature of the pyroxenes in the xenolith inducing depletion. Our results are in agreement with the most recent δD isotopic data in from mantle xenoliths.

Now that the approach has been set-up and has proved some adequacy, it would be interesting to apply it on bigger pieces of xenoliths (for instance, 10 – 20 cm^3) and if possible with more limited cracks.

7. Conclusions and future perspectives

Our work focused on different lava flows has shown that there is no obvious link between the specific location of the samples in the basalt and their total water content, during magma cooling and solidification. Even in the case of samples that travel more than 10 km within the lava flow, the water content in the pyroxenes inside the xenoliths, do not reveal any strong correlation. However, what it seems to affect hydrogen concentration is the degree of the magma degassing, i.e. explosive eruptions versus effusive eruptions. Pyroxenes from the samples in a pyroclastic deposit in Ray Pic (explosive style) contain more water than the samples from the lava flow (effusive style). This is a strong evidence that hydrogen content is influenced by the degree of degassing of the magma prior to eruption, something that can fluctuate during the lifespan of the volcano according to different magmatic processes e.g. magma mixing, magma recharge, degassing etc. Although, magma degassing affects water content, it appears to have limited impact in the hydrogen spectral signatures of pyroxenes. Pyroxenes with different signatures (type 1 and 2) coexist in the same lava flow and preserve these signatures, which are likely obtained deeper prior emplacement of the basaltic body, prior eruption and even prior degassing.

In the experimental and numerical study, we explored the importance of grain boundary diffusion in the preservation of the δD in pyroxenes from mantle xenoliths. We estimate that the hydrogen isotopic diffusion in the grain boundary is at least 2 log units higher than intracrystalline diffusion. However, more important than this value, the flux of deuterium is large and fast enough to rapidly equilibrate opx crystals inside the xenolith. This has a great impact on the preservation of hydrogen isotopic signature of xenoliths, showing that degassing magmas can easily result in a total reset from mantle δD values.

Future work, focusing in expanding the understanding on the same direction, would need more analyses exploring further hydrogen diffusion experiments to understand why spectral signatures are preserved in pyroxenes. Adding the pressure component in the experiments could also bring them one-step closer to nature reality. Another interesting idea could also be to perform experiments in bigger xenolithic cubes in an attempt to confirm and better constrain the present interpretation of H/D diffusion in grain boundaries. We could not achieved during this thesis a complete numerical modelling of the contribution of the grain boundaries in our samples. It is surely something we will push further in first priority.

8. References

Azevedo-Vannson, S., France, L., Ingrin, J., Chazot, G. (2021). Mantle metasomatic influence on water contents in continental lithosphere: New constraints from garnet pyroxenite xenoliths (France & Cameroon volcanic provinces). Chemical Geology, 575, 120257. doi:10.1016/j.chemgeo.2021.120257

Balan, E., Blanchard, M., Yi, H., Ingrin, J. (2012). Theoretical study of OH-defects in pure enstatite. Physics and Chemistry of Minerals, 40(1), pp.41-50.

Balan, E., Paulatto, L., Liu, J., Ingrin, J. (2020). Low-temperature infrared spectrum and atomic-scale structure of hydrous defects in diopside. European Journal of Mineralogy, 32(5), pp.505-520.

Balluffi, R.W., Allen, S.M., Carter, W.C., (2005). Kinetics of Materials. Wiley-Interscience, Hoboken. 645 pp.

Bell D.R., Rossman G.R. (1992). Water in the Earth's mantle: the role of nominally anhydrous minerals. Science 255:1391–1397.

Bell, D.R., Ihinger, P. D., (2000). The isotopic composition of hydrogen in nominally anhydrous mantle minerals. Geochimica et Cosmochimica Acta, 64(12), pp.2109-2118.

Bell, D.R., Ihinger, P. D., Rossman, G. R. (1995). Quantitative analysis of trace OH in garnet and pyroxenes. American Mineralogist, vol. 80, no. 5-6, pp. 465-474.

Berry, A., Hermann, J., O'Neill, H., Foran, G., (2005). Fingerprinting the water site in mantle olivine. Geology, 33(11), p.869-872.

Berry, A., O'Neill, H., Hermann, J., Scott, D., (2007). The infrared signature of water associated with trivalent cations in olivine. Earth and Planetary Science Letters, 261(1-2), pp.134-142.

Blanchard, M., Ingrin, J. (2004). Kinetics of deuteration in pyrope. European Journal of Mineralogy 16, 567-576.

Blanchard, M., Ingrin, J., Balan, E., Kovács, I., Withers, A. (2017). Effect of iron and trivalent cations on OH defects in olivine. American Mineralogist, 102(2), pp.302-311.

Bräuer, K., Kämpf, H., Niedermann, S., Wetzel, H.-U. (2017). Regional distribution pattern of carbon and helium isotopes from different volcanic fields in the French Massif Central: Evidence for active mantle degassing and water transport. Chemical Geology, 469, 4–18.

Brey, G. P., Köhler, T., (1990). Geothermobarometry in Four-phase Lherzolites II. New Thermobarometers, and Practical Assessment of Existing Thermobarometers, Journal of Petrology, Volume 31, Issue 6, 1353–1378.

Carpenter Wood, S., (2001). The Kinetics of Hydrogen Diffusion in Single Crystal Orthopyroxene. Dept. Geosciences, Pennsylvania State University.

Castro, J., Bindeman, I., Tuffen, H., Ian Schipper, C., (2014). Explosive origin of silicic lava: Textural andδD–H 2 O evidence for pyroclastic degassing during rhyolite effusion. Earth and Planetary Science Letters, 405, pp.52-61.

Chen, Y., Provost, A., Schiano, P., Cluzel, N. (2011). The rate of water loss from olivine-hosted melt inclusions. Contributions to Mineralogy and Petrology, 162(3), 625–636. doi:10.1007/s00410-011-0616-5

Chevrot, S., Villaseñor, A., Sylvander, M., Benahmed, S., Beucler, E., Cougoulat, G., Delmas, P., de Saint Blanquat, M., Diaz, J., Gallart, J., Grimaud, F., Lagabrielle, Y., Manatschal, G., Mocquet, A., Pauchet, H., Paul, A., Péquegnat, C., Quillard, O., Roussel, S., Ruiz, M., Wolyniec, D. (2014). High-resolution imaging of the Pyrenees and Massif Central from

the data of the PYROPE and IBERARRAY portable array deployments. Journal of Geophysical Research 119, 6399–6420.
Deer, W., Howie, R., Zussman, J., (2013). An Introduction to the Rock-Forming Minerals. London: Mineralogical Society of Great Britain & Ireland.
Della Ventura, G., Hawthorne, F., Robert, J.L., Iezzi, G. (2003) Synthesis and infrared spectroscopy of amphiboles along the tremolite-pargasite join. European Journal of Mineralogy, 15, 341-347
Demers-Roberge, A., Jollands, M. C., Müntener, O., Tollan, P. (2021). Variability of hydrogen defects in mantle orthopyroxene. across a back-arc transect in Southern Patagonia. Abstract Goldschmidt conference Lyon, 4 July - 9 July 2021.
Demouchy, S. (2010). Diffusion of hydrogen in olivine grain boundaries and implications for the survival of water-rich zones in the Earth's mantle. Earth and Planetary Science Letters 295, 305–313.
Demouchy, S., Bolfan-Casanova, N. (2016), Distribution and transport of hydrogen in the lithospheric mantle: A review. Lithos 240–243, 402-425.
Demouchy, S., Mackwell, S., (2006). Mechanisms of hydrogen incorporation and diffusion in iron-bearing olivine. Physics and Chemistry of Minerals 33, 347–355.
Demouchy, S., Mackwell, S.J., (2003). Water diffusion in synthetic iron-free forsterite. Physics and Chemistry of Minerals 30, 486–494.
Denis, C. M. M., Alard, O., Demouchy, S. (2015). Water content and hydrogen behaviour during metasomatism in the uppermost mantle beneath Ray Pic volcano (Massif Central, France). Lithos, 236-237, 256–274. doi:10.1016/j.lithos.2015.08.013
Denis, C., Demouchy, S., Shaw, C. (2013). Evidence of dehydration in peridotites from Eifel Volcanic Field and estimates of the rate of magma ascent. Journal of Volcanology and Geothermal Research, 258, pp.85-99.
Dohmen, R., Milke, R. (2010). Diffusion in Polycrystalline Materials: Grain Boundaries, Mathematical Models, and Experimental Data. Reviews in Mineralogy and Geochemistry, 72(1), 921–970.
Downes, H., Dupuy, C. (1987). Textural, isotopic and REE variations in spinel peridotite xenoliths, Massif Central, France. Earth and Planetary Science Letters 82, 121–135.
Du Frane, W., Tyburczy, J., (2012). Deuterium-hydrogen exchange in olivine: Implications for point defects and electrical conductivity. Geochemistry, Geophysics, Geosystems, 13(3), Q03004, doi:10.1029/2011GC003895.
Farver, J., (2010). Oxygen and Hydrogen Diffusion in Minerals. Reviews in Mineralogy and Geochemistry, 72(1), pp.447-507.
Faure, M., Lardeaux, J., Ledru, P. (2009). A review of the pre-Permian geology of the Variscan French Massif Central. Comptes Rendus Geoscience, 341(2-3), pp.202-213.
Fei H., Koizumi S., Sakamoto N., Hashiguchi M., Yurimoto H., Marquardt K., Miyajima N., Yamazaki D., Katsura T. (2016). New constraints on upper mantle creep mechanism inferred from silicon grain-boundary diffusion rates. Earth and Planetary Science Letters 433, 350-359.
Ferriss, E., Plank, T., Newcombe, M., Walker, D., Hauri, E., (2018). Rates of dehydration of olivines from San Carlos and Kilauea Iki. Geochimica et Cosmochimica Acta, 242, pp.165-190.
Ferriss, E., Plank, T., Walker, D., (2016). Site-specific hydrogen diffusion rates during clinopyroxene dehydration. Contributions to Mineralogy and Petrology, 171(6).

Frost, D., Dolejs, D., (2007). Experimental determination of the effect of H2O on the 410-km seismic discontinuity. Earth and Planetary Science Letters, 256(1-2), pp.182-195.

Gardner J., Tielke J., Mecklenburgh J., Mariani E., Wheeler J. (2020). Do grain boundaries act as a water reservoir in Earth's mantle? Abstract EGU 2020.

Gatta, G., Hradil, K. and Meven, M., (2021). Where is the Hydrogen? Elements, 17(3), pp.163-168.

Granet, M., Wilson, M., Achauer, U. (1995). Imaging a mantle plume beneath the French Massif Central. Earth and Planetary Science Letters, 136(3-4), 281–296. doi:10.1016/0012-821x(95)00174-b

Grant, K., Ingrin, J., Lorand, J.P., Dumas, P. (2007). Water partitioning between mantle minerals from peridotite xenoliths. Contributions to Mineralogy and Petrology, 154, 15–34.

Gu, X. (2016). Melt-rock interaction signatures in peridotite from sub-continental mantle (French Massif Central): A trace element, H, Li and δ7Li approach. PhD thesis, University of Lorraine, Nancy, 178 pp.

Gu, X., Deloule, E., France, L., Ingrin, J. (2016). Multi-stage metasomatism revealed by trace element and Li isotope distributions in minerals of peridotite xenoliths from Allègre volcano (French Massif Central). Lithos, 264, 158–174.

Gu, X., Ingrin, J., Deloule, E., France, L., Xia, Q. (2018). Metasomatism in the sub-continental lithospheric mantle beneath the south French Massif Central: Constraints from trace elements, Li and H in peridotite minerals. Chemical Geology, 478, 2–17.

Harmon, R., Hoefs, J. and Wedepohl, K., (1987). Stable isotope (O, H, S) relationships in Tertiary basalts and their mantle xenoliths from the Northern Hessian Depression, W.-Germany. Contributions to Mineralogy and Petrology, 95(3), pp.350-369.

Harrison, L.G., (1961). Influence of dislocations on diffusion kinetics in solids with particular reference to the alkali halides. Trans. Faraday Soc. 57, 1191–1199. doi:10.1039/TF9615701191.

Harvey, J., Gannoun, A., Burton, K. W., Schiano, P., Rogers, N. W., Alard, O. (2010). Unravelling the effects of melt depletion and secondary infiltration on mantle Re–Os isotopes beneath the French Massif Central. Geochimica et Cosmochimica Acta, 74(1), 293–320.

Hercule, S., Ingrin, J., (1999). Hydrogen in diopside: Diffusion, kinetics of extraction-incorporation, and solubility. American Minerologist 84, 1577–1587.

Hiraga T., Kohlstedt D. (2007). Equilibrium interface segregation in the diopside–forsterite system I: Analytical techniques, thermodynamics, and segregation characteristics. Geochimica et Cosmochimica Acta, 71(5), pp.1266-1280.

Hiraga, T., Anderson, I., Kohlstedt, D. (2004). Grain boundaries as reservoirs of incompatible elements in the Earth's mantle. Nature, 427(6976), pp.699-703.

Ingrin, J. (2021). OH signature of pyroxenes: A new probe for studying lithospheric processes? Goldschmidt Lyon 2021

Ingrin, J., Blanchard, M. (2006). Diffusion of hydrogen in minerals. Water in Nominally Anhydrous Minerals. Rev. Mineral. Geochem. vol. 62, 291–320.

Ingrin, J., Hercule, S., Charton, T. (1995). Diffusion of hydrogen in diopside: Results of dehydration experiments. Journal of Geophysical Research: Solid Earth, 100(B8), 15489–15499. doi:10.1029/95jb00754

Ingrin, J., Latrous, K., Doukhan, J. Doukhan, N., (1989). Water in diopside: an electron microscopy and infrared spectroscopy study. European Journal of Mineralogy, 1(3), pp.327-342.

Ingrin, J., Skogby, H. (2000). Hydrogen in nominally anhydrous upper-mantle minerals: concentration levels and implications. European Journal of Mineralogy 12, 543–570.
Karato, S. (2006). Influence of Hydrogen-Related Defects on the Electrical Conductivity and Plastic Deformation of Mantle Minerals: A Critical Review. Earth's Deep Water Cycle, V.168, pp.113-129.
Karato, S. (2008). Deformation of Earth Materials. Cambridge: Cambridge University Press
Karato, S., Spetzler, H., (1990). Defect microdynamics in minerals and solid-state mechanisms of seismic wave attenuation and velocity dispersion in the mantle. Reviews of Geophysics, 28(4), p.399.
Kaur I., Mishin Y., Gust W. (1995). Fundamentals of Grain and Interphase Boundary Diffusion, 3ed Revised and Enlarged Edition, Wiley New York.
Kelley, K.A., Plank, T., Grove, T. L., Stolper, E.M., Newman, S., Hauri, E., (2006). Mantle melting as a function of water content beneath back-arc basins. Journal of Geophysical Research, 111(B9), B09208.
Kohlstedt, D.L., Mackwell, S.J., (1998). Diffusion of hydrogen and intrinsic point defects in olivine. Zeitschrift für Physikalische Chemie 207, 147–162.
Lemaire, C., Kohn, S., Brooker, R., (2004). The effect of silica activity on the incorporation mechanisms of water in synthetic forsterite: a polarised infrared spectroscopic study. Contributions to Mineralogy and Petrology, 147(1), pp.48-57.
Lenoir, X., Garrido, C. J., Bodinier, J.-L., & Dautria, J.-M. (2000). Contrasting lithospheric mantle domains beneath the Massif Central (France) revealed by geochemistry of peridotite xenoliths. Earth and Planetary Science Letters, 181(3), 359–375. doi:10.1016/s0012-821x(00)00216-8
Libowitzky, E., Rossman, G. R. (1997). An IR absorption calibration for water in minerals. American Mineralogist, 82(11-12), 1111–1115. doi:10.2138/am-1997-11-1208
Litasov, K., Ohtani, E., (2007). Effect of water on the phase relations in Earth's mantle and deep water cycle. Advances in High-Pressure Mineralogy, Geological Society of America, Special Paper 421.
Lloyd, A., Ferriss, E., Ruprecht, P., Hauri, E., Jicha, B., Plank, T., (2016). An Assessment of Clinopyroxene as a Recorder of Magmatic Water and Magma Ascent Rate. Journal of Petrology, 57(10), pp.1865-1886.
Lucazeau, F., Vasseur, G., Bayer, R. (1984). Interpretation of heat flow data in the French massif central. Tectonophysics, 103(1-4), 99–119. doi:10.1016/0040-1951(84)90077-5
Mackwell, S.J., Kohlstedt, D.L., (1990). Diffusion of hydrogen in olivine: implications for water in the mantle. Journal of Geophysical Research 95, 5079–5088.
Matte, P. (1986). Tectonics and plate tectonics model for the Variscan belt of Europe. Tectonophysics, 126(2-4), 329–374. doi:10.1016/0040-1951(86)90237-4
Mercier, J.-C. C., Nicolas, A. (1975). Textures and Fabrics of Upper-Mantle Peridotites as Illustrated by Xenoliths from Basalts. Journal of Petrology, 16(1), 454–487. doi:10.1093/petrology/16.1.454
Michon, L., Merle, O. (2001). The evolution of the Massif Central Rift; spatio-temporal distribution of the volcanism. Bulletin de la Société Géologique de France, 172(2), pp.201-211.
O'Leary J.A., (2007). Hydrogen isotope geochemistry of the mantle: constraints from back arc basin basalts and mantle xenoliths, PhD Thesis, California Institute of Technology

Padrón-Navarta, J.A., Hermann, J., O'Neill, H.S.C., (2014). Site-specific hydrogen diffusion rates in forsterite. Earth and Planetary Science Letters 392, 100–112.

Palme H., O'Neill Hugh St. C. (2005). Cosmochemical Estimates of Mantle Composition, in The Mantle and Core. Edited by Richard W. Carlson. Oxford: Elsevier Ltd., pp. 1–38.

Panchuk, K., (2019). Physical Geology - First University of Saskatchewan Edition. [S.l.]: University of Saskatchewan.

Patkó, L., Liptai, N., Kovács, I., Aradi, L., Xia, Q., Ingrin, J., Mihály, J., O'Reilly, S., Griffin, W., Wesztergom, V., Szabó, C., (2019). Extremely low structural hydroxyl contents in upper mantle xenoliths from the Nógrád-Gömör Volcanic Field (northern Pannonian Basin): Geodynamic implications and the role of post-eruptive re-equilibration. Chemical Geology, 507, pp.23-41.

Peck, D. L. (1978). Cooling and vesiculation of Alae Lava Lake, Hawaii, Tech. Rep., U. S. Govt. Print. Off., Washington, D. C.

Pelleg, J. (2016). Diffusion in ceramics, Solid Mechanics and Its Applications, Mechanism of Diffusion Springer International Publishing Switzerland pp. 31–39.

Peslier A.H., Schönbächler M., Busemann H., Karato S.I. (2017). Water in the Earth's Interior: Distribution and Origin. Space Sci Rev 212, 743–810.

Peslier, A. H. (2010). A review of water contents of nominally anhydrous natural minerals in the mantles of Earth, Mars and the Moon. Journal of Volcanology and Geothermal Research, 197(1-4), 239–258. doi:10.1016/j.jvolgeores.2009.10.006

Philpotts, A., Ague, J., (2018). Cooling of igneous bodies and other diffusion processes, Principles of Igneous and Metamorphic Petrology, Cambridge University Press, pp.111-129.

Plank, T., Kelley, K. A., Zimmer, M. M., Hauri, E. H., Wallace, P. J. (2013). Why do mafic arc magmas contain ~4wt% water on average? Earth and Planetary Science Letters, 364(), 168–179.

Prechtel, F., Stalder R. (2012). OH-defects in Al- and Cr-doped synthetic enstatites and defect geobarometry on natural orthopyroxenes from the Earth's mantle. European Journal of Mineralogy 24, 471–481.

Putnis, A., McConnell, J.D.C. (1980). Principles of mineral behaviour. Oxford: Blackwell Scientific Publications.

Sasco, R., Guillou, H., Nomade, S., Scao, V. Maury, R.C., Kissel, C. Wandres, C. (2017). $^{40}Ar/^{39}Ar$ and unspiked ^{40}K- ^{40}Ar dating of upper Pleistocene volcanic activity in the Bas-Vivarais (Ardèche, France). Journal of Volcanology and Geothermal Research, S0377027317301294–. doi:10.1016/j.jvolgeores.2017.06.003

Shaw, H. R., Hamilton, M. S., Peck, D. L. (1977). Numerical analysis of lava lake cooling models; Part I, Description of the method. American Journal of Science, 277(4), 384–414. doi:10.2475/ajs.277.4.384

Shen, T., Hermann, J., Zhang, L., Padrón-Navarta, J. A., Chen, J. (2014). FTIR spectroscopy of Ti-chondrodite, Ti-clinohumite, and olivine in deeply subducted serpentinites and implications for the deep water cycle. Contributions to Mineralogy and Petrology, 167(4). doi:10.1007/s00410-014-0992-8

Skogby, H., Bell, D. R., Rossman G. R. (1990). Hydroxide in pyroxene; variations in the natural environment. American Mineralogist, 75 (7-8): 764–774.

Sobolev, S. V., Zeyen, H., Granet, M., Achauer, U., Bauer, C., Werling, F., Altherr, R., Fuchs, K. (1997). Upper mantle temperatures and lithosphere-asthenosphere system beneath the

French Massif Central constrained by seismic, gravity, petrologic and thermal observations. Tectonophysics, 275(1-3), 143–164. doi:10.1016/s0040-1951(97)00019-x
Sommer H., Regenauer-Lieb K., Gasharova B., Siret D. (2008). Grain boundaries: a possible water reservoir in the Earth's mantle? Mineralogy & Petrology 94, 1–8.
Stalder, R. (2004). Influence of Fe, Cr and Al on hydrogen incorporation in orthopyroxene. European Journal of Mineralogy, 16(5), 703–711. doi:10.1127/0935-1221/2004/0016-0703
Stalder, R., Behrens, H., (2006). D/H exchange in pure and Cr-doped enstatite: implications for hydrogen diffusivity. Physics and Chemistry of Minerals, 33(8-9), pp.601-611.
Stalder, R., Karimova, A., Konzett, J. (2015). OH-defects in multiple-doped orthoenstatite at 4–8 GPa: filling the gap between pure and natural systems. Contributions to Mineralogy and Petrology, 169(4)
Stalder, R., Skogby, H., (2003). Hydrogen diffusion in natural and synthetic orthopyroxene. Physics and Chemistry of Minerals 30, 12–19.
Tian, Z., Liu, J., Xia, Q., Ingrin, J., Hao, Y., Christophe, D., (2017). Water concentration profiles in natural mantle orthopyroxenes: A geochronometer for long annealing of xenoliths within magma. Geology, 45(1), pp.87-90.
Towbin, W.H., Plank, A.T., (2021). Water in mantle xenoliths: magma ascent too slow to preserve lithospheric water concentrations, Goldschmidt 2021 abstracts
Uenver-Thiele, L., Woodland, A. B., Seitz, H.-M., Downes, H., Altherr, R. (2017). Metasomatic Processes Revealed by Trace Element and Redox Signatures of the Lithospheric Mantle Beneath the Massif Central, France. Journal of Petrology, 58(3), 395–422. doi:10.1093/petrology/egx020
Van der Meijde, M., Marone, F., Giardini, D., Van der Lee, S., (2003). Seismic Evidence for Water Deep in Earth's Upper Mantle. Science, 300(5625), pp.1556-1558.
Walker, A., Hermann, J., Berry, A., O'Neill, H. (2007). Three water sites in upper mantle olivine and the role of titanium in the water weakening mechanism. Journal of Geophysical Research, 112(B5).
Walter, S., Castro, J., (2020). VolcDeGas: A program for modelling hydrogen isotope fractionation during degassing of rhyolitic melts. Volcanica, 3(1), pp.155-168.
Warren, J., Hauri, E., (2014). Pyroxenes as tracers of mantle water variations. Journal of Geophysical Research: Solid Earth, 119(3), pp.1851-1881.
Withers A.C., Bureau H., Raepsaet C., Hirschmann M.M. (2012). Calibration of infrared spectroscopy by elastic recoil detection analysis of H in synthetic olivine. Chemical Geology 334, 92–98.
Wittig, N., Baker, J. A., Downes, H. (2007). U–Th–Pb and Lu–Hf isotopic constraints on the evolution of sub-continental lithospheric mantle, French Massif Central. Geochimica et Cosmochimica Acta, 71(5), 1290–1311. doi:10.1016/j.gca.2006.11.025
Wittmann, W., Sigmundsson, F., Dumont, S., Lavallée, Y. (2017). Post-emplacement cooling and contraction of lava flows: InSAR observations and a thermal model for lava fields at Hekla volcano, Iceland. Journal of Geophysical Research: Solid Earth, 122(2), pp.946-965.
Xia, Q., Dallai, L., Deloule, E., (2004). Oxygen and hydrogen isotope heterogeneity of clinopyroxene megacrysts from Nushan Volcano, SE China. Chemical Geology, 209(1-2), pp.137-151.
Yang, X., Keppler, H., Li, Y., (2016). Molecular hydrogen in mantle minerals. Geochemical Perspectives Letters, pp.160-168.

Yu H., Xia, Q., Deloule, E., Yang X., (2005). Hydrogen Isotopic Compositions of Pyroxenes in Nushan Peridotite Xenoliths, SE China. Acta Geologica Sinica - English Edition, 79(3), pp.336-342.

Zangana, N.A., Downes, H., Thirlwall, M.F., Hegner, E. (1997). Relationship between deformation, equilibration temperatures, REE and radiogenic isotopes in mantle xenoliths (Ray Pic, Massif Central, France): an example of plume–lithosphere interaction? Contributions to Mineralogy and Petrology 127, 187–203.

Zangana, N.A., Downes, H., Thirlwall,M., Marriner, G., Bea, F. (1999). Geochemical variation in peridotite xenoliths and their constituent clinopyroxenes from Ray Pic (French Massif Central): implications for the composition of the shallow lithospheric mantle. Chemical Geology 153, 11–35.

Zimmer, M. M., Plank, T., Hauri, E. H., Yogodzinski, G. M. Stelling, P., Larsen, J., Singer, B., Jicha, B., Mandeville, C. Nye, C. J. (2010). The Role of Water in Generating the Calc-alkaline Trend: New Volatile Data for Aleutian Magmas and a New Tholeiitic Index. Journal of Petrology, 51(12), 2411–2444.

Acknowledgements

I would like to express my sincere gratitude to my supervisor Jannick Ingrin for trusting me this project for all the training, guidance and endless help during this PhD work. Without him, nothing would be possible. To my co-supervisor Pierre Hirel for his valuable feedback and his great aid for all the numerical modelling. A big thank you I want to give to my PhD exam committee, Sautter Violaine, Demouchy Sylvie, Deloule Etienne and Merkel Sébastien, for accepting to review this work and to Isabelle De Waele for all the help during the FTIR sessions.

For this great opportunity to pursue my PhD in France, from the warm welcome to the excellent cooperation, representing Lille University and France community, I would like to thank all the members of the Earth and Planetary Materials research group and more specific Julien for the many workout opportunities and Ahmed for all the small talk breaks.

For all the constructive conversations, the happy student moments and the unconditional support through this PhD, I would like to thank my fellow colleagues and new friends: Tommaso, the piadina master chef with the wild dreams; Jeff, the best CS teammate; Estelle, the most kind French lady I ever met; Dan, the chaos office manager; Jules, for his beautiful drawing; Pierre-Marie, Shanshan, Maxime, Maroua, Laïs, Mahira, Sylvain, Alexandre, Amelie, Maria, Prince and Talus for all the walks and fun we share together.

Special mention and gratitude goes to all the free internet sources of knowledge (Sci-Hub, Wikipedia, YouTube tutorials, etc.) and to all scientists that publish their work in open access journals. Another special thank you goes to the ground flight attendant that helped me travel in summer 2021 back to France, while the rest of her coworkers tried to cancel my flight because I did not had a COVID test, although I was fully vaccinated. I promised to her to add her here!

Last but far from least for their support, encouragement and absolute love throughout all these years, I would like to thank from my heart my family and my friends. Special thanks goes to: my niece Sophia and my nephew Christos, for all the relaxing time playing board games in all my vacation time when I was in Greece; to Alex for his help during Octave coding; to Hara for the endless support and companionship; to Sotiris and Kiki for introducing me in to Karato's work and their support; to the Spring Gamblers (Dimitra, Maria, Jimbo, Thanos) for all the skype meetings and the countless hours playing french tarot; to all my "Swedish family", George, Zisis, Milena, Christos, Haris etc. that supported my PhD journey in various and many ways; the Beerchope management, Lou and Romain, for helping me exploring the local beer world.

As mentioned in the first pages, this PhD work is dedicated to my parents, Olga and Ilias. They lived a simply and constrained life in order to fully support the intellectual development of their children, my sister Helen and myself. All the positive characteristics of my personality are a reflection of their parenting. Ψυχή βαθιά!

Appendix A1 – EGU 2019 abstract

Geophysical Research Abstracts
Vol. 21, EGU2019-**PREVIEW**, 2019
EGU General Assembly 2019

Do mantle xenoliths preserve water signature from the lithospheric mantle and how? An experimental and numerical approach.

Konstantinos Thomaidis, Jannick Ingrin, and Pierre Hirel
Univ. Lille, CNRS, INRA, ENSCL, UMR 8207 - UMET - Materials and Transformations, F-59000 Lille, France (konstantinos.thomaidis@univ-lille.fr)

Water presence as OH point defects in the main minerals (Opx, Cpx, Ol) of the upper mantle plays an important role in its fundamental properties (i.e. melting, plasticity, conductivity). It is widely assumed that the water signature recorded by mantle xenoliths is representative of mantle conditions, but this assumption remains a hypothesis and the question of how we can interpret the extensive OH data acquired worldwide on xenoliths is still unsolved.

The aim of this work is to evaluate the effect of the transport of mantle xenoliths in the concentration and distribution of water among the mineral phases of Opx and Cpx. This work will attempt to determine the diffusion mechanisms that control hydrogen exchange between the xenoliths and the host magma; looking at the rol of bulk diffusion versus grain boundary diffusion through experiments and numerical modelling. Experimental measurements done on natural samples will be used to interpret original data from mantle xenoliths.

Here we present our first results from annealing experiments performed in peridotite xenoliths from a Cenozoic strombolian volcano from the south of the French Massif Central. We jointly present the results of a finite element modelling of hydrogen diffusion in coexisting Opx and Cpx considering different diffusion rates of hydrogen in the grain boundary.

Appendix A2 – EGU 2020 abstract

Thomaidis, K. and Ingrin, J.: Role of grain boundary diffusion in H/D exchange in mantle xenoliths , EGU General Assembly 2020, Online, 4–8 May 2020, EGU2020-10930, https://doi.org/10.5194/egusphere-egu2020-10930, 2020.

Water concentration in pyroxenes from mantle xenoliths is frequently used to trace water content in the lithospheric mantle. We do not understand yet how these pyroxenes can preserve a memory of their deep equilibrium during their transports to the surface. In an attempt to evaluate the role of grain boundaries in the exchange of hydrogen between the pyroxenes of the xenoliths and the host magma; we have launched a program of experiments of H exchange in blocks of mantle xenoliths of centimetre size. The blocks, all from the same xenolith, contain clinopyroxenes, orthopyroxenes and olivine of the mm to sub-millimetre size. We present here the results of a series of H/D exchange performed at 600, 700 and 900 ^{o}C at room pressure in a deuterium enriched gas. OH-OD profiles recorded by micro-infrared spectroscopy in pyroxenes at the edge of the block are only slightly different from the ones recorded in pyroxenes at the centre of the block. These results show that the diffusion/solubility of hydrogen in grain boundaries is fast enough to equilibrate rapidly the grains at the center of the xenoliths. It proves that in nature the δD signature of xenoliths is very likely controlled by the equilibrium with the host magma even in the case of xenoliths with large grain size.

We will also present preliminary results on the role of grain boundary diffusion in the control of hydrogen exchange involving reaction activated at higher temperature such as the reaction involving the oxidation-reduction of iron ($1/2H_2 + Fe^{3+} = H_i^{+} + Fe^{2+}$) and reactions involving the formation/destruction of cation vacancies.

Appendix A3 – Goldschmidt 2021 abstract

Hydrogen isotopic exchange experiments in mantle xenoliths indicate rapid δD equilibrium with magma

K. THOMAIDIS[1]*, J. INGRIN[1] , P. HIREL[1],
[1] Univ. Lille, CNRS, INRAE, ENSCL, UMR 8207 - UMET - Unité Matériaux et Transformations, F-59000 Lille, France
(*correspondence: konstantinos.thomaidis@univ-lille.fr)

Water in the form of hydrous point defects in the crystal structure of pyroxenes from mantle xenoliths is frequently used to trace the water content in the lithospheric mantle. However, little is known on the mechanism that allows xenoliths to preserve deep hydrogen signatures and avoid complete reset by reaction with the host magma during transport. Especially, it is unknown how grain boundaries can affect hydrogen exchange between the different constitutive minerals and with the surrounding melt. In this study, we report results from hydrogen-deuterium exchange experiments performed in cubic pieces of natural xenolith aggregates between 600 and 900°C in a deuterium (D) enriched gas, at room pressure. The cubes, all from the same xenolith, contain clinopyroxenes, orthopyroxenes and olivine of mm to sub-millimetre size. We used single crystals of orthopyroxenes (opx), as sensors of the progress of the exchange within the polycrystalline aggregate. We compare diffusion profiles measured in single crystals and opx located at the edge of the cubes with diffusion profiles within opx inside the cubes not directly in contact with the deuterium enriched gas. Data are analysed to assess the possible contribution of grain boundary diffusion on the H/D equilibration of xenoliths during their transport to the surface. OH-OD profiles recorded by infrared spectroscopy in opx at the edge of the cubes are only moderately different from the ones recorded in opx inside the cubes. These results indicate that the isotopic diffusion of hydrogen in grain boundaries is fast enough to equilibrate rapidly the opx crystals inside the cube xenoliths. This can be a first evidence that in nature the δD signature of xenoliths is very likely controlled by the equilibrium with the host magma even in the case of xenoliths with large grain size.

Appendix B – Idefick

B1. Example of input file for 2D numerical simulation with Idefick.

```
// To run this example, enter: idefick input.txt

// Definition of media and their properties, here we define two different media, one anisotropic
// for opx crystal and one isotropic for grain boundary

medium M1 {D0 = 2.0e-14 8.0e-14}
// Opx diffusion coefficients along X and Y (m/s²) based on intracrystalline values for γ at 700°C
medium M2 {D0 = 1.0e-10 1.0e-10}
// Grain boundary diffusion coefficients along X and Y (m/s²)

// Definition of grid composition
{grid 2}                    // 2-D simulation
{Lx  2000.0 µm}             // Length of the cell and unit (m/mm/µm/nm)
{Ly  2000.0 µm}             // Width of the cell and unit (m/mm/µm/nm)
{NX  100}                   // Number of finite elements along X
{NY  100}                   // Number of finite elements along Y
{fill  1:2  1:100  M1 0}
{fill  3:100  1:46 M1 1}
{fill  3:100  47:50 M2 1}    // Grain boundary with 4 elements (80µm) thickness
{fill  3:100 51:100 M1 1}
{fix   1:2 1:100  M1 0}      // The 'sink' fixed concentration at zero
{bc free free}              // Boundary conditions along X and Y (fixed|free|periodic)
// Boundary conditions control the way the concentration evolves at the edges of the simulation
// setup.

// Definition of simulation setup
{duration 108 h}            // Simulation duration and unit (ms/s/min/h/d/y)
{T = 1000 K}                // Temperature in Kelvin, remains constant during the simulation
{maxSteps 10000000}         // Limit number of simulation steps

// Output
{Cx 25000}                   // Write concentration profile C(x,y) every N time steps
```

B2. Users interface through Windows PowerShell.

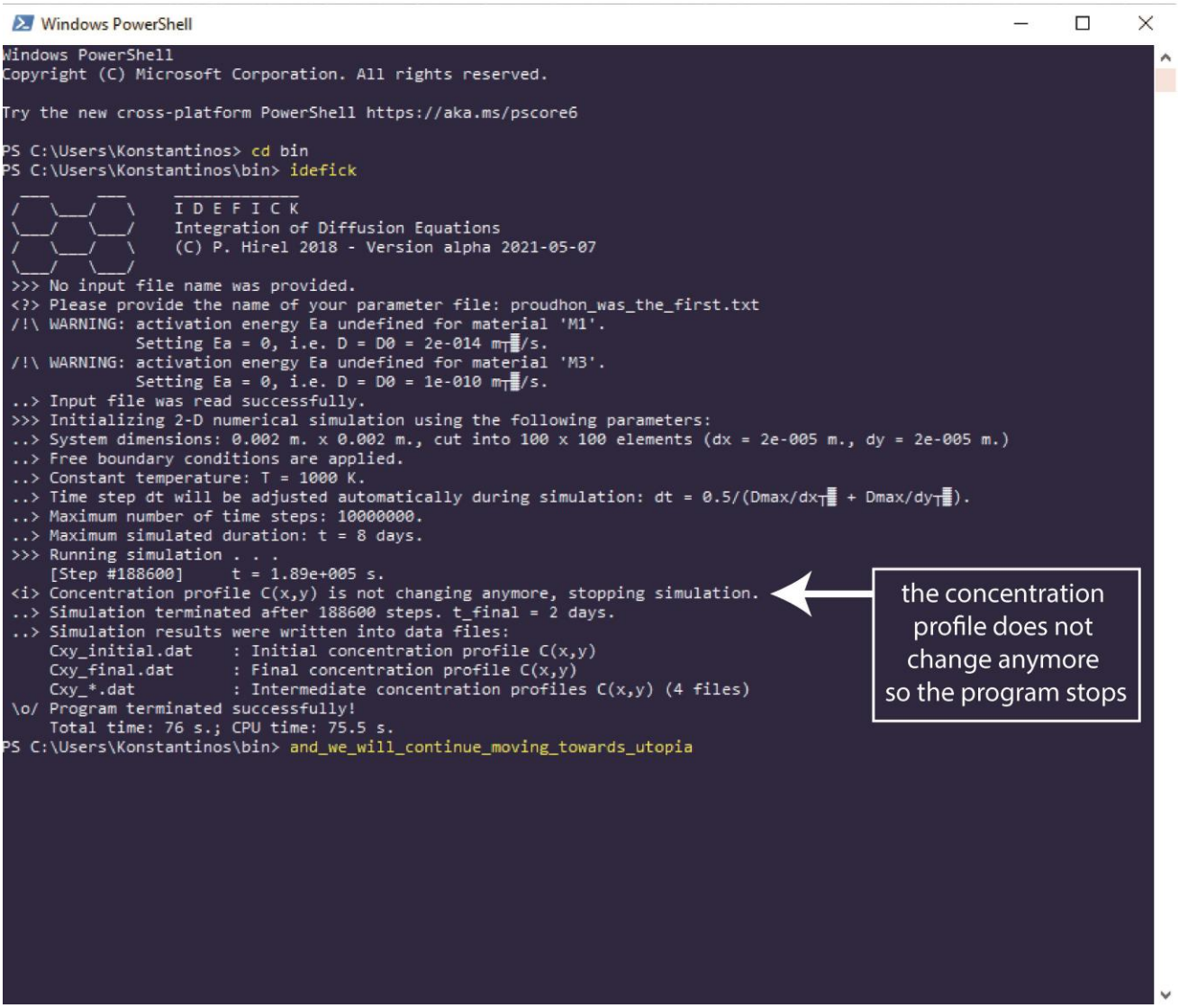

B3: Example of C(x,y) profile files at different time with two different grain boundaries thicknesses (lower 20 μm, higher 80μm). Specific example is just for presenting the potential benefits of working with Idefick.

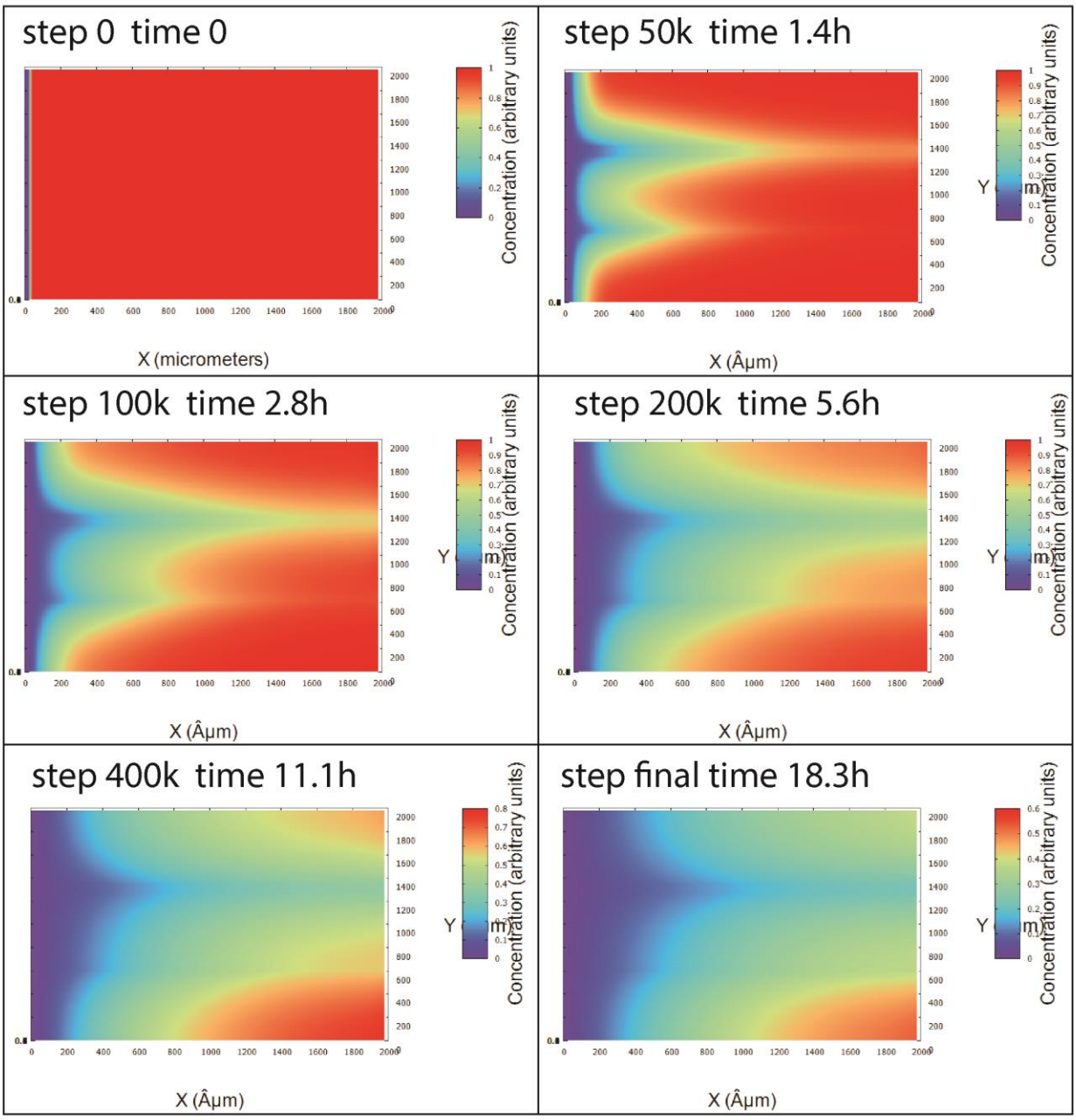

Appendix C – GNU Octave source code

---------- part 1 ----------

```
clear
clc # clear and clean any previous work
raw_data = load("-ascii", "cube5b.18092019.4.txt"); # select the txt file with the profile
spectra = raw_data(1:1763, 2:7); # choose the spectra values
x = raw_data (1:1763, 1); # choose line one for wavenumber values
clear raw_data # delete the file
m = 0.0295; # put the thickness of the cube slice
normalise = spectra/m; # normalise data by the thickness
distance=[40;70;100;130;160;190]; # add the distance of the profile from edge and steps
```

---------- part 2 ----------

```
x1a=x(119:160, 1); # select the front points for the integrated area of the OH peaks
x2a=x(412:450, 1); # select the back points or the integrated area of the OH peaks
xa=[x1a;x2a]; # combine the points
clear x1a;
clear x2a;
x1a=x(119:450); # select the whole range for the x axis
ya1=normalise(119:160,1); # select the same points for the y axis
ya2=normalise(412:450,1);
ya=[ya1;ya2];
clear ya1;
clear ya2;
pol3a=polyfit (xa, ya, 3); # polynomial interpolation 3rd degree p(x) = ax^3 + bx^2+ cx + d
p4a=pol3a(1,1); # a
p3a=pol3a(1,2); # b
p2a=pol3a(1,3); # c
p1a=pol3a(1,4); # d
x2a=x1a .* x1a; # x^2
x3a=x2a .* x1a; # x^3
poly_line3a=p1a+p2a .*x1a+p3a .*x2a+p4a .*x3a; # create the polynomial baseline
integral_linea=normalise(119:450,1)-poly_line3a; # cut from the spectra the integrated area
integral_a=trapz(x(119:450,1),integral_linea); # compute the approximate integral, value in cm^-2

# repeat for all the profile analysis spots and OD peaks as well

figure (1); subplot (2, 3, 1); plot (x, normalise); # visualize spectra for better evaluation
hold on
plot (x1a, poly_line3a, "k");
plot(xa,ya, "o","markersize", 2);
[…]
plot (x1aOD, poly_line3aOD, "k");
[…]
set(gca, 'XDir', 'reverse');
```

```
xlim ([2300, 4000]);
ylim ([2, 6]); # to be adjusted accordingly
xlabel ("wavenumber (cm-1)");
ylabel ("absorbance (cm-1)");
grid on;
hold off

figure (1); subplot (2, 3, 2);
plot (x1a, integral_linea); # extraction of the baseline, plot only peaks
hold on
plot (x1b, integral_lineb, "k");
[…]
plot (x1aOD, integral_lineaOD, "k");
[…]
set(gca, 'XDir', 'reverse');
xlim ([2300, 4000]);
ylim ([0, 1]); # to be adjusted accordingly
xlabel ("wavenumber (cm-1)");
ylabel ("absorbance (cm-1)");
grid on;
hold off
---------------------------------------------------------------------------------------- part 3 ----------
aOH=abs(integral_a);
[…]
OH=[aOH;bOH;cOH;dOH;eOH;fOH;gOH]

aOD=abs(integral_aOD);
[…]
OD=[aOD;bOD;cOD;dOD;eOD;fOD;gOD]

a=abs(integral_g-integral_a); #integral_g here is AOH0 but can be replaced with M1
[…]
AOH0AOHd=[a;b;c;d;e;f;g] # AOH0-AOHd or M1-AOHd

md = length(OD); # beta calculation
X = [ones(md, 1) OD];
theta = (pinv(X'*X))*X'*AOH0AOHd;

figure (1); subplot (2, 3, 3); plot (OD, AOH0AOHd, "o","markersize", 6); # beta plot
hold on
plot(X(:,2), X*theta, '-')
xlabel ("OD (cm-1)");
ylabel ("AOH0-AOHd");
grid on;

beta=theta(2)
```

```
AODs=abs(integral_g/beta)
constant_test=OH+OD*beta # testing that we have not lost any hydrogen
M1=mean(constant_test)
err=constant_test*0.2

constant_testx=[1;2;3;4;5;6;7]; # testing that we have not lost any hydrogen
figure (1);subplot (2, 3, 5);
plot(constant_testx, constant_test,"o","markersize", 2);
errorbar(constant_testx, constant_test,err,'o')
xlim ([0, 10]);
ylim ([0, 200]);
xlabel ("profile");
ylabel ("AOH+b*AOD");
grid on;
hold off

AOHdAOH0a=abs(integral_a/integral_g);
[…]
AOHdAOH0=[AOHdAOH0a…] #AOHd/AOH0 or AOHd/M1

AODdAODsa=aOD/AODs;
[…]
AODdAODs=[AODdAODsa…] #AOHd/AODs

onea=1-aOD/AODs;
[…]
one_minus_AODdAODs=[onea…] #1-AOHd/AODs

---------- part 4 ----------

D1=[-1e-15] # set different diffusion values
D2=[-2e-15]
D3=[-3e-15]
t1=4/pi; # breaking the diffusion equation into smaller parts
time=135*60*60; # set time based on the experiments, in seconds
L=0.0005; # thickness in meters, average for grains
t2=((pi^2)*time)/(4*(L^2));
xdis=[0:0.000001:0.0005]; # diffusion profile along x
t4=pi.*xdis/(2*L);
t3=flip(t4);
distancex=[0:1:500]; # matching the xdis for better plotting

diffusion1=t1*(exp(D1*t2)*cos(t3)-(exp(D1*9*t2)*cos(3*t3)/3)+(exp(D1*25*t2)*cos(5*t3)/5)...
diffusion2=t1*(exp(D2*t2)*cos(t3)-(exp(D2*9*t2)*cos(3*t3)/3)+…
diffusion3=…
```

```
figure (1);subplot (2, 3, 4);
plot (distance, one_minus_AODdAODs, "+","markersize", 6);
hold on
plot(distance, AOHdAOH0, "o","markersize", 6);
plot(distancex,diffusion1, "k");
plot(distancex,diffusion2, "g");
plot(distancex,diffusion3, "b");
xlim ([0, 500]);
ylim ([0, 1.1]);
xlabel ("distance (micrometer)");
ylabel ("1-AOHd/AODs");
grid on;
hold off
```

Appendix D –Additional data and graphs

Appendix D1 - Trace elements table

All values are in μg/g. <L.D stands for limits of detection, where concentrations are below minimum possible detection.

	As	Ba	Be	Bi	Cd	Co	Cr	Cs	Cu	Ga	Ge	Hf	In	Mo
RayPic16 02	0.90	640	1.79	0.09	0.15	47.1	617	0.89	39.6	19.6	1.49	5.75	0.07	3.24
Mon	1.15	660	1.78	<L.D.	0.15	48.3	639	0.97	36.8	19.4	1.50	5.86	0.07	2.00
Col 2	1.27	662	1.86	<L.D.	0.14	48.4	711	0.95	38.1	20.3	1.55	5.94	0.07	4.32
Lep 4	1.53	650	1.77	<L.D.	0.15	52.2	691	0.90	37.9	20.1	1.49	6.00	0.07	6.07
Burz 16 06	1.20	651	1.77	<L.D.	0.14	48.8	603	0.94	35.5	19.9	1.51	6.01	0.07	3.02

	Nb	Ni	Pb	Rb	Sb	Sc	Sn	Sr	Ta	Th	U	V	W	Y	Zn
RayPic	81.7	347	4.13	59.2	0.11	22.39	2.27	816	5.77	6.53	1.73	182	1.12	25.9	112
Mon	80.7	355	4.08	56.8	0.10	21.27	2.07	844	5.84	6.79	1.68	181	<L.D.	26.2	116
Col	84.0	388	4.49	62.9	0.13	21.45	2.19	861	5.93	6.83	1.79	186	1.34	26.6	115
Lep	83.1	478	3.92	60.4	0.15	21.09	2.01	845	5.97	6.73	1.79	185	1.61	26.6	115
Burz	82.0	360	3.80	61.2	0.10	20.82	1.83	835	5.89	6.67	1.66	183	1.01	26.4	113

	Zr	La	Ce	Pr	Nd	Sm	Eu	Gd	Tb	Dy	Ho	Er	Tm	Yb	Lu
RayPic	273	53.2	100	11.4	44.1	8.51	2.67	7.03	0.975	5.51	1.00	2.46	0.334	2.04	0.295
Mon	278	54.5	103	11.7	44.9	8.68	2.68	7.11	0.984	5.51	1.02	2.46	0.337	2.03	0.290
Col	282	55.6	105	11.9	46.1	8.90	2.76	7.25	1.01	5.59	1.03	2.50	0.340	2.06	0.302
Lep	278	54.4	104	11.7	45.2	8.81	2.76	7.24	1.03	5.65	1.05	2.59	0.352	2.12	0.303
Burz	276	53.9	103	11.6	44.8	8.70	2.74	7.18	1.00	5.55	1.03	2.53	0.345	2.09	0.300

Appendix D1- Mineral proportion for figure 5.1

Sample	Ol	Opx	Cpx	Spl		Sample	Ol	Opx	Cpx	Spl
Pyro1	56	31	10	3		Level 1 06	57	33	7	3
Pyro2	46	36	14	4		Level 1 12	53	29	14	4
Pyro3	44	40	12	4		Level 2 03	73	22	4	1
Pyro4	53	38	6	3		Level 2 10	77	19	3	1
RayPic16 02	62	29	6	3		Level 3 02	92	4	2	2
RayPic16 04	58	32	8	2		Level 3 04a	42	42	12	4
Lep4	78	16	2	4						
Burz16 01	50	37	10	3						
Mon1	65	24	7	4						
Col2	58	32	7	3						

Appendix D2 – Average opx spectra

Average (n=10) opx spectra for sample Allègre Level 2 07 that was used in our experiments. Spectra derived from the four single crystals, before experiments and six crystals from the untreated cube slice. Axis x is wavenumber (cm^{-1}) and y axis is absorbance (cm^{-1}).

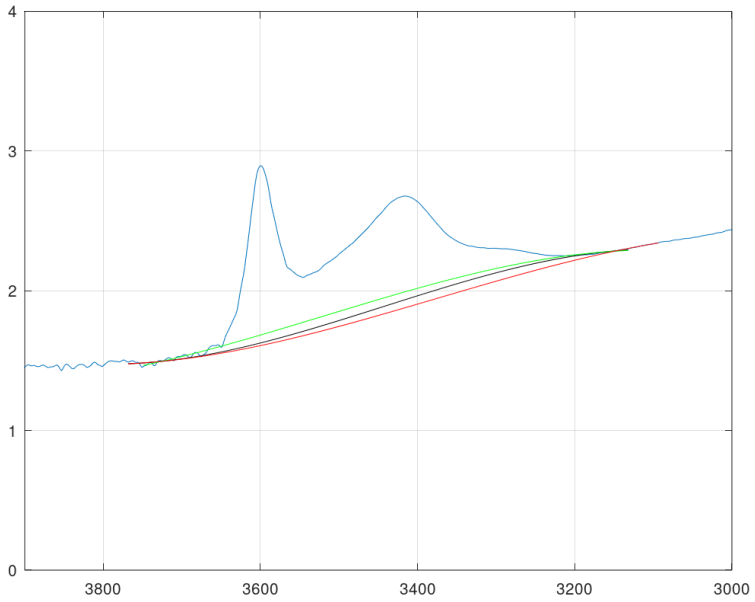

Appendix D3 – Additional graphs and data for single crystals

1) Top left corner graph shows the spectra with the polynomial fits of the baselines. 2) Middle top the integrated area. 3) Top right corner graph is the calculation of the value of b parameter representing the ratio of the two extinction coefficients of OH bands and OD bands. 4) Second row left corner is the fit of the diffusion coefficient from equation 2.6. 5) Second row middle is the check that no hydrous species were lost during H/D exchange (A_{OH} + b*A_{OD} = constant). 6) Third row, the photo of the opx crystal. In the single crystals presented below, we follow the same graph order.

Opx1 700°C 108h

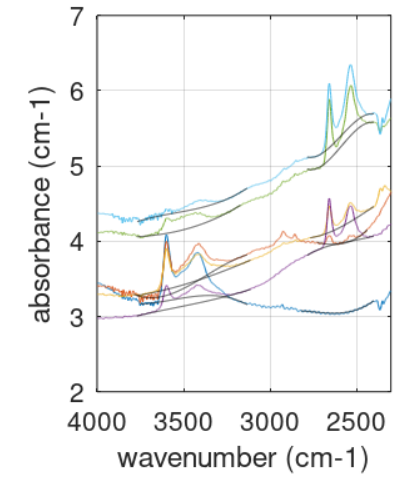

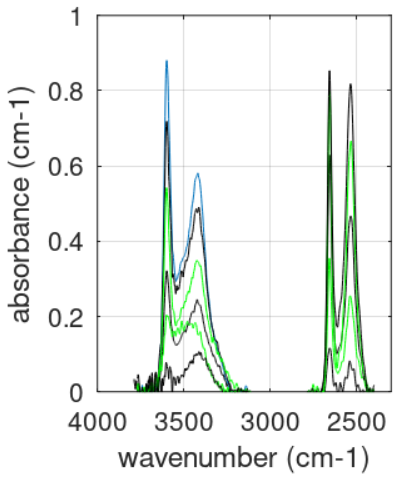

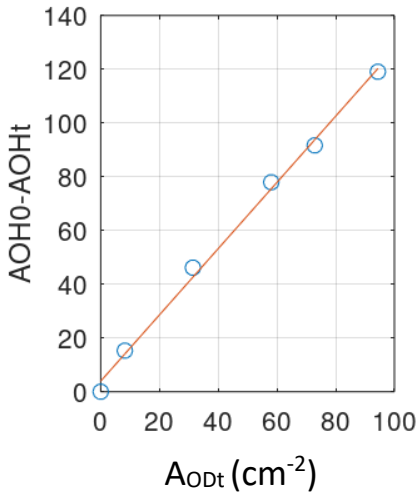

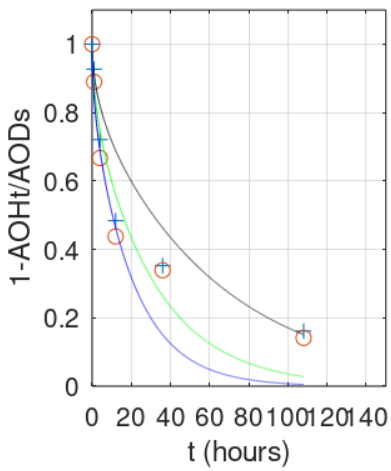

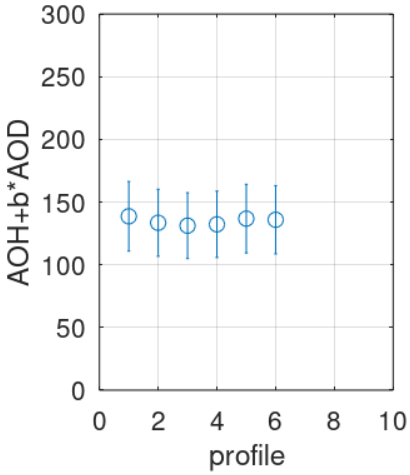

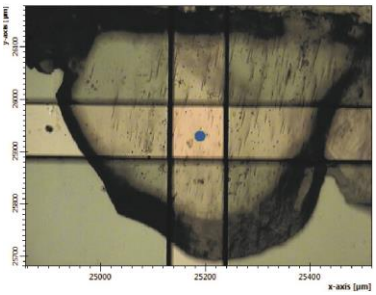

Opx5 800ºC 16h

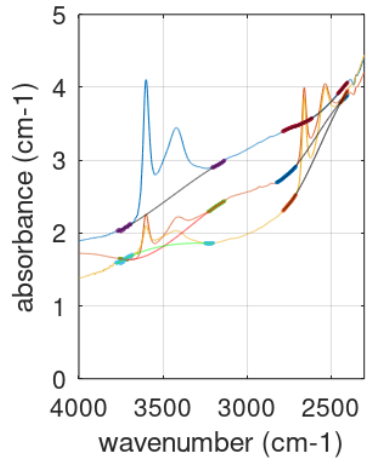

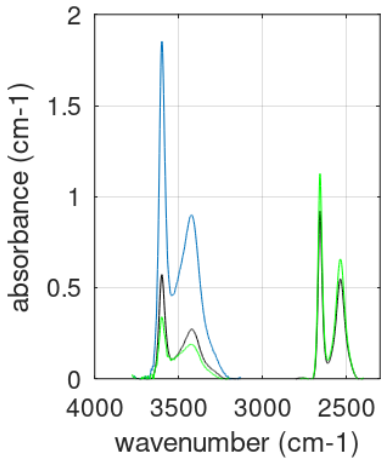

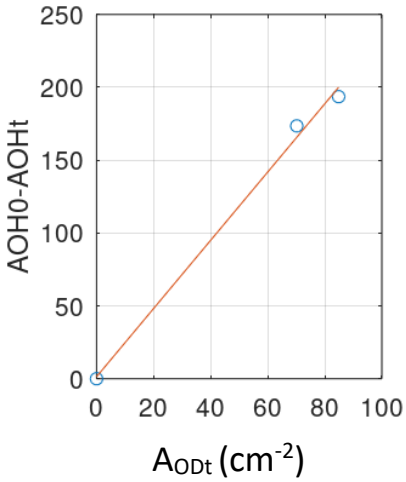

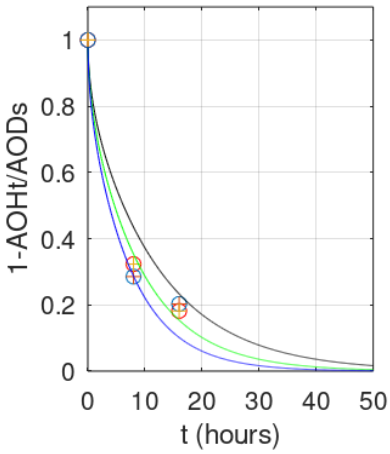

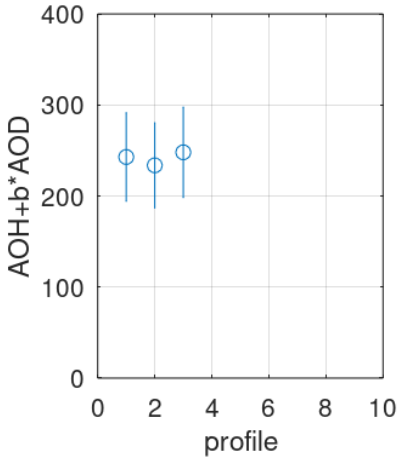

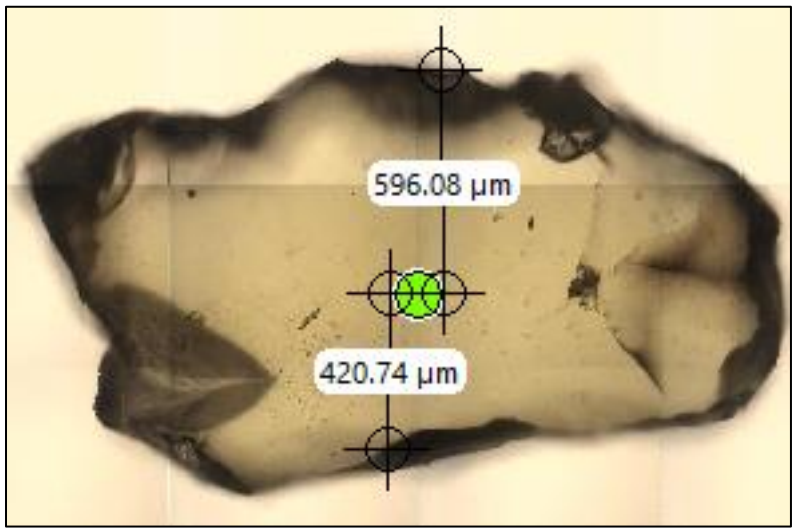

Opx2 800ºC 5h

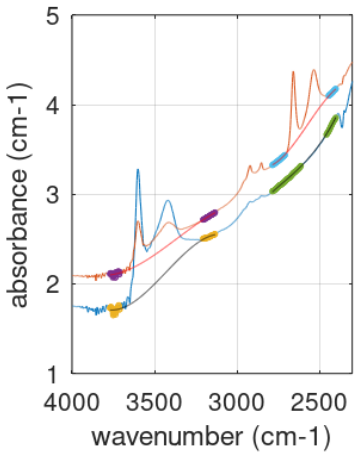

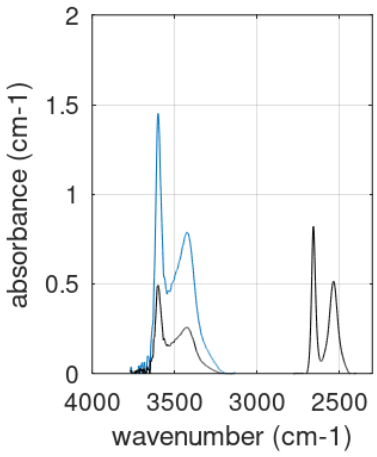

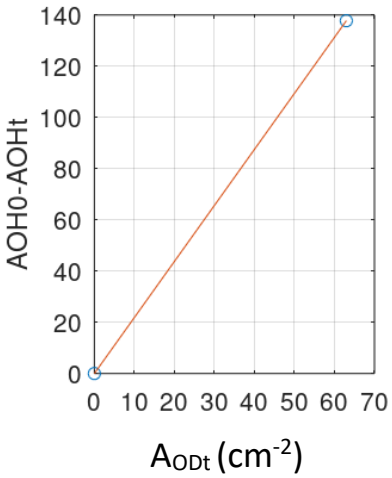

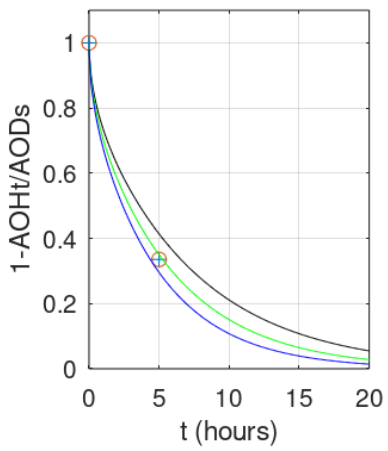

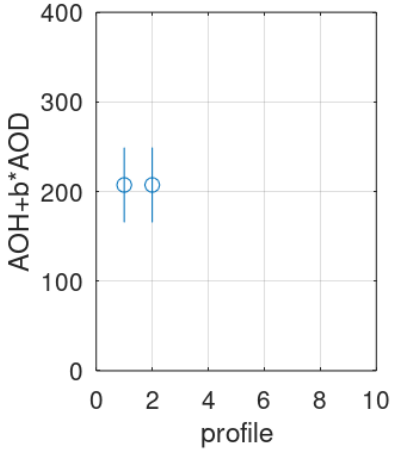

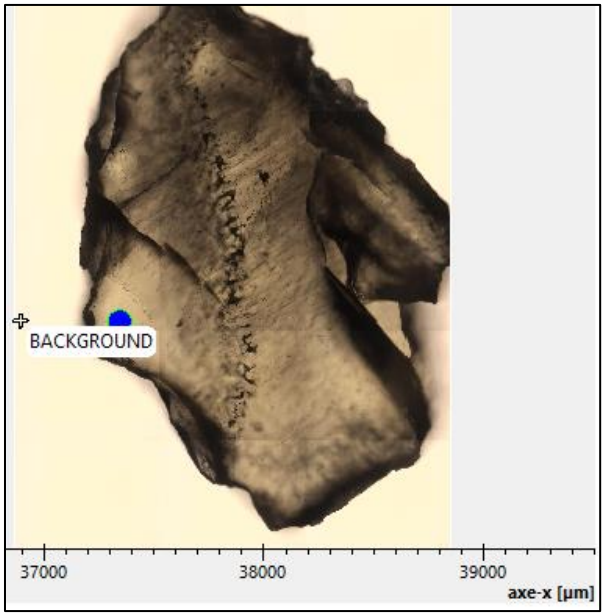

Opx3 900ºC 4h

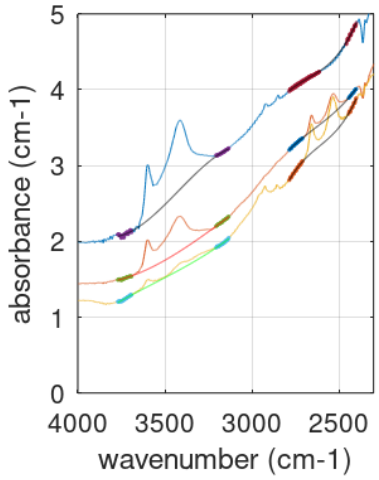

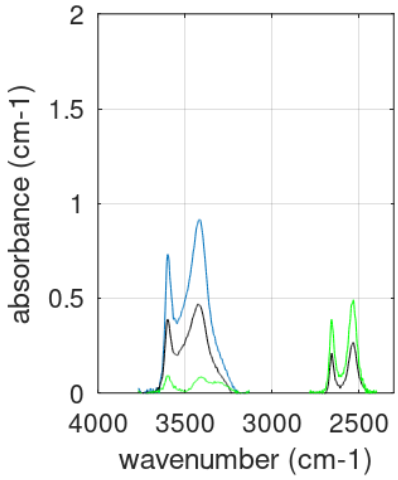

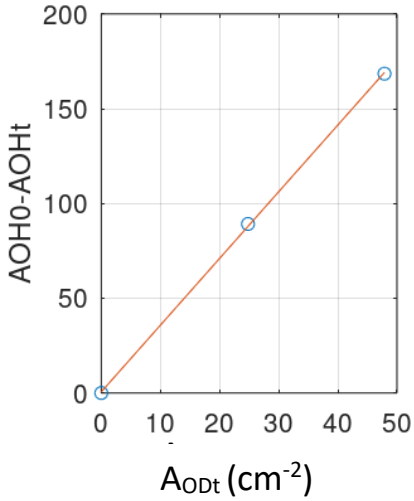

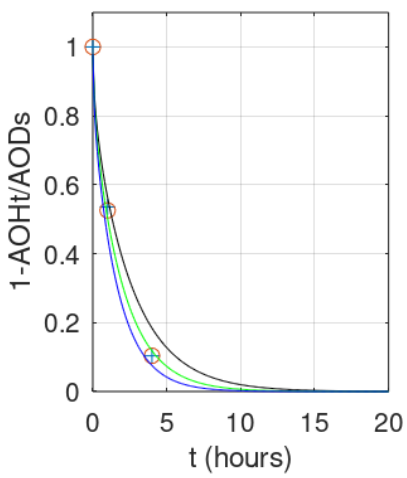

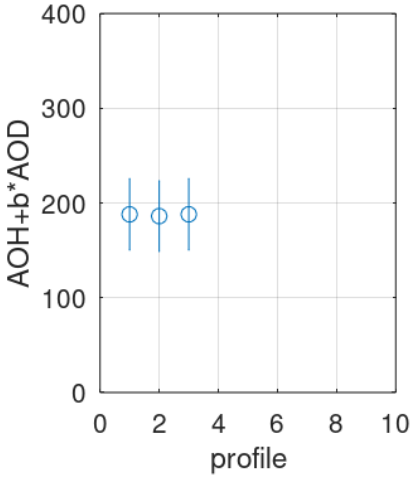

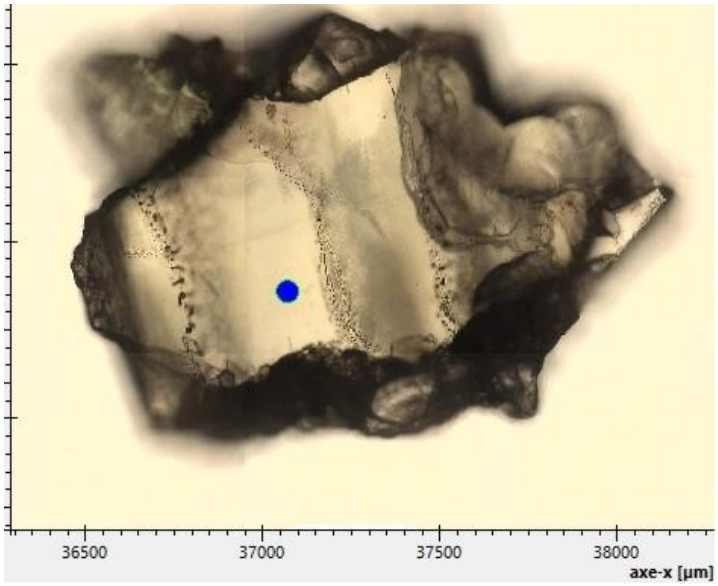

Appendix D4 – Additional graphs and data for crystals at the cubes edges

1) Top left corner graph shows the spectra with the polynomial fits of the baselines. 2) Middle top the integrated area. 3) Top right corner graph is the calculation of the value of b parameter representing the ratio of the two extinction coefficients of OH bands and OD bands. 4) Second row left corner is the fit of the diffusion coefficient from equation 2.7. 5) Second row middle is the check that no hydrous species were lost during H/D exchange (A_{OH} + b*A_{OD} = constant). 6) Third row, the photo of the opx crystal with the profile. In the crystals presented below, we follow the same graph order.

600ºC 5b 4a edge 135h

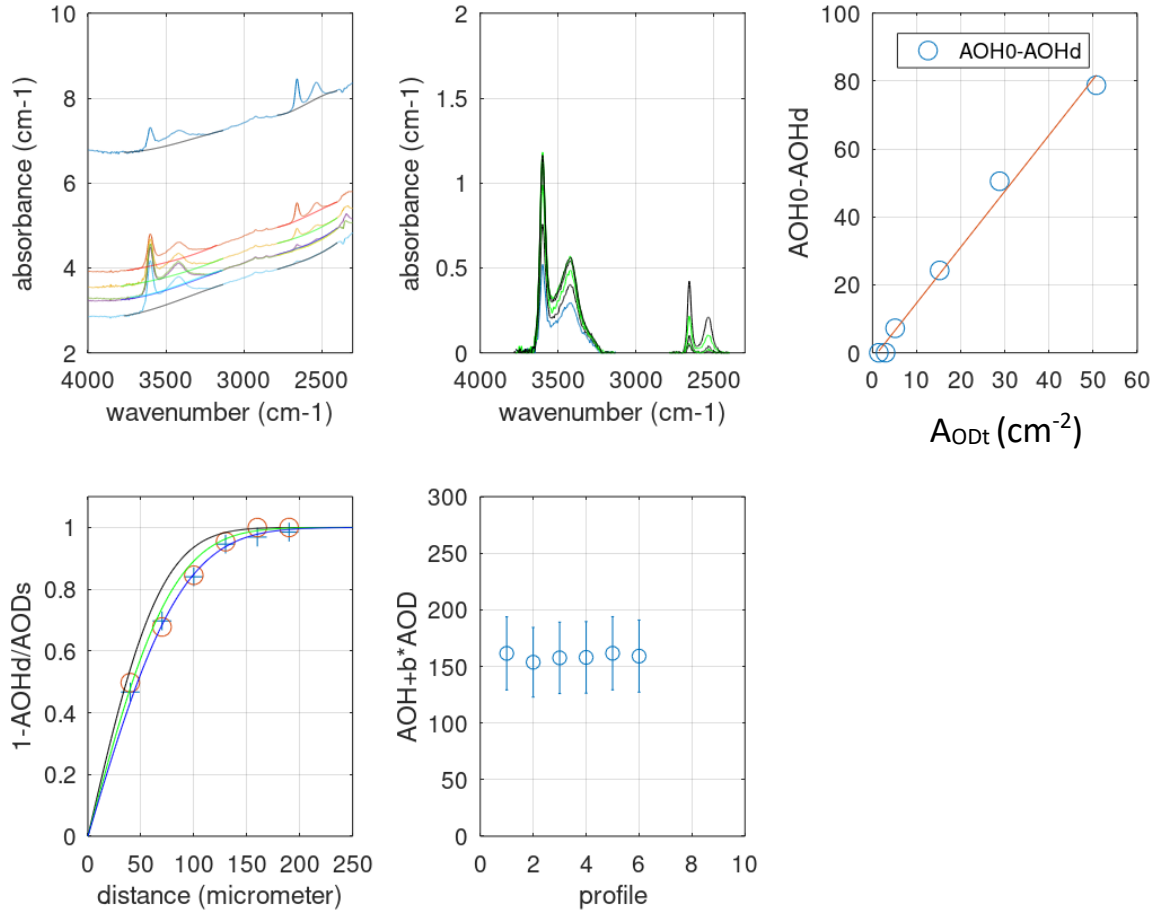

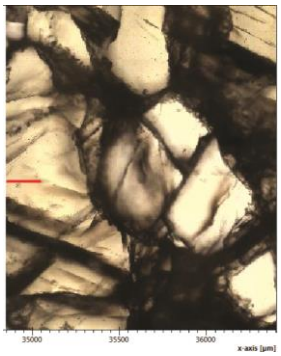

600°C 5b 10γ edge 135h

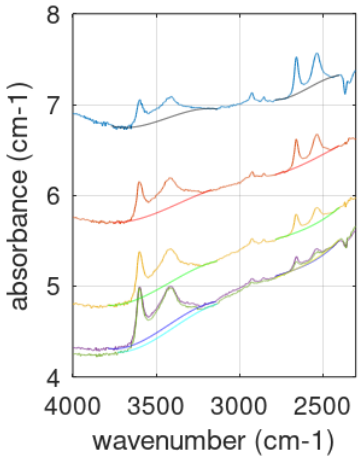

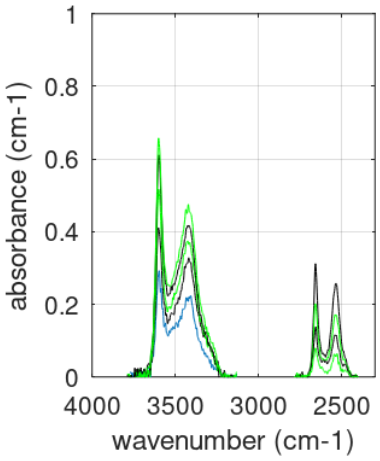

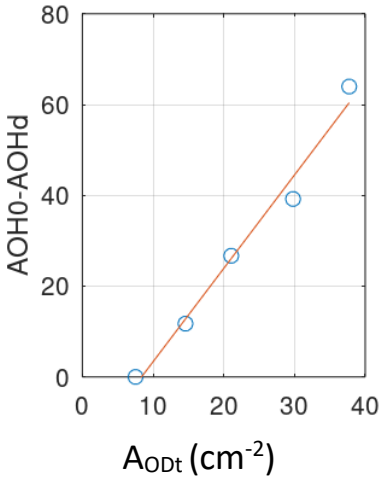

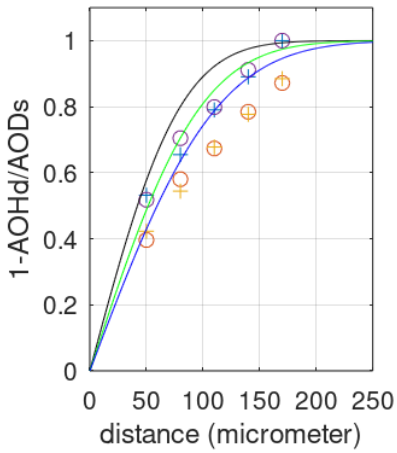

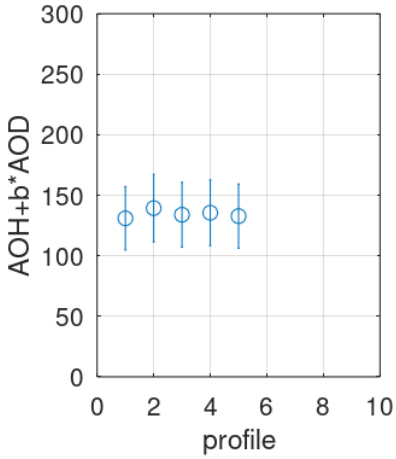

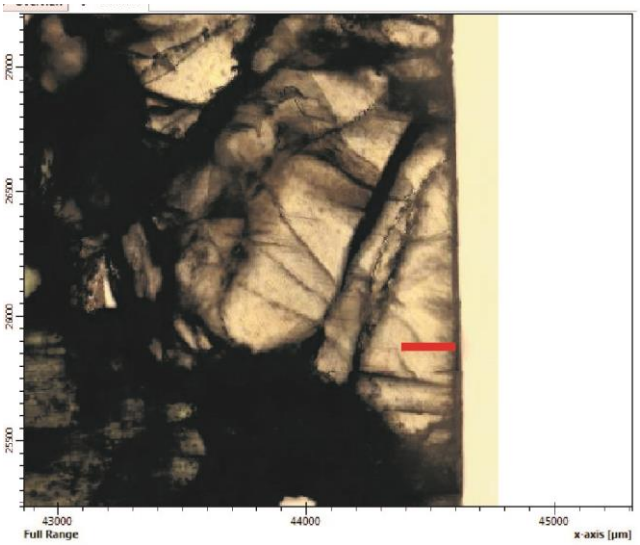

700ºC 5ac 3α edge 108h

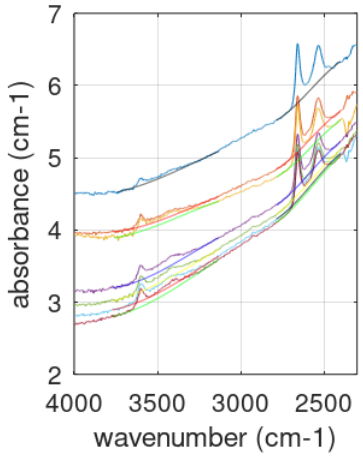

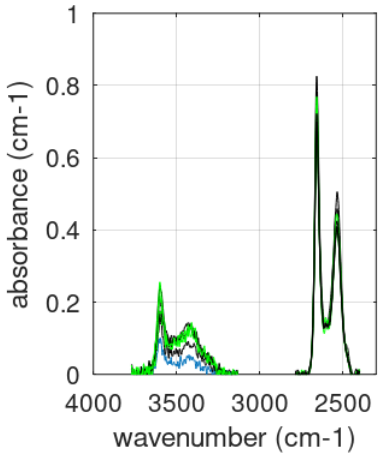

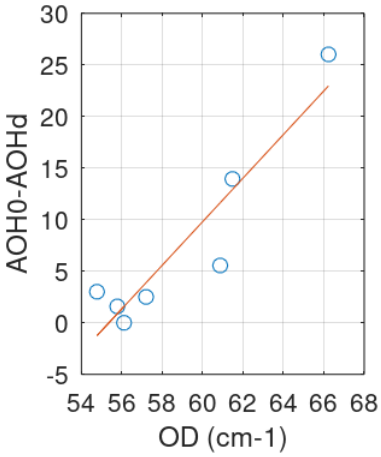

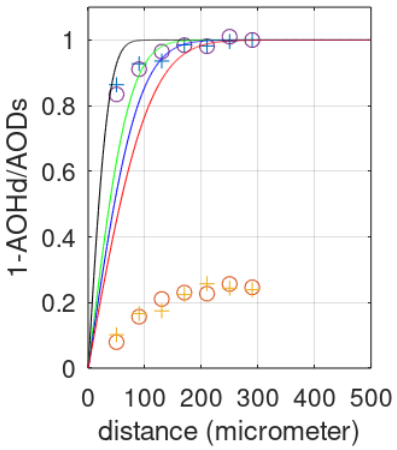

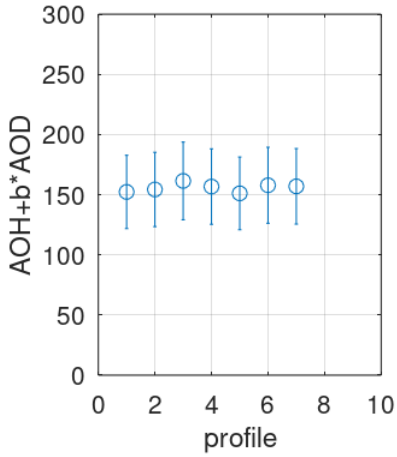

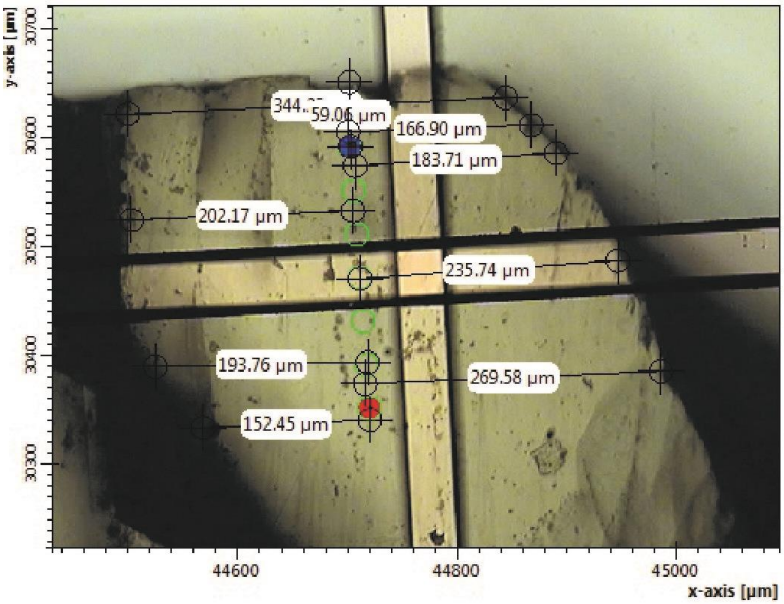

900ºC 6b2 3α edge 4h

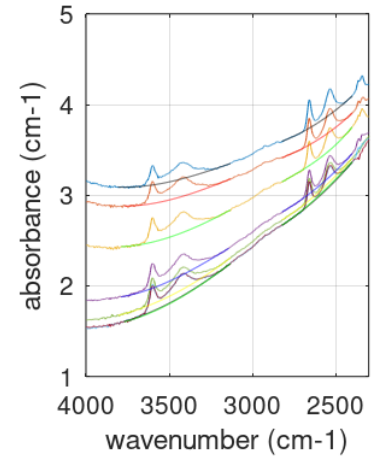

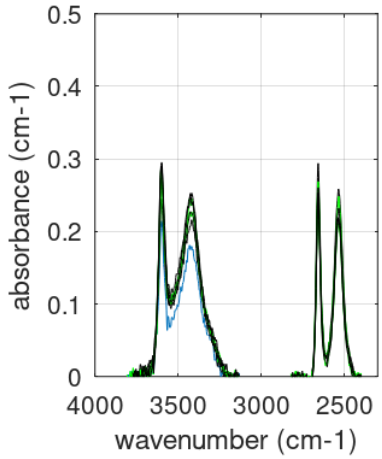

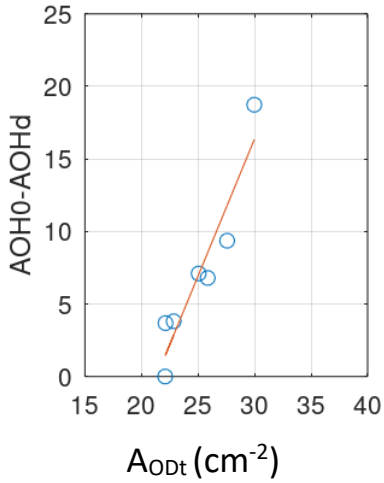

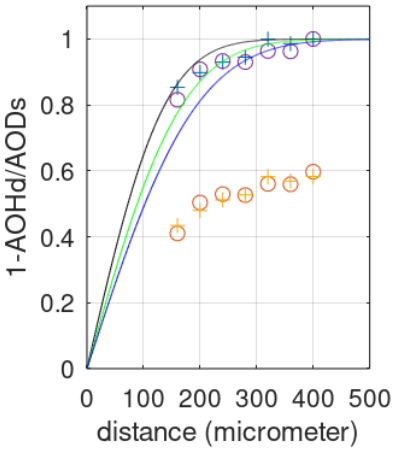

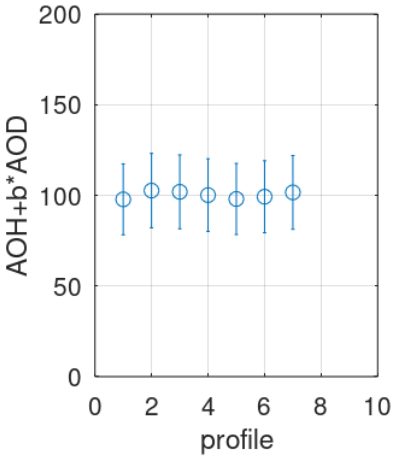

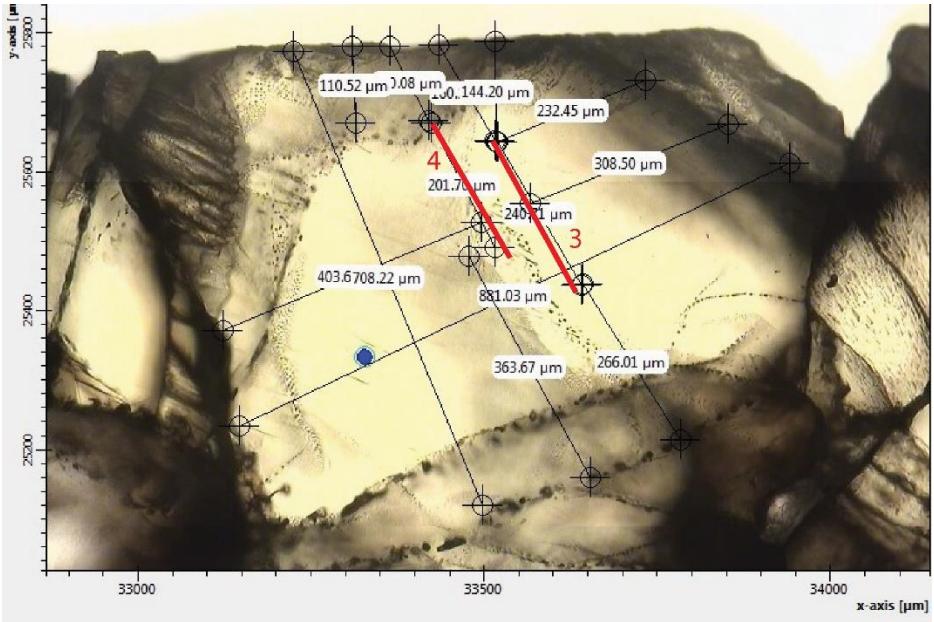

900ºC 6b2 4α edge 4h

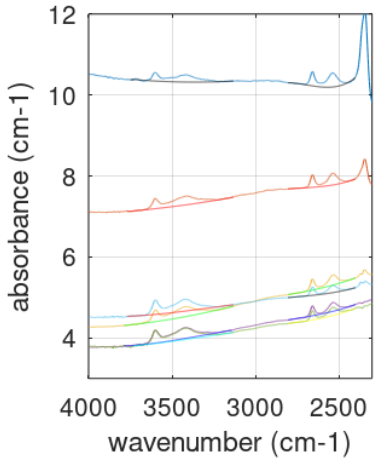

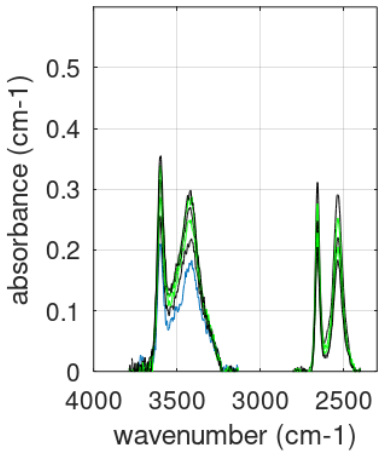

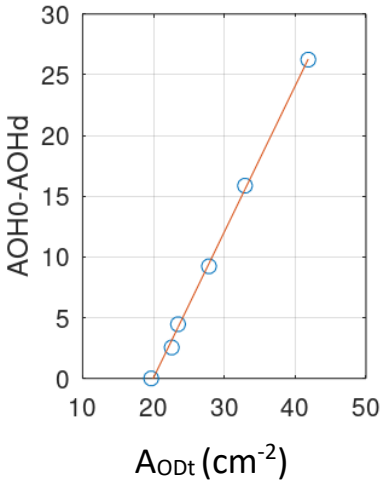

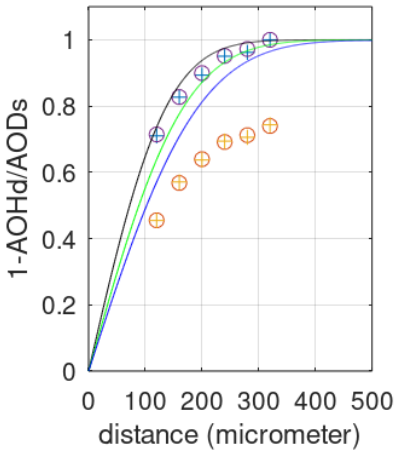

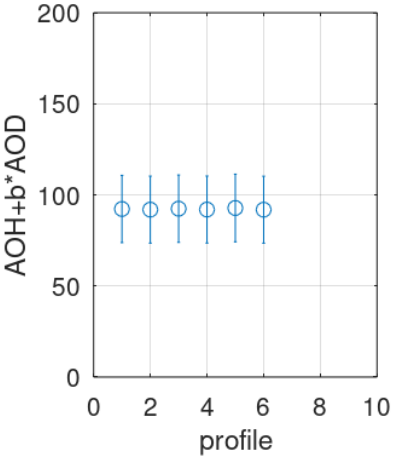

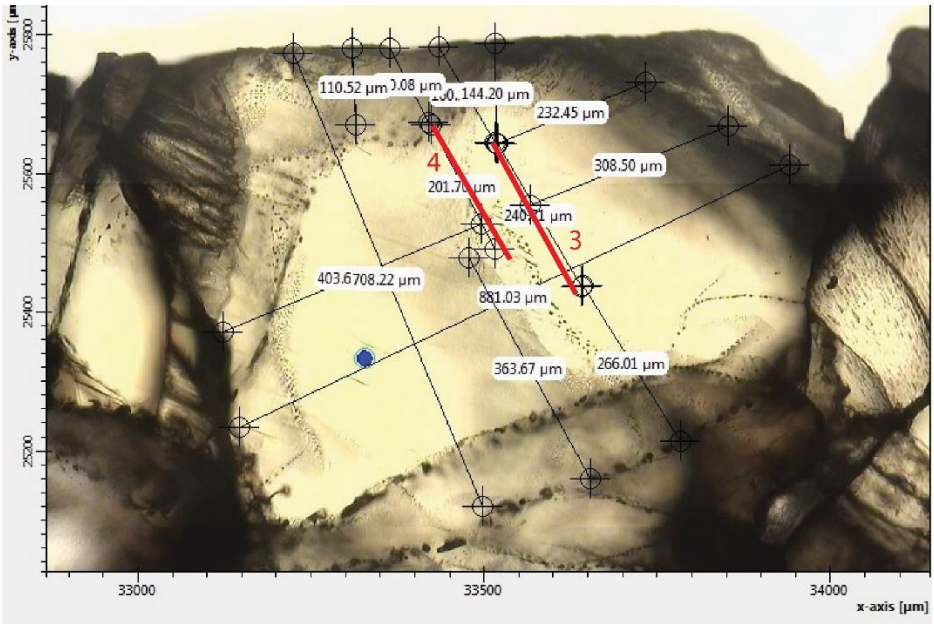

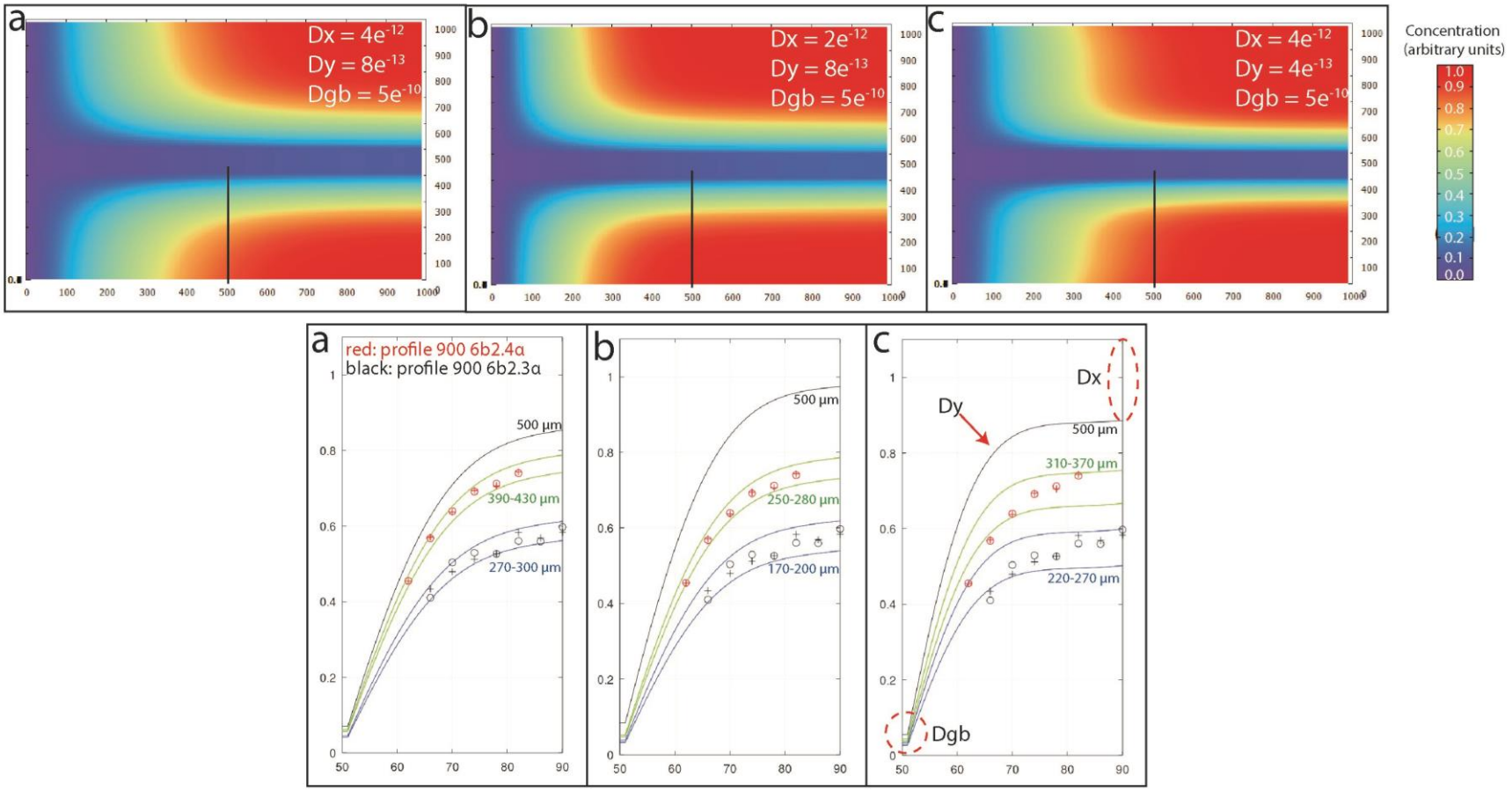

Illustrative diagram showing the process with the numerical modelling for finding profiles diffusion coefficient and their possible contribution from lateral diffusion. The example is for profiles at 900ºC 6b2 3 and 4. We perform few dozens of these kind of modelling tests in order to find the range within our profiles fit better. The three main parameters Dx, Dy and Dgb are affecting three different areas in the profiles. Dgb controls mainly the grain boundary saturation and the Cgb in the end of the modelling, with fast Dgb leading to values close to Cgb = 0. Dx is controlling the rate of the contribution from the lateral diffusion with faster values leading to lower plateaus. Dy is controlling the curve of the profile with faster values leading to more sharp profiles. We can see the differences in the three examples. Example c is just for showing a bad profile that does not fit with our data.

Appendix D5 – Additional graphs and data for crystals inside the cubes

600ºC 5b 2α inside 0.7mm 135h

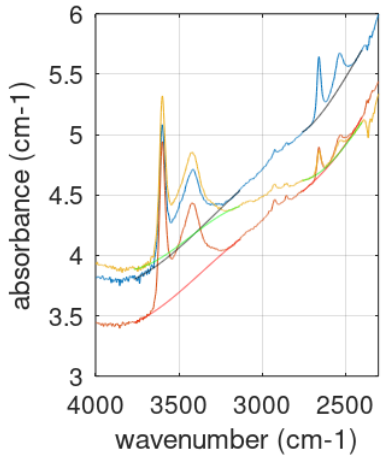

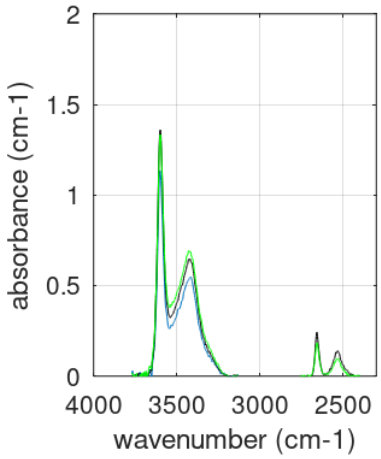

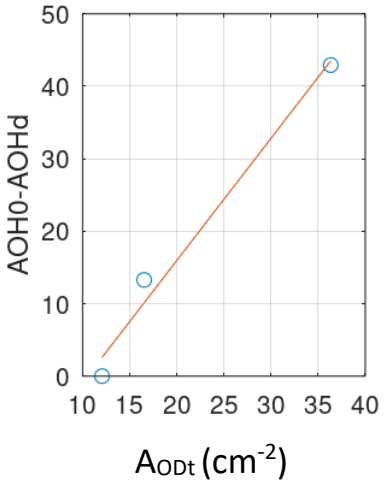

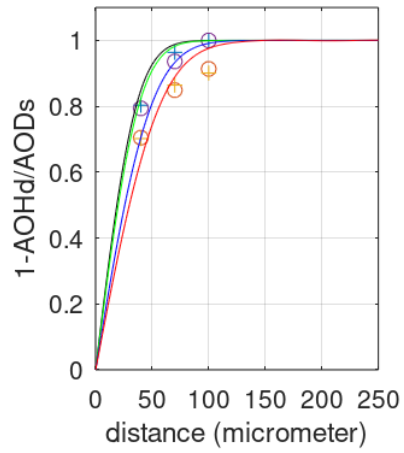

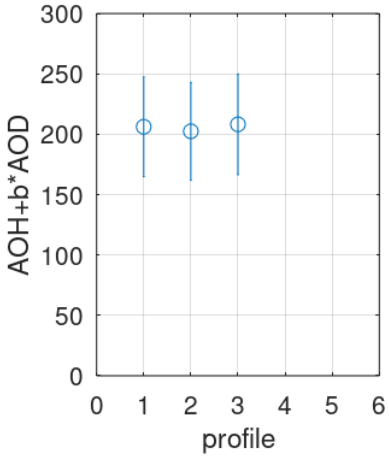

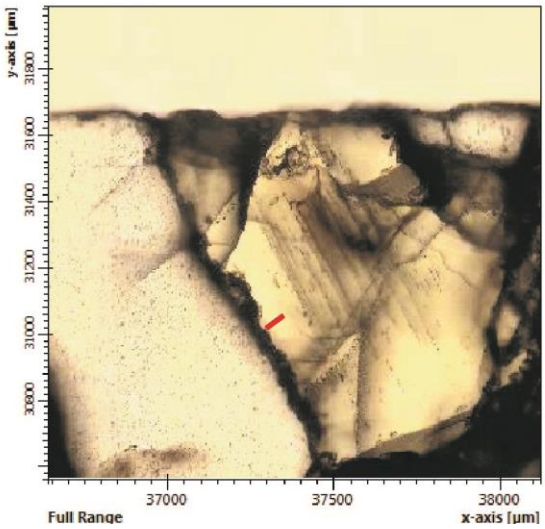

600°C 5b 8γ inside 1.7mm 135h

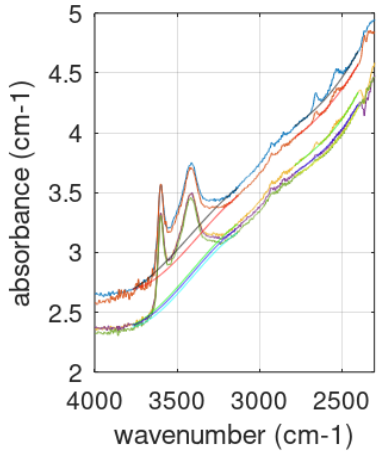

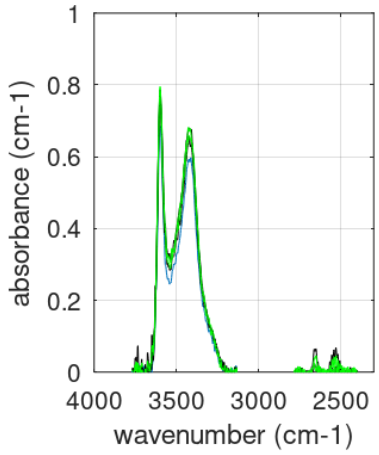

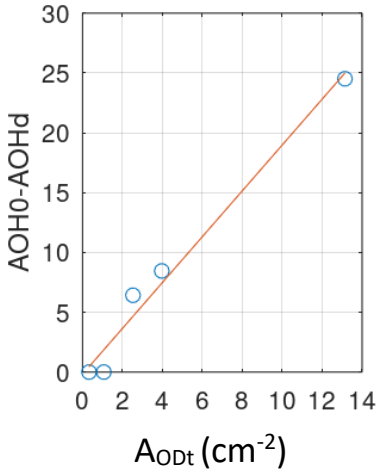

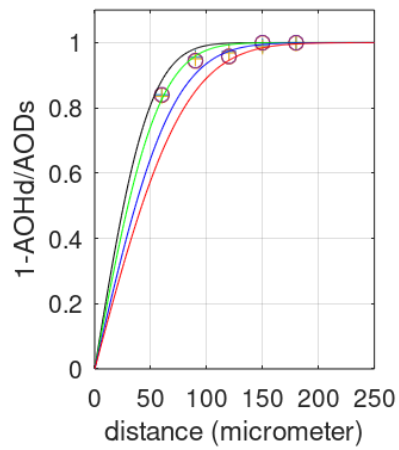

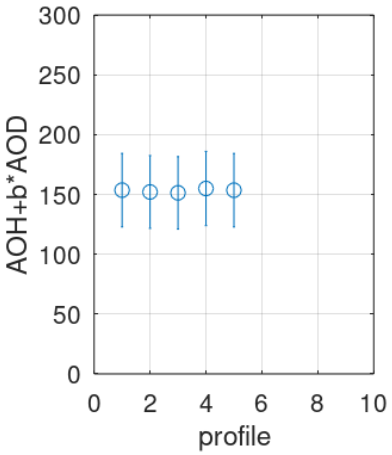

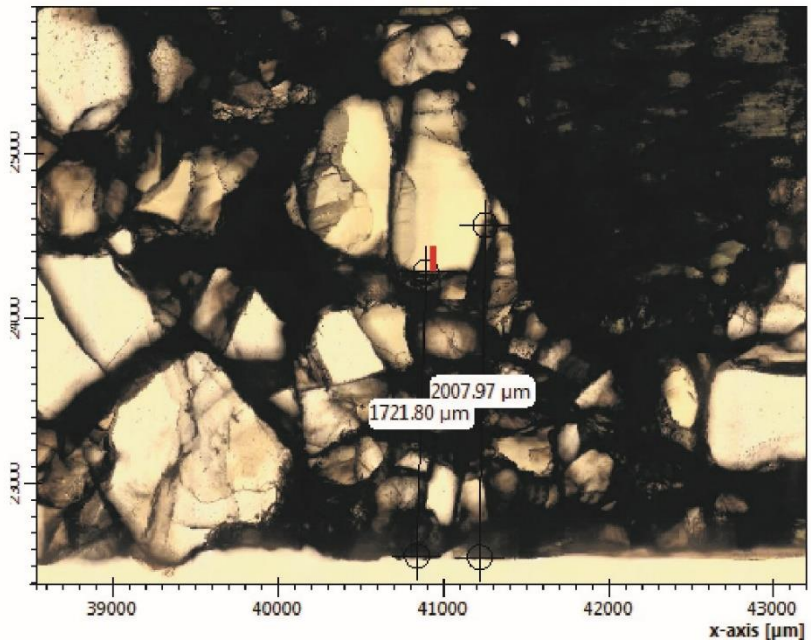

600ºC 5bb 2γ inside 1.3mm 135h

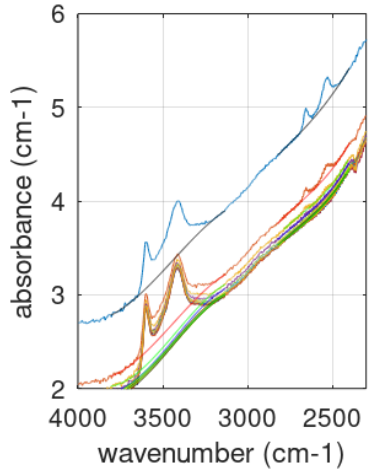

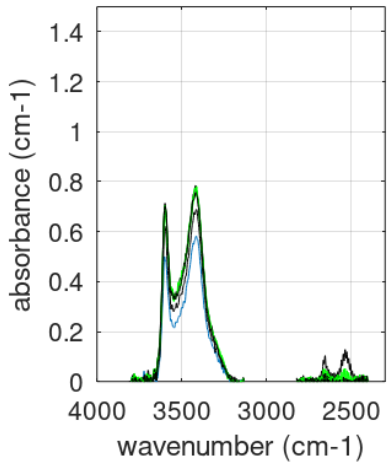

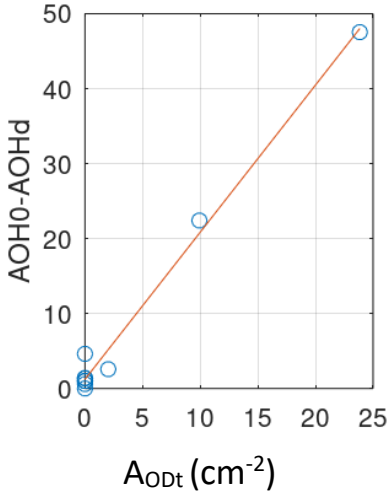

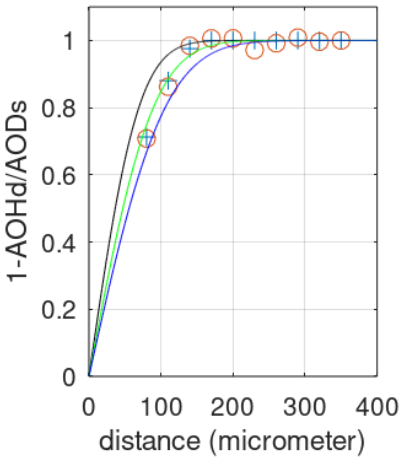

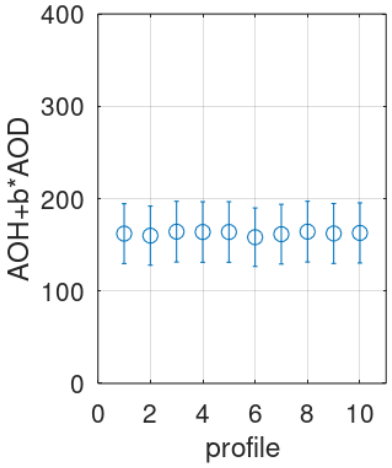

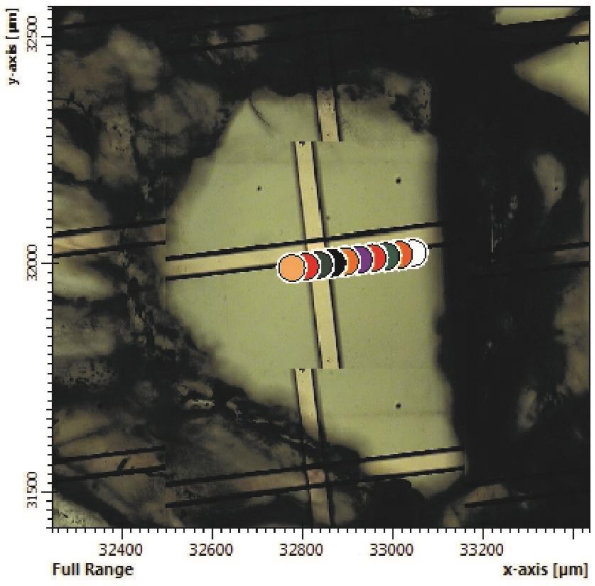

600ºC 5bb 6α inside 1.0mm 135h

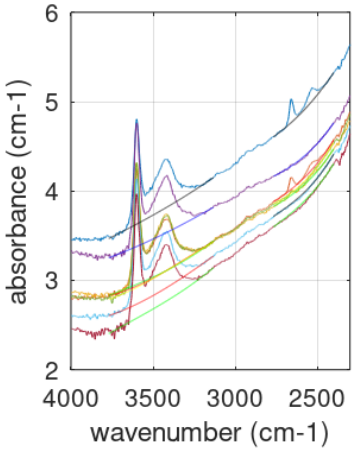

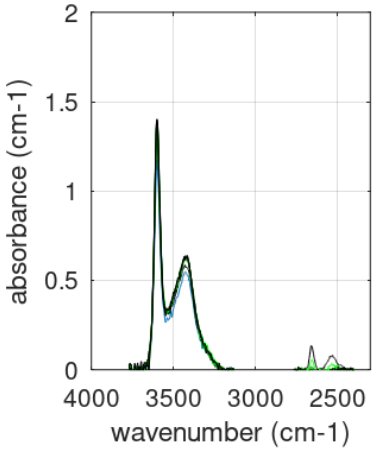

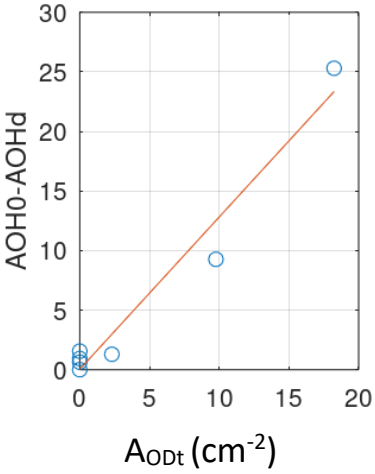

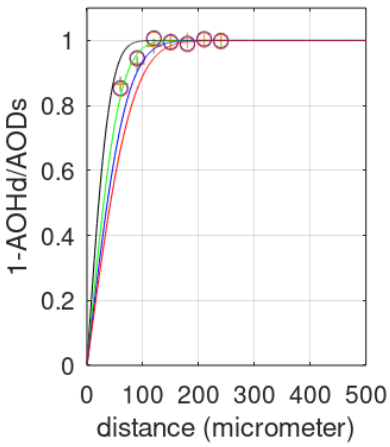

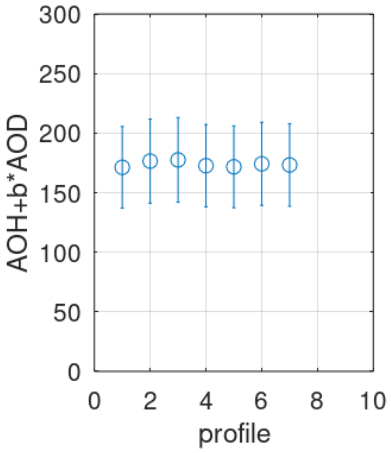

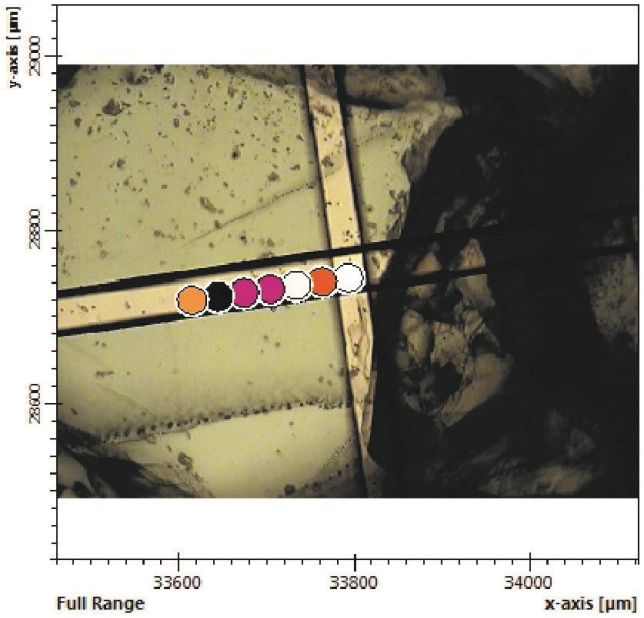

700ºC 5ac 5γ inside 0.5mm 108h

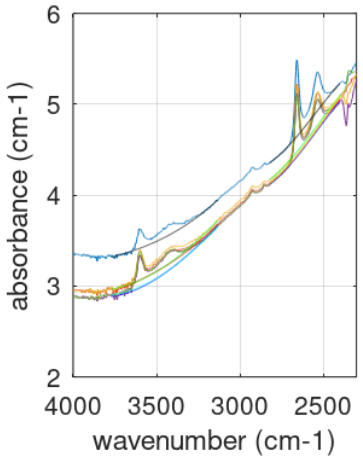

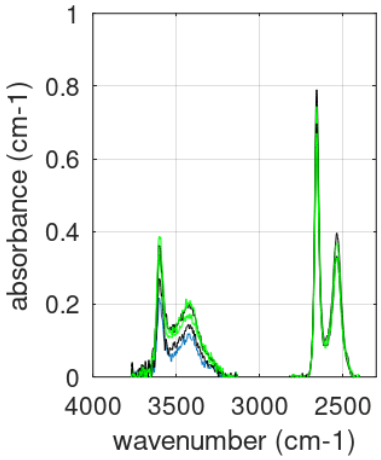

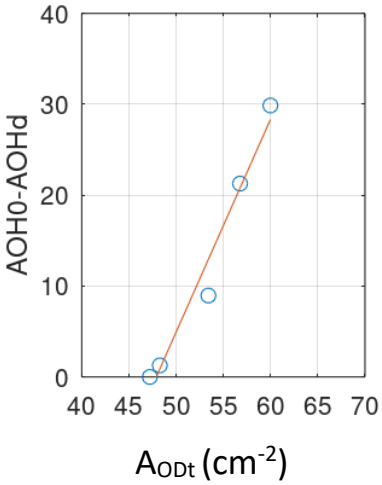

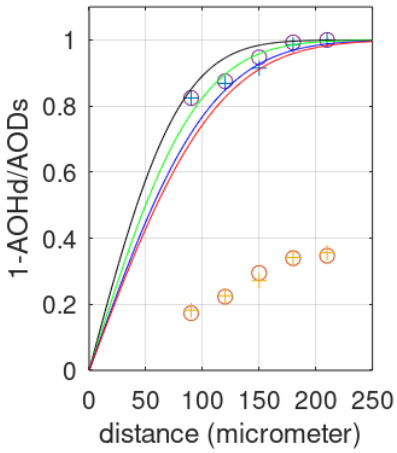

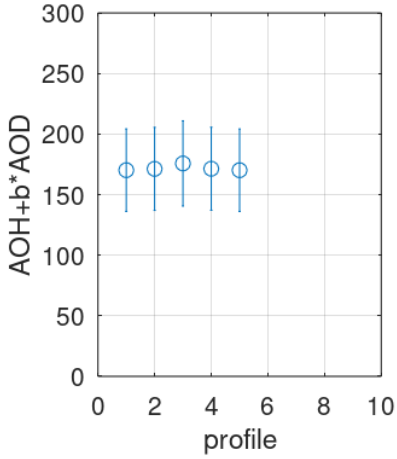

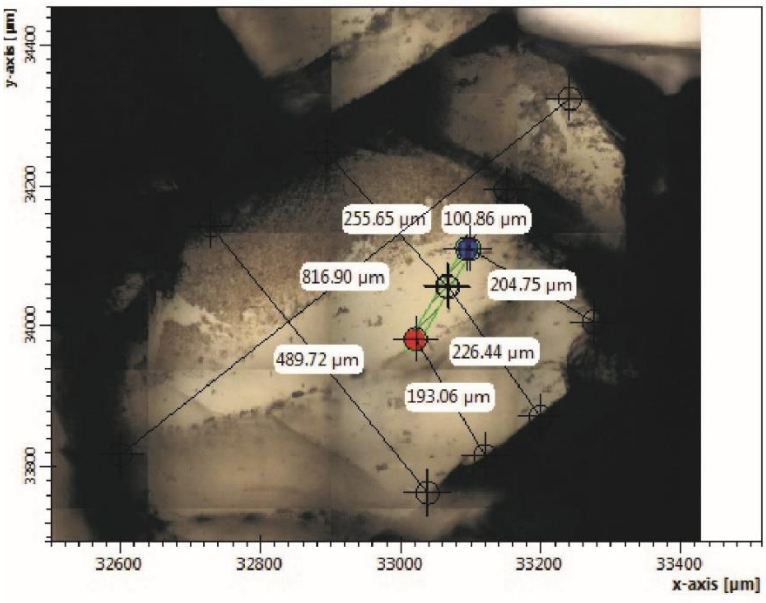

700°C 5aii 0γ inside 2.3mm 108h

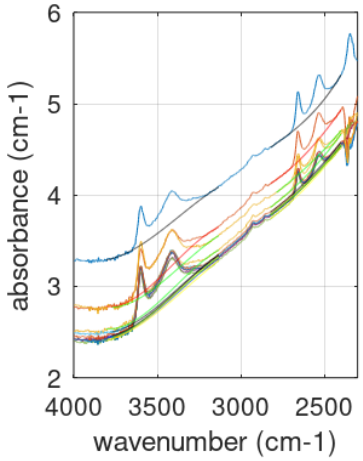

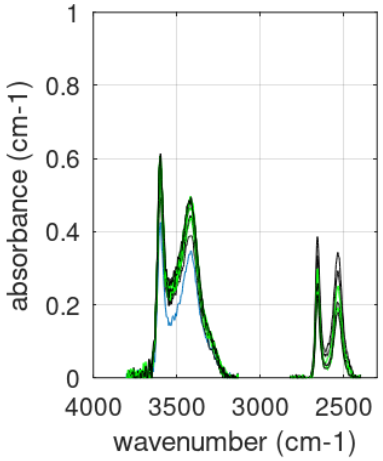

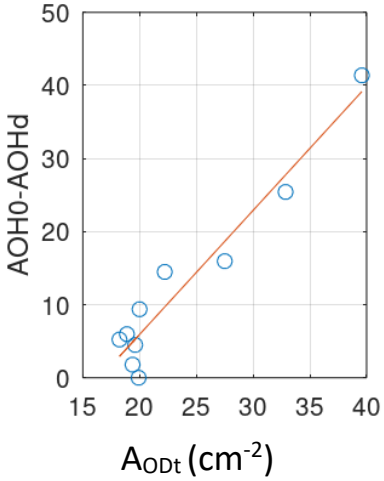

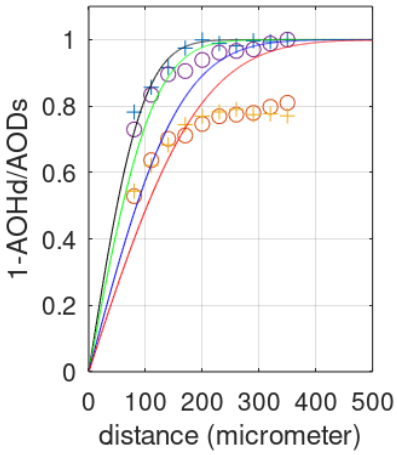

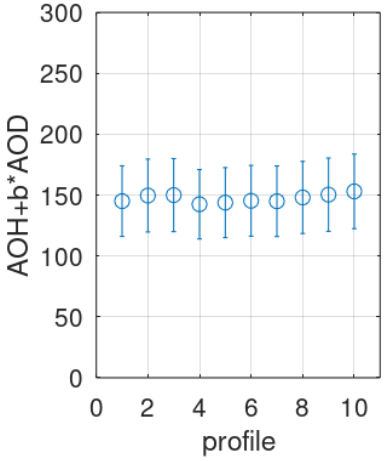

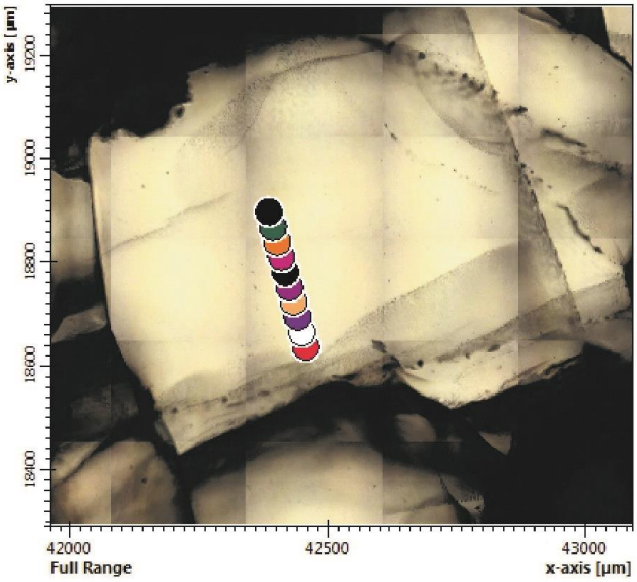

800°C 7b 1γ inside 0.5mm 16h

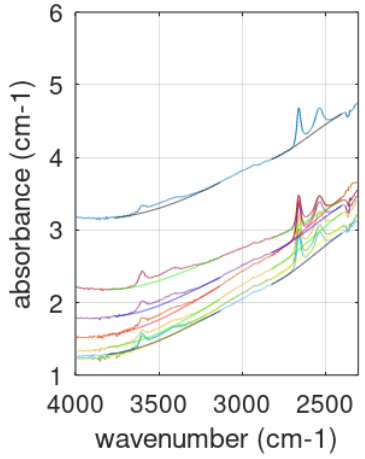

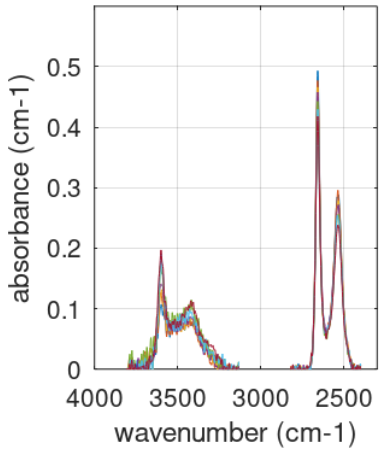

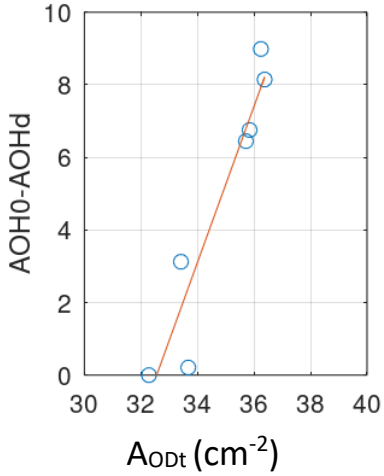

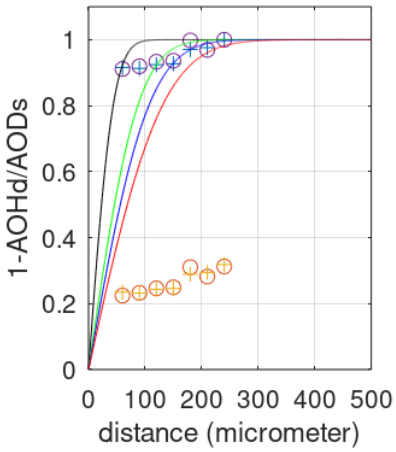

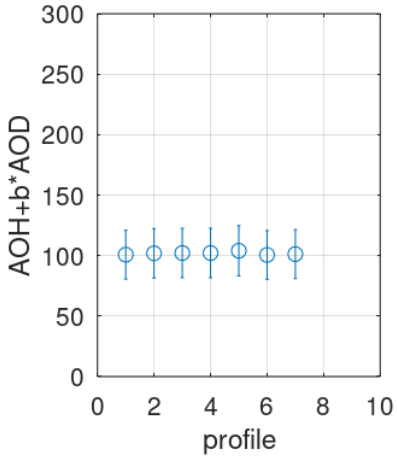

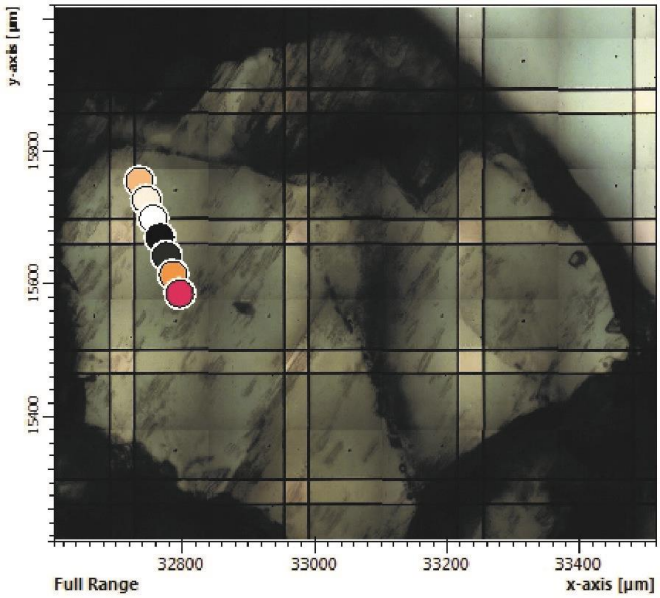

800°C 7b 5γ inside 2.8mm 16h

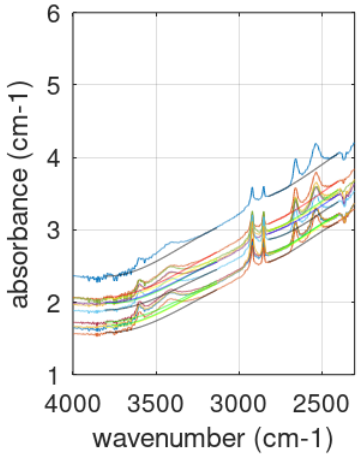

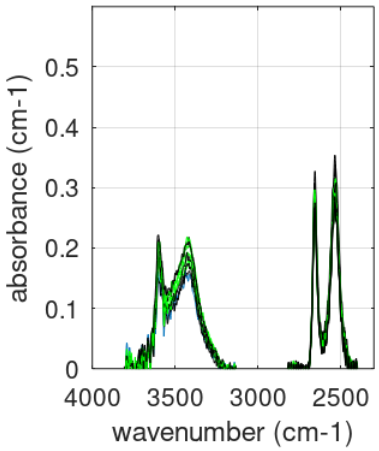

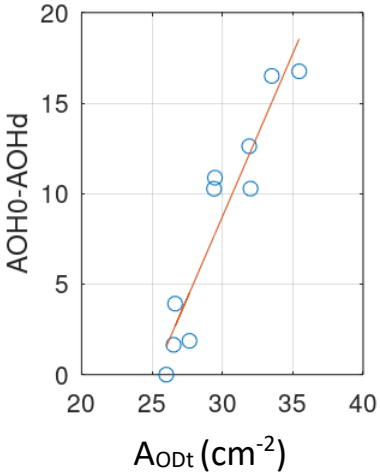

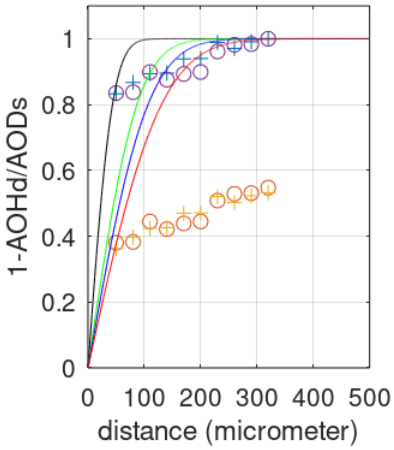

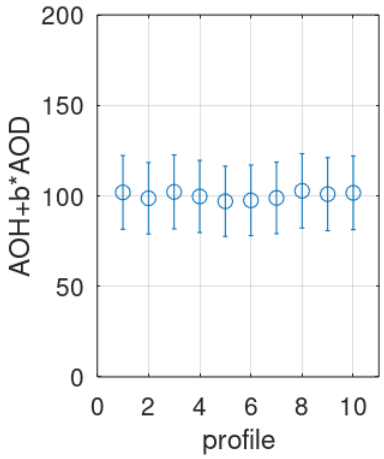

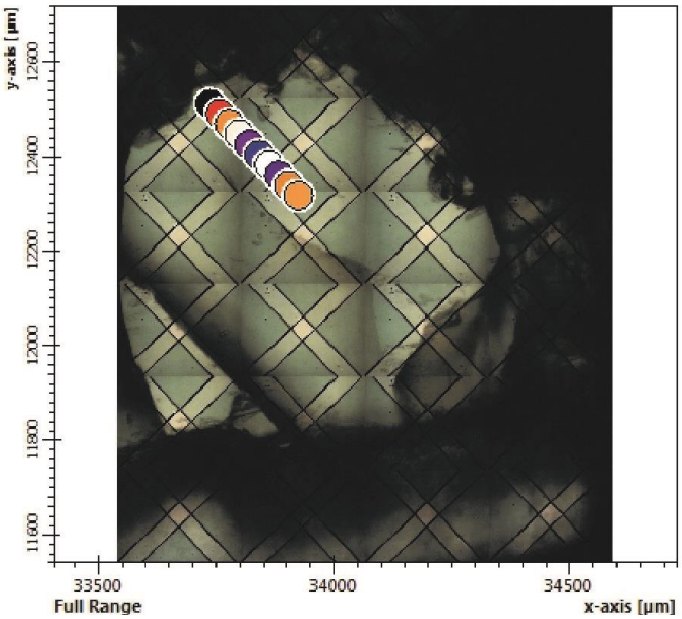

800°C 7b2 3γ inside 1.6mm 16h

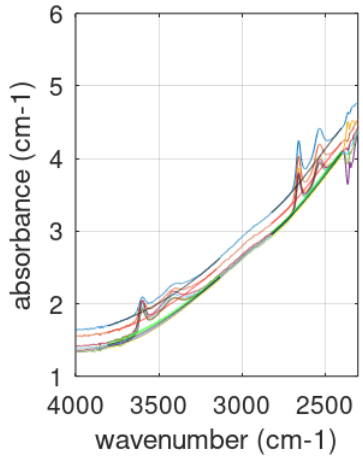

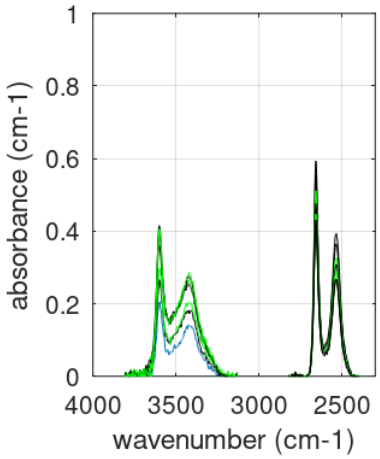

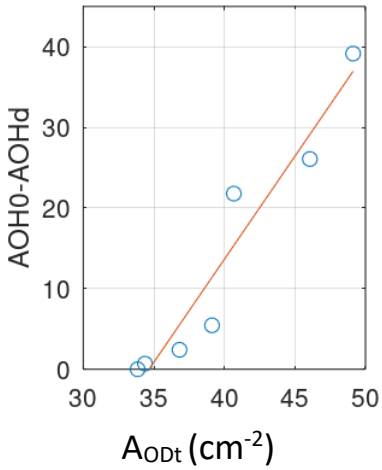

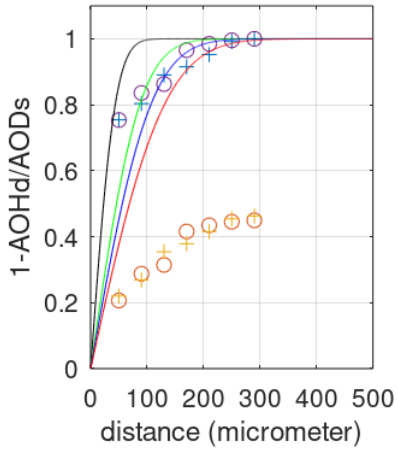

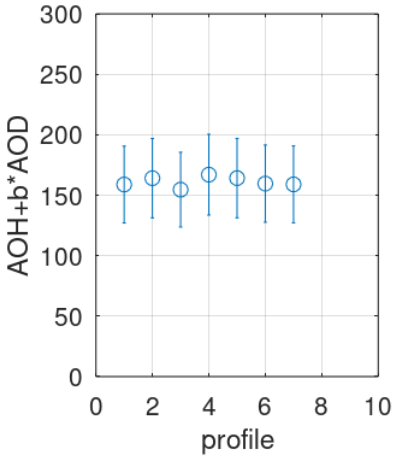

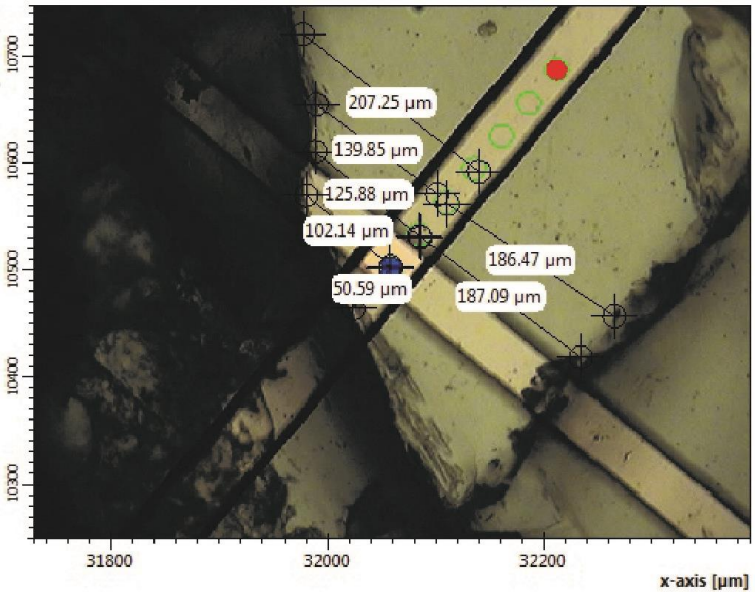

800°C 7b2 7γ inside 2.2mm 16h

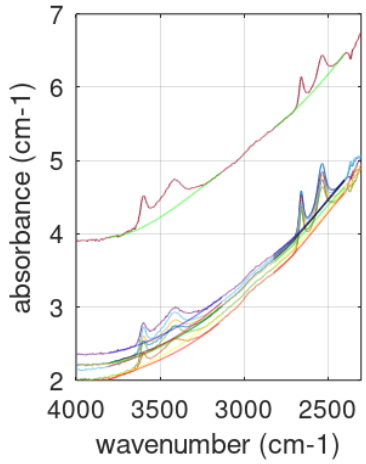

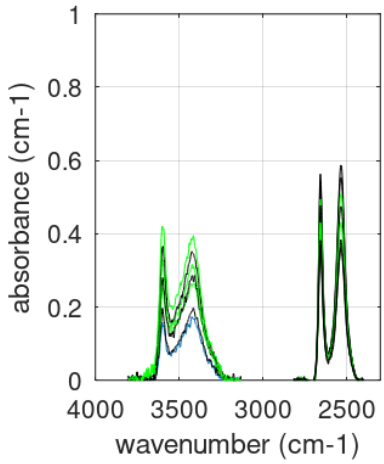

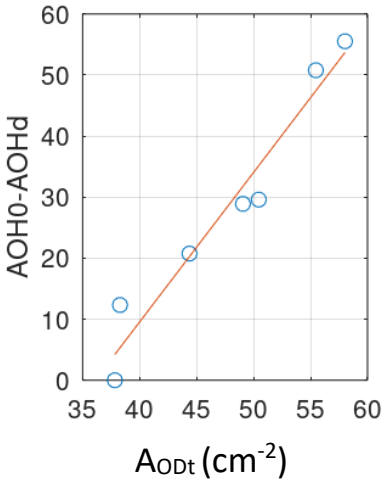

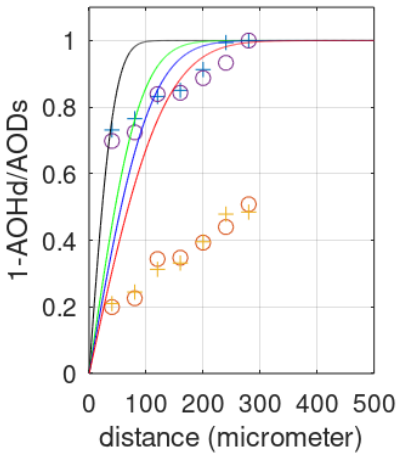

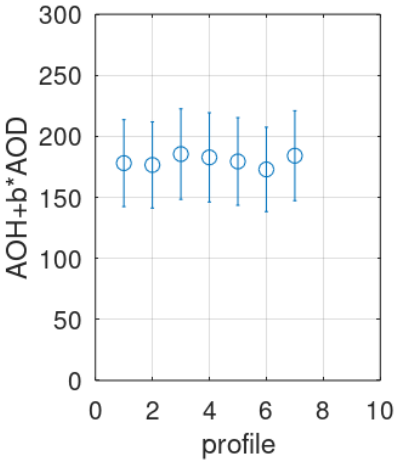

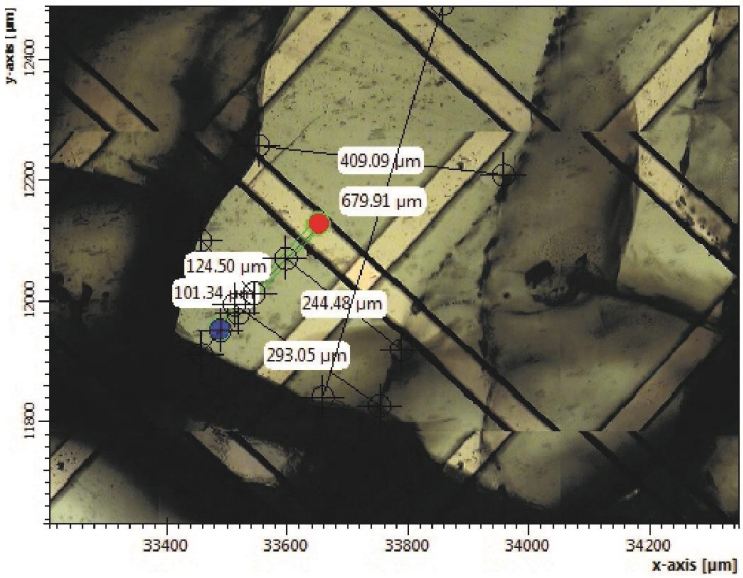

900°C 6b2 9α inside 3.0mm 4h

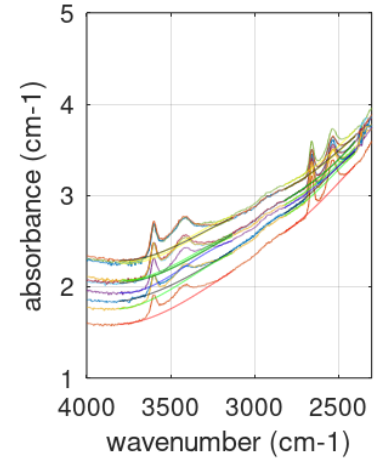

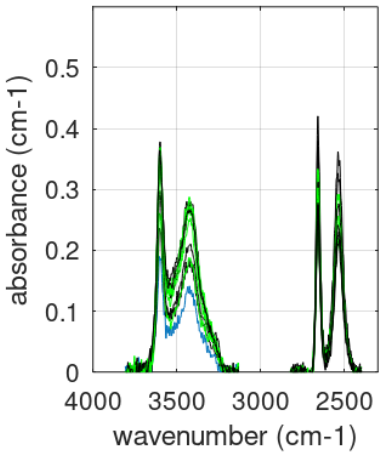

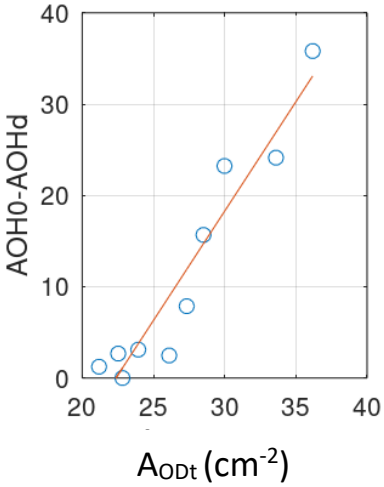

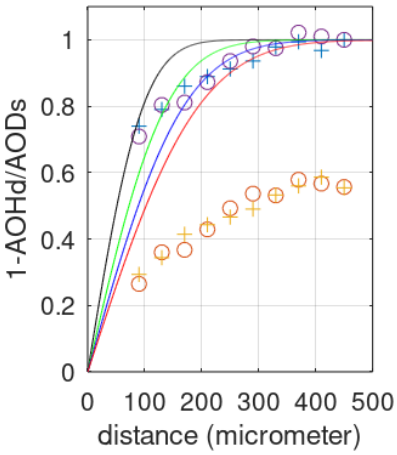

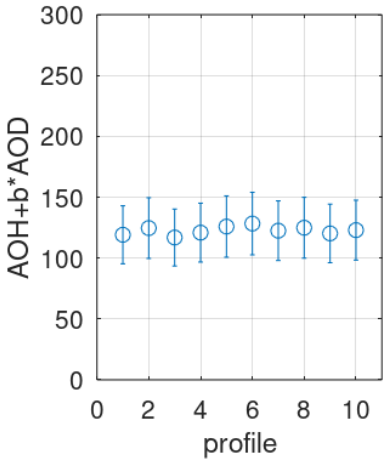

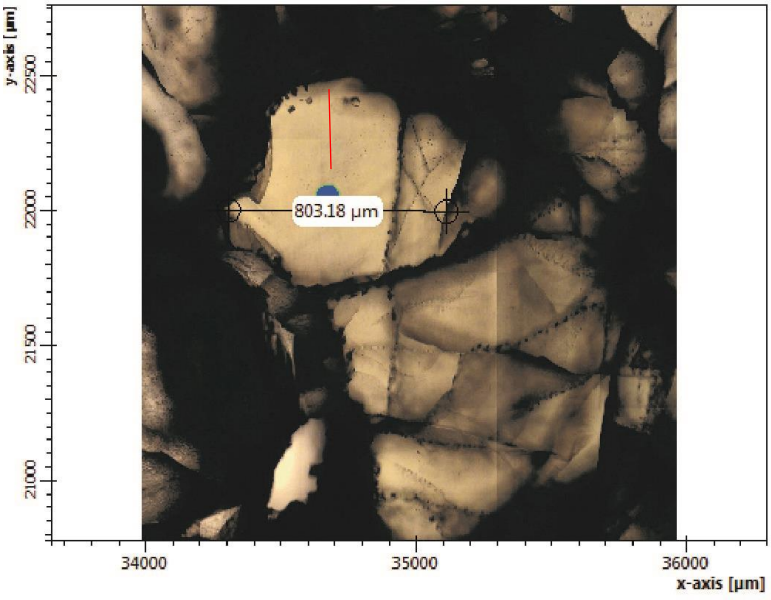

900°C 6c 7γ inside 2.4mm 2h

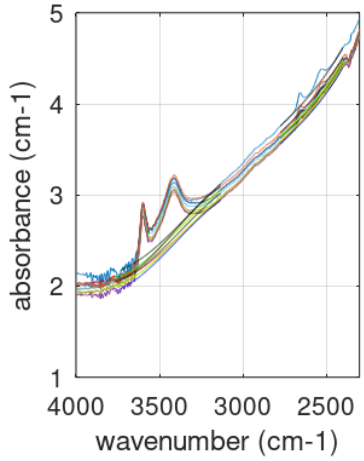

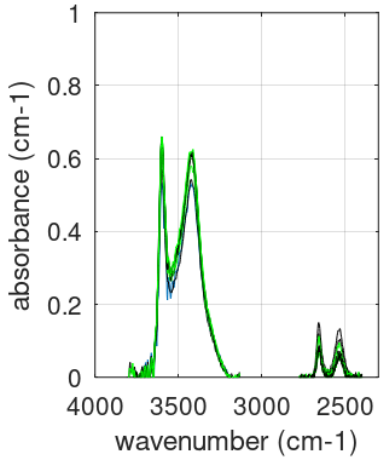

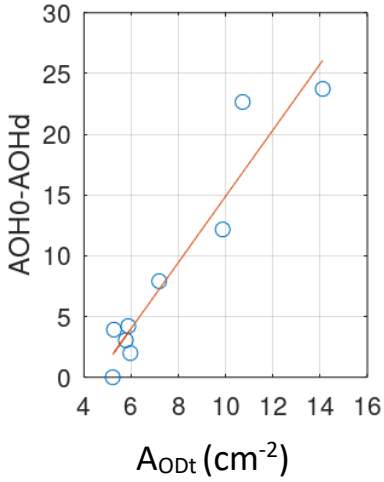

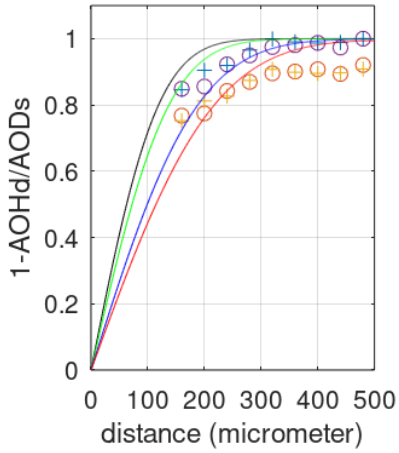

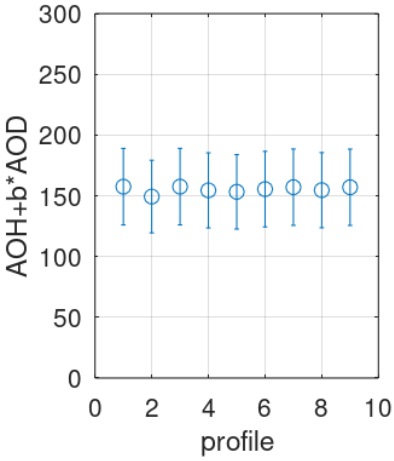

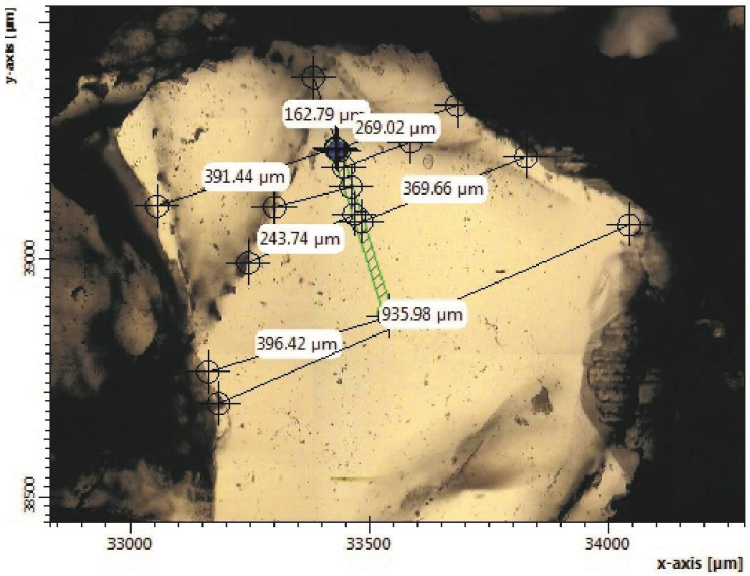

Appendix D6 – Cube maps

5b

All well-structured sides of the cube maps are 1 cm.

5bb

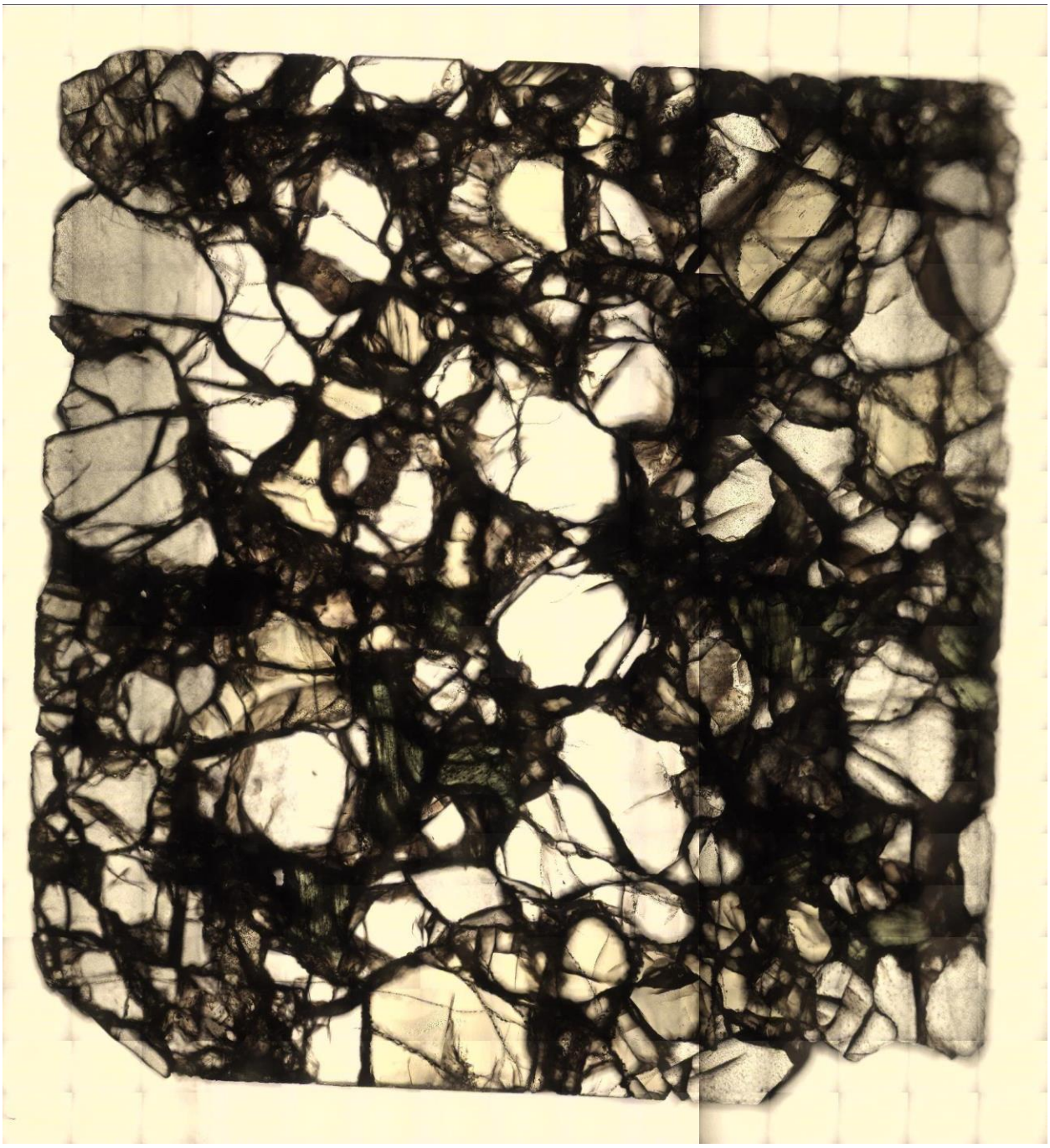

5aii

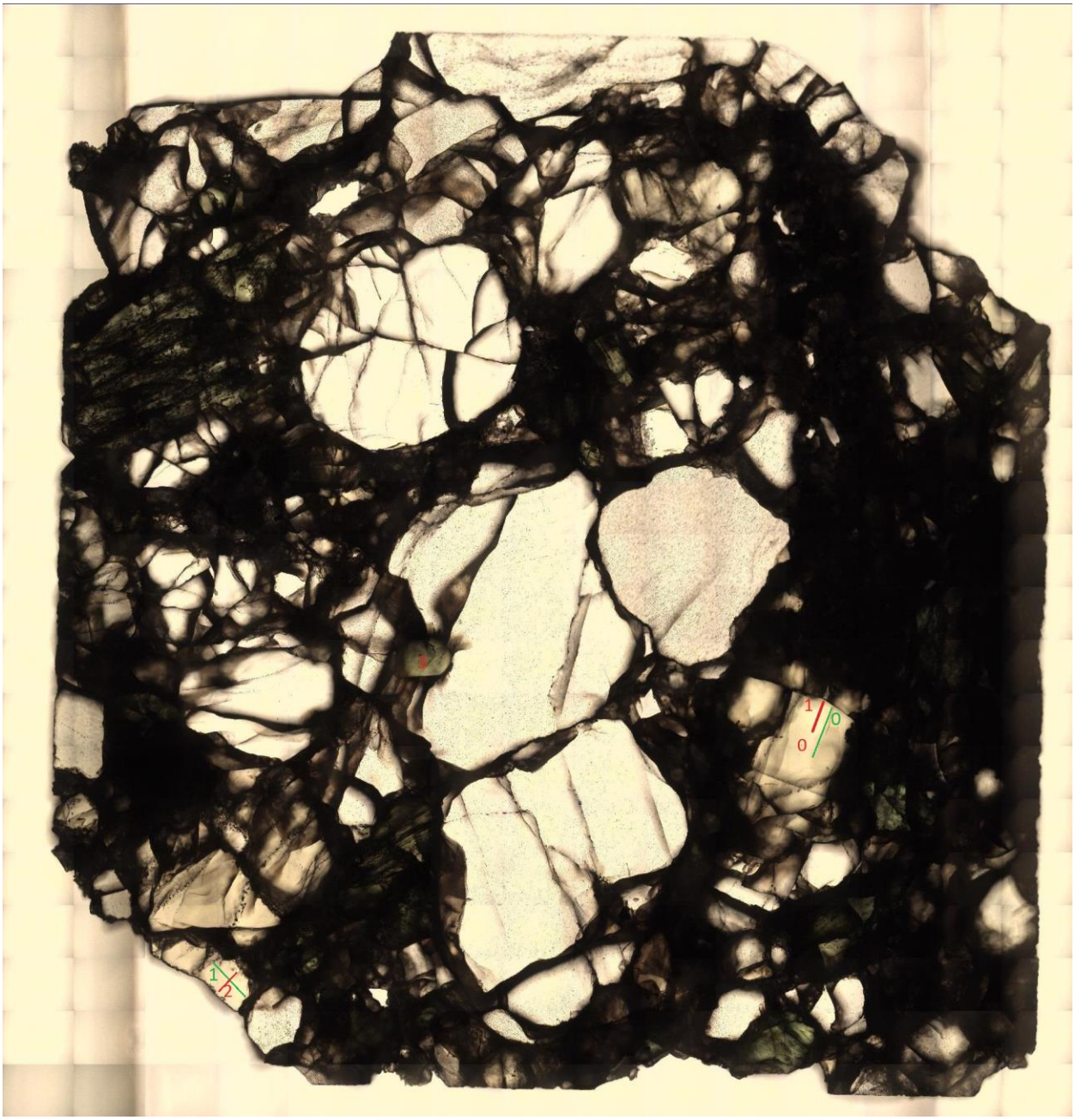

7ac

7b

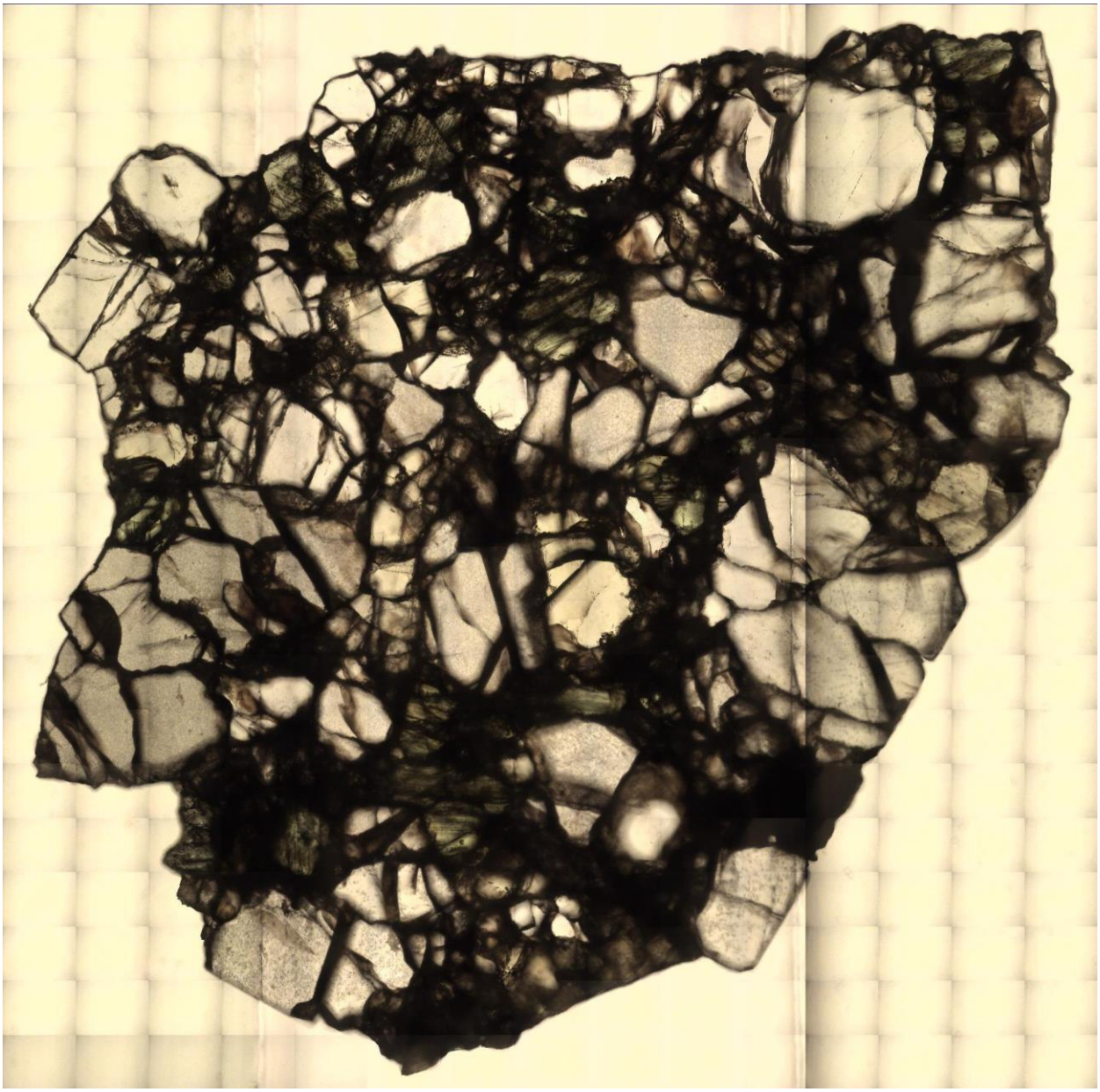

7b2

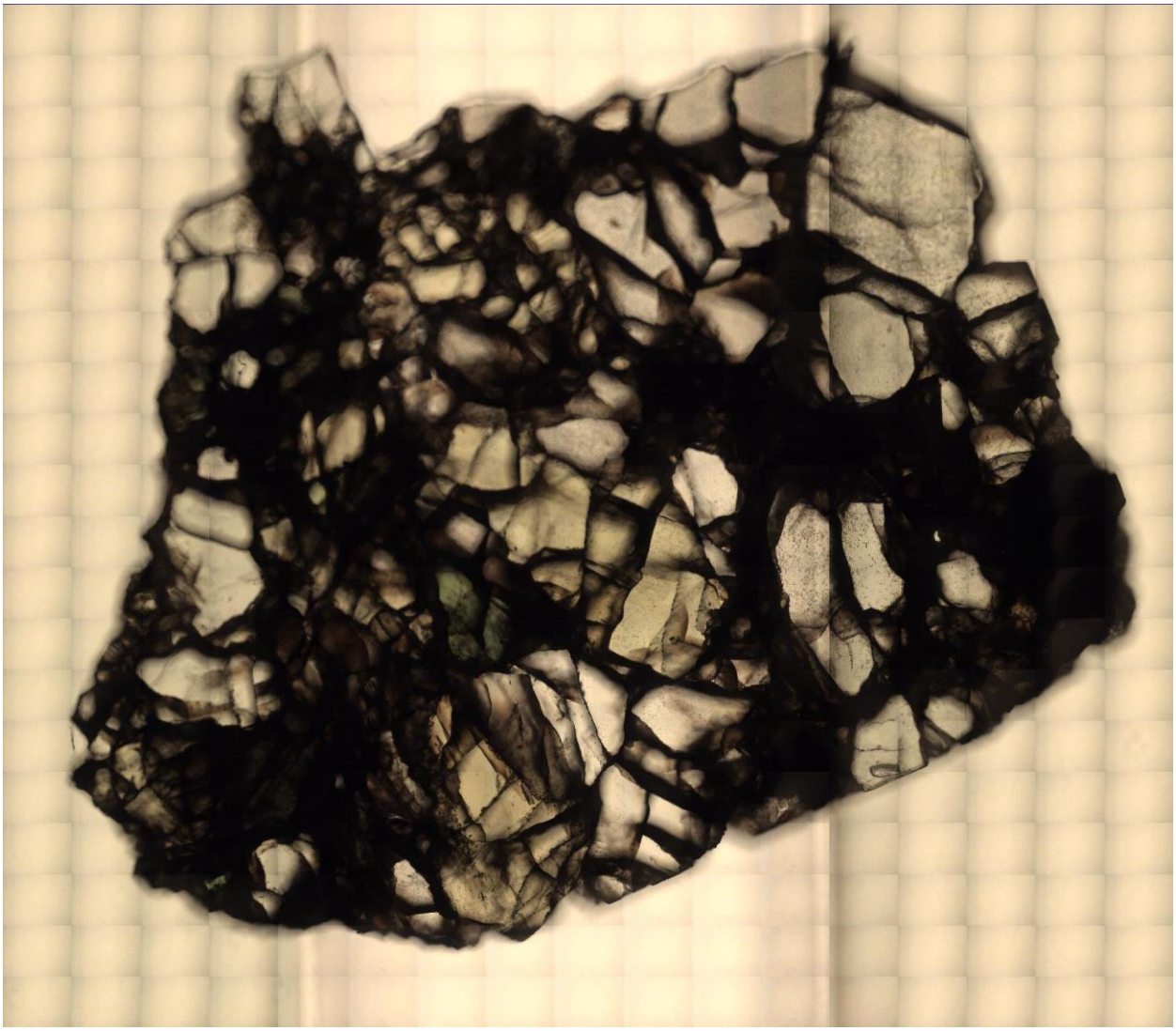

6c